JESTT

Vol. 2, Issue. 2, 2025

SCOPUA

Journal of Engineering, Science and Technological Trends

ISSN(e): 2959-1937

Volume 2 (Issue 2) Published on 2025-07-10

https://doi.org/10.64060/jestt.v2i2

2025

Journal Homepage

https://journals.scopua.com/index.php/JeSTT

Publisher

Scientific Collaborative Online Publishing Universal Academy

Publisher Homepage

https://scopua.com/

Model Town - Ferozepur Road, Near Atfaq Hospital, Lahore, Pakistan

Journal of Engineering, Science and Technological Trends

Aims & Scope

Journal of Engineering, Science and Technological Trends (JESTT) aims to advance the understanding of engineering sciences by providing a platform for the publication of unique contributions in the field of engineering, science, and technology.

The scope of the Journal of Engineering, Science and Technological Trends was interdisciplinary. During the board meeting on February 28, 2025, the scope of JESST was redefined to explicitly focus on "Materials Science and Engineering", "Nanoscience and Nanotechnology", "Environmental and Applied Engineering", "Computational and Data-Driven Approaches", and "Cybersecurity and Smart Systems".

The updated scope reflects our commitment to publishing high-quality, original, and innovative research that addresses contemporary challenges and advances theoretical and applied knowledge within the journal's core disciplines. JESTT welcomes manuscripts in both fundamental and applied research areas and encourages submissions that contribute novel and innovative insights to engineering science and technology. The scope of JESTT includes:

1. **Materials Science and Engineering**

- Additive Manufacturing (3D Printing of Materials)
- Biomaterials Engineering
- Inorganic and Organic Semiconductors
- Material Characterization
- Material Science
- Material Statistics (Use of Modern Statistics like Neutrosophic Analysis for Decision-Making in Materials Field)
- Materials Engineering
- Materials for Flexible and Wearable Electronics

2. **Nanoscience and Nanotechnology**

- Nanofabrication
- Nanomaterial-Based Sensors
- Nanotechnology

3. **Environmental and Applied Engineering**

- Heavy Metal Detection
- Hydraulic Engineering
- Sensor Technology

4. **Computational and Data-Driven Approaches**

- Computational Materials Science

- Computer Vision Applications
- Deep Learning in Pattern Recognition
- Digital Twin Technology in Engineering

5. **Cybersecurity and Smart Systems**

- Artificial Intelligence in Cybersecurity
- Smart Grid and Critical Infrastructure Protection

Editorial Board Members

Editor in Chief

Prof. Dr. Jiran Liang (Patron)

School of Microelectronics
Tianjin University,
Tianjin 300072, PR China

Gas Sensors, Humidity Sensors, Inorganic Thin Film Deposition, Smart Windows, Temperature Sensors, Thermochromic Vanadium Dioxide Thin Films, Zinc Oxide Nanostructures (Nanosheets and Nanorods).

Profile: Scopus ID | ResearchGate

Dr. Naveed Ahmad

University of Education Lahore, Pakistan

Experimental Physics, Heavy Metal Detection, Material Characterization, Materials Physics, Materials Science, Nanomaterials, Nanotechnology, Solid Waste Management, Thin Film Deposition

Profile: Google Scholar | ResearchGate

Editor

Dr. Qayyum Zafar

University of Management and Technology, Pakistan

Ambient Sensors (Humidity, Light, Temperature), Bulk-Heterojunction Organic Photodetectors, Organic Semiconductors, Perovskite Solar Cells, Thin-Film Devices, ZnO & Organic Nanocomposites.

Contents (Volume 2 & Issue 2 – 2025)

Journal of Engineering, Science and Technological Trends (JESTT)

Vol. 2, Issue 2, July 2025
DOI: https://doi.org/10.64060/jestt.v2i2.1

Communication

AI-Powered Innovation in Flexible and Implantable Electronics: From Sensors to Systems

Abdullah [1], Hafiza Kanza Maryam [1], Laraib [1], Hafiza Fatima [3]* and Muhammad Abubakar Rafi [4]

[1]School of Chemistry, University of the Punjab, Quaid-e-Azam Campus, Lahore, 54590, Pakistan
[2] Department of Chemistry, Lahore College for Women University, Pakistan
[3]Department of Physics, University of Agriculture Faisalabad, Pakistan
* Corresponding Email: f.afzal.edu@gmail.com (H. Fatima)

Received: 19 February 2025 / Revised: 19 May 2025 / Accepted: 26 June 2025 / Published online: 25 August 2025 (V-2)

ABSTRACT

A significant change in wearable and implantable biomedical technology is being driven by the combination of flexible electronics and artificial intelligence (AI). Real-time, non-invasive monitoring of vital signs, including temperature, heart rate, and mobility, is made possible by flexible devices because of their soft, biocompatible, and conformable architecture. These devices improve wearability and user comfort while providing ongoing healthcare tracking. By facilitating intelligent data processing, adaptable functionality, and expedited material discovery, AI greatly improves gadget performance. AI-driven, context-aware wearable devices support applications such as motion tracking, gesture recognition, and health monitoring. AI enhances quality control in manufacturing by using neural networks and computer vision to find flaws in parts like flexible PCBs. The creation of ecologically friendly devices is aided by AI-assisted predictive modelling and autonomous labs, which also help find high-performance, sustainable materials. The future of self-sustaining biomedical devices is being shaped by significant improvements in energy harvesting, electronic skin (e-skin), and intelligent interfaces, despite persistent constraints such as hardware integration, power management, data privacy, and limited computing capability. In order to create intelligent, sustainable, and high-performing healthcare systems, this paper examines the relationship between AI and flexible electronics, highlighting significant technical developments, existing constraints and new potential.

Keywords*:* Artificial Intelligence; Biomedical Sensors; Flexible Electronics; Intelligent Healthcare Systems; Wearable and Implantable Devices

1. Introduction

The development of flexible materials and next-generation electronics has significantly changed the biomedical sensing landscape. Flexible technologies, as opposed to conventional rigid electronics, provide previously unheard-of compatibility with the curved and dynamic surfaces of the human body, opening the door for novel uses in medical diagnostics and healthcare [1],[2]. Physiological data, including blood pressure, temperature, heart rate, and mobility patterns, may now be easily collected thanks to wearable and implanted electronic devices. These gadgets are transforming the way we monitor, identify, and treat medical diseases since they can fit into the skin or even be incorporated into the body [3]. In addition to providing increased wearability and comfort for users, flexible electronics are also making it easier for medical devices to become smaller and softer. This change enables less intrusive long-term monitoring and real-time data collection. Soft and flexible gadgets, in particular, act as platforms for stimulation and sensing, bridging the gap between biological tissues and electrical systems. For instance, neural prosthetics communicate with the nervous system through flexible substrates, allowing for motor control, sensory restoration, and even cognitive improvements [4],[5]. The power supply is essential to guaranteeing these systems' long-term functionality. The development of wearable and implantable energy harvesting devices that can transform biome-

chanical energy, including body motion, into useful electrical power is a growing area of research interest. These self-sustaining energy sources solve important issues such as device bulk, short operating lifespan, and the complexity of external signal processing components, in addition to lowering reliance on other power sources. It is also possible for these multipurpose devices to serve as active stimulators for organs and brain systems as well as power generators [6],[7],[8]. As the need for high-performing, biocompatible, and eco-friendly technologies increases, new materials, including biodegradable polymers and two-dimensional (2D) nanomaterials, are being incorporated into flexible systems. Particularly in implantable settings, these advancements aid in the creation of next-generation devices that are safer, lighter, and thinner for prolonged human usage. The combination of artificial intelligence (AI) and the Internet of Things (IoT) accelerates this paradigm shift towards smart and environmentally friendly devices [9].

The capabilities of flexible electronic systems are being greatly enhanced by AI-driven design and manufacturing techniques that simplify material selection, device optimisation, and real-time signal interpretation [10],[11]. We provide a thorough analysis of flexible electronic wearable and implantable technologies in this paper, including their use as energy harvesters, stimulators, and sensors. We examine current developments in 2D-material-based and biodegradable systems and show how AI and machine learning methods are being used to improve each step, from device operation to material discovery. For high-performance and sustainable systems, special attention is paid to AI-assisted material selection, intelligent manufacturing, and power efficiency techniques [12]. We illustrate how AI is transforming healthcare electronics through case studies and current research, allowing for precise motion recognition, improved comfort, and environmentally friendly design. Lastly, we go over the difficulties and potential paths of this quickly developing sector, highlighting chances for multidisciplinary cooperation and creativity.

2. Role of Artificial Intelligence in Materials Science

Human civilisation's progress has always been closely linked to the resources available to it. The development of materials has continuously signalled important turning points in human history, from the primitive stone implements of prehistoric times to the advanced composites and semiconductors powering modern technology. The capacity to find, develop, and use sophisticated materials more effectively is becoming more and more important as we approach the Fourth Industrial Revolution. The core of this effort is materials science. Researchers seek to develop novel materials with improved functionality by investigating how a material's internal structure, processing techniques, and intrinsic qualities impact its performance in many applications. The vast volume and complexity of accessible data remain the field's primary bottleneck, despite centuries of advancement and a significant collection of experimental data and theoretical ideas [13]. The rapid rate of discoveries is too much for human intellect to handle, and conventional discovery methods, which frequently rely on empirical knowledge and gradual experimentation, remain a laborious and sluggish obstacle that has opened the door for a new approach to materials research that makes use of AI [14]. Over the course of decades, AI has developed from straightforward rule-based systems to complex neural networks that can outperform humans in a variety of activities, including medical diagnosis, language comprehension, and gaming. AI is a vital tool for materials research because of its capacity to handle enormous amounts of data and identify subtle trends, which speeds up innovation and discovery. Materials informatics is a new multidisciplinary area that emerged from the combination of artificial intelligence and materials science. This field uses data-driven models to forecast material characteristics, pinpoint the best synthesis routes, boost characterisation techniques, and increase process efficiency. Machine learning (ML), a kind of AI that allows computers to learn from data, identify correlations, and generate well-informed predictions without explicit programming for every job, lies at the heart of this revolution. Materials research is already starting to change as a result of machine learning. ML models are capable of carrying out tasks that would be unreasonably time-consuming using traditional techniques, such as quickly screening vast chemical spaces, suggesting new compounds, and improving manufacturing conditions. In addition to lowering trial-and-error, these technologies provide a degree of predicted accuracy that was previously unachievable. The framework for a more thorough examination of the foundational ideas of machine learning and their application to materials science is established by this introduction. Researchers can uncover novel materials more quickly, more cheaply, and more precisely than ever before by adopting AI-driven methodologies, which will usher in a new era of invention and discovery.

3. AI in Material Design for Flexible Electronics

From consumer electronics and healthcare diagnosis to communications and energy systems, wearable sensors offer a wide range of possible uses. More work is being done locally on edge devices as the industry moves toward decentralised computing. Microcontrollers are progressively incorporating embedded AI and ML, enabling wearable devices to interpret data in real-time with increased efficiency and privacy. This change improves responsiveness and lessens reliance on centralised cloud computing. AI algorithms are currently used in embedded systems, which are usually made for specific purposes, to increase their usefulness. Wearables are closer to adaptive systems that can learn from human interactions, modify operating settings, and make wise judgments on their own when combined with flexible sensors and integrated machine learning. The combination of integrated intelligence with flexible materials creates new opportunities for energy harvesting, gesture recognition, and health monitoring [15]. The strategic acquisitions of AI-focused software startups by semiconductor giants demonstrate the industry's reaction to this trend. Micro-ML and embedded AI are two terms that are quickly becoming popular, indicating how important they will be in determining the direction of embedded systems in the future [16].

3.1. Sensing Mechanisms in Wearable Devices

By translating inputs like pressure, strain, temperature, gas concentration, or humidity into readable electrical impulses, sensors act as the link between the physical or chemical environment and electronic systems. The resistive, capacitive, piezoelectric, and triboelectric modes are the main sensor mechanisms shown in Figure 1.

3.2. Integration of Embedded Machine Learning with Flexible Sensors in Wearable Technologies

Continuous, time-series data sequential information captured at regular intervals, depending on the unique properties and application of each sensor, is naturally produced by wearable systems that include flexible sensors, as shown in Figure 2. The identification of temporal patterns, trends, and recurrent behaviours, all crucial for dynamic analysis in real-time settings, is made possible by this chronological structure. Conventional systems usually concentrate on gathering and processing this unprocessed sensor data using basic methods like noise reduction, signal amplification, nor-

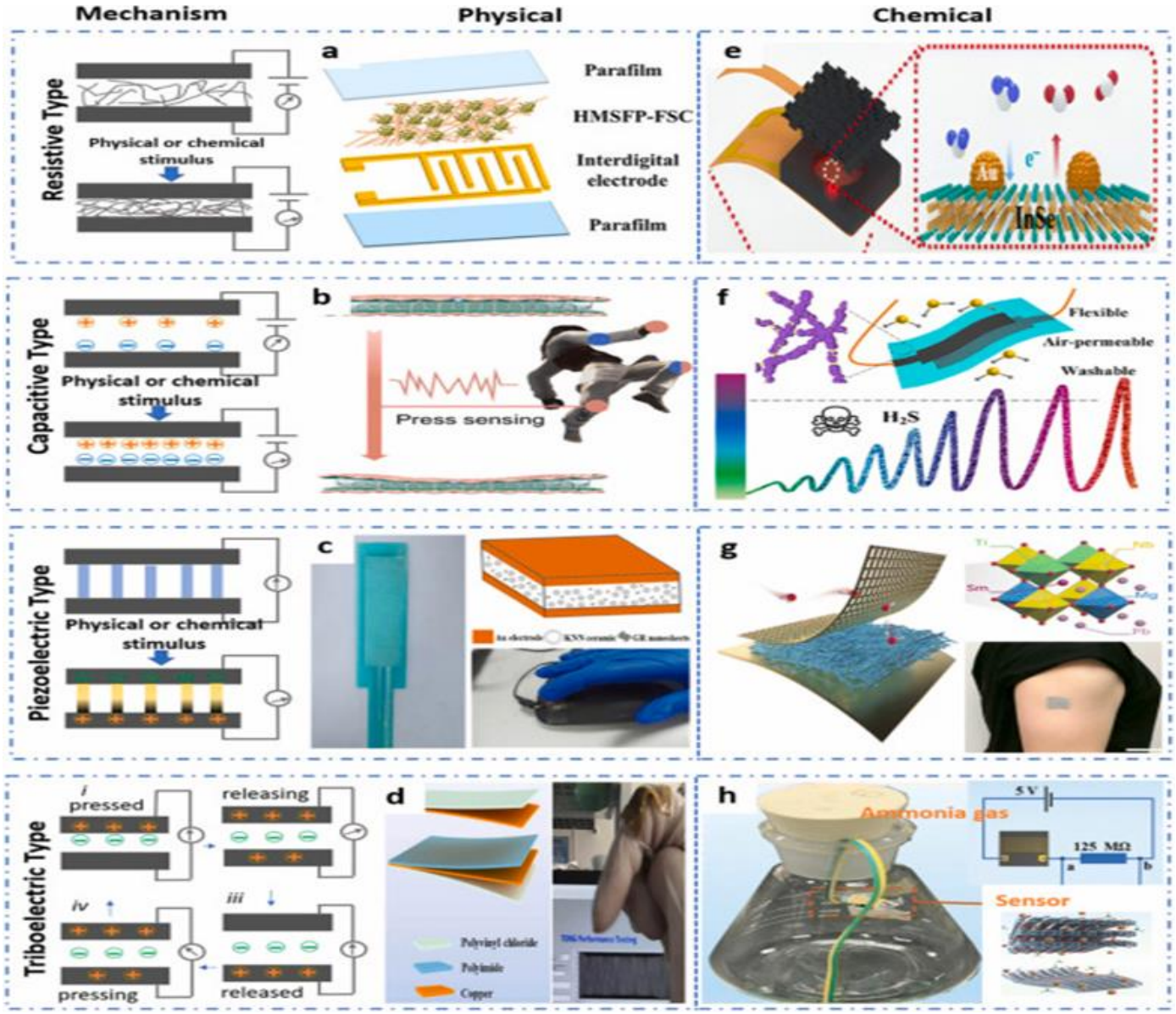

Figure 1: *Sensing mechanisms, including physical and chemical stimulus* [17]: **(a).** *Flat silk cocoon pressure sensor based on a sea urchin-like microstructure* [18], **(b).** *Flexible pressure textile sensors for monitoring athletic motion during Taekwondo* [19], **(c).** *Flexible piezoelectric sensors based on graphene doping (GR/KNN/P(VDF-TrFE))* [20], **(d).** *Stretchable triboelectric nanogenerators based on flexible polyimide for energy harvesting and self-powered sensors* [21], **(e).** *A fully integrated flexible tunable chemical sensor from gold-modified indium selenide nanosheets* [22], **(f).** *Flexible H_2S sensors by growing NO_2-UiO-66 on electrospun nanofibers* [23], **(g).** *Piezoelectric textile sensors for self-powered humidity detection and wearable biomonitoring* [24] and **(h).** *A room temperature ammonia gas sensor by a freestanding-mode triboelectric nanogenerator* [25].

malisation, and outlier removal. The structure and format of the data are two of the most important factors in choosing the right learning model from the perspective of artificial intelligence.

Therefore, the combination of flexible sensors with integrated machine learning opens the door to wearables that are context-aware, adaptable, and capable of continually learning and reacting to their surroundings with ever-increasing intelligence [26],[27].

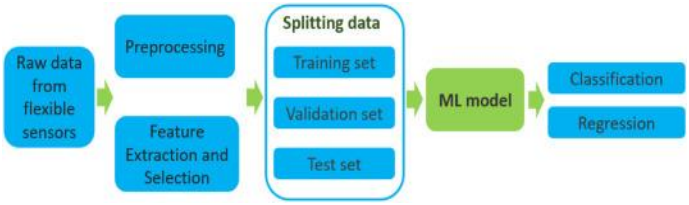

Figure 2: *The general process of ML algorithms for data interpretation* [28].

Preservatives, for example, can stop germs from growing, greatly lowering the risk of foodborne diseases [26]. The function of smart edible films in the circular economy is another crucial element; researchers are looking into making these films out of food industry leftovers, which encourages waste reduction and resource efficiency [27]. For instance, materials made from whey protein or fruit peels not only efficiently use trash but also give the films functional and nutritional improvements. This approach makes the entire food packaging process more ecologically friendly and aligns with sustainable food development goals.

4. AI-Driven Defect Detection and Quality Control in Flexible Electronics

Every step of the manufacturing process for flexible electronics, including stretchy circuits, bendable displays, and wearable sensors, requires accuracy and consistency. However, conventional quality control techniques frequently fail to detect microscopic or structural flaws because of the intrinsic complexity of flexible substrates and materials (such as plastic films, conductive polymers, or nanomaterials). AI, especially ML and computer vision, has emerged as a game-changer in improving quality assurance and defect identification in the production of flexible electronics [29]. AI-driven defect detection systems use sophisticated algorithms and high-resolution imaging technologies (such as optical microscopes, infrared cameras, X-rays, etc.) to automatically detect surface irregularities, including cracks, voids, delamination, wrinkles, or misalignments. Both the human eye and traditional rule-based inspection methods frequently have trouble identifying these flaws. To precisely identify and detect anomalies in real time, machine learning models, particularly convolutional neural networks (CNNs), are trained on enormous databases of tagged defect pictures [30].

4.1. Flexible PCBs (FPCBs)

The core of many stretchy and wearable gadgets is made of flexible printed circuit boards, or FPCBs. They are susceptible to certain kinds of manufacturing flaws, like broken traces, short circuits, misalignments, delamination, or inadequate etching, and are composed of pliable substrates like polyimide. High-resolution analysis of multilayer architectures is necessary for the detection of such flaws, and this gets more challenging as current circuits get smaller and more complicated [31].

4.2. CNNs

A family of deep learning algorithms known as CNNs has emerged as a vital tool for detecting PCB defects. When it comes to pattern identification and picture categorisation, CNNs excel. Anomalies, including open circuits, soldering errors, missing components, and microcracks, may be automatically detected by the system by training CNNs on thousands of annotated photos of PCB regions that are problematic and those that are not. Compared to rule-based algorithms or human-based visual inspection, these models provide a reliable, automated inspection system that can handle data from a variety of imaging sources, including optical, infrared, and even X-ray scans.

High-speed PCB scanning, circuit layout segmentation and real-time inference using CNNs are all done by AI-powered inspection systems in production settings to identify any flaws. These systems are incorporated into roll-to-roll (R2R) processing lines for continuous monitoring in the fabrication of flexible electronics. When combined with sophisticated imaging methods, CNN-based models are able to examine deeper structural discrepancies in addition to detecting surface-level irregularities [32]. AI integration with smart edge devices also makes it possible to forecast and analyse localised defects, which lowers latency and permits real-time manufacturing parameter modifications. In order to minimise scrap rates and enable proactive interventions, predictive maintenance models may also be constructed utilising historical PCB failure data.

5. AI-Powered Exploration of Advanced Materials

Modern science and engineering are fast changing due to AI, which is becoming a driving force behind ground-breaking advancements in fields including chemistry, materials science, and sustainable engineering. Its power resides in its capacity to simplify the research process, reveal hidden linkages, and evaluate intricate datasets, basically altering the way discoveries are created. AI has been crucial in lowering the time, money, and energy needed to create novel solutions in the context of green chemistry and sustainable technologies. It has also improved product performance, efficiency, and safety. AI's capacity to tackle global environmental and socioeconomic issues is among its most significant accomplishments [33]. AI acts as a link between conventional research techniques and the new requirements of a circular economy in the framework of sustainable development. The development of intelligent, automated research settings that can optimise experimental methods in real time is the result of collaboration between AI professionals and domain specialists in green technologies.

AI-powered autonomous labs are revolutionising the traditional trial-and-error methodology. Based on human-defined goals, these systems create, suggest, and improve trials using machine learning techniques. These trials are carried out by automated robotic platforms, and the outcomes are relayed back into the system so that the AI can keep improving its predictions. This closed-loop approach significantly reduces the time, energy, and material resources required for discovery by moving away from static experimental techniques and toward dynamic, adaptive research processes [34]. Furthermore, predictive toxicology and material discovery are being redefined by AI-driven simulations and quantum computing. Large databases of materials, experimental data, and scientific literature may now be mined by sophisticated machine learning algorithms to find patterns and discover novel compounds with desired characteristics. Four steps are usually included in the process: theory formulation, synthesis planning, property prediction, and material characterisation. AI is particularly good at processing and analysing the vast amounts of high-dimensional data produced by image and sensor technologies during the characterisation phase. However, access to huge, high-quality datasets is necessary for AI in material science to reach its full potential. Enabling equitable and scalable AI tools in chemistry requires the creation of open-access platforms and centralised data repositories. These programs have the potential to eliminate major obstacles in chemical research and sustainability-driven innovation by promoting data exchange and standardisation [35].

6. Challenges and Limitations

Particularly in flexible wearable technologies, embedded intelligent systems depend on the smooth integration of a number of essential parts, such as memory units, actuators or transmission elements, soft sensors, power sources like batteries, and small hardware platforms running specialised software. For real-time decision-making and responsive actions based on ongoing data collection to be possible, all elements must work together harmoniously. Incorporating ML into these systems has greatly increased their capabilities, enabling increased cost-effectiveness, accuracy, and efficiency in a variety of applications. Intelligent processing is made possible by machine learning algorithms, which provide insights that can improve system efficiency and customise user experiences with little assistance from humans. One characteristic of embedded systems that allows for low-latency replies and ongoing performance enhancements is real-time signal processing. This results in more seamless interactions, prompt feedback, and context-aware decision-making for end users, all of which increase consumer convenience and happiness [36]. Several significant obstacles still exist in spite of the expanding potential of flexible wearable systems driven by embedded machine learning. Optimal system design is still hampered by problems including inconsistent data gathering, restricted transmission bandwidth, limited computer power, and the difficulty of integrating disparate hardware compo-

nents. Although flexible sensors are more versatile and wearable, they also present other challenges, such as noise sensitivity, fluctuating signal strength, and non-linear output, which make it more difficult to analyse signals and interpret data accurately.

Another significant challenge is establishing dependable hardware connections between soft sensors and more conventional system components, including stiff sensors or printed circuit boards. In addition to hardware issues, portability and scalability are problems for embedded machine learning systems. The majority of embedded systems run on little or no OS at all, rather than full-fledged operating systems like Windows or Linux. Although task-specific design saves resources, it makes model deployment and application variety more difficult. Although there are alternatives like FreeRTOS and Mbed OS, their overhead and complexity prevent them from being widely used in practical applications. Privacy and security are also major issues. Because they frequently gather private behavioural and physiological data, wearable technology is a prime target for attackers. Ensuring data protection through encryption, ethical design and secure ML models is crucial for maintaining user trust and system reliability [37].

7. Future Perspectives

A new frontier characterised by multi-functionality, self-sustainability, and improved intelligence is rapidly emerging in wearable electronics and photonics. It is anticipated that these next-generation systems will surpass simple sensing or display capabilities and develop into all-encompassing platforms with the ability to communicate intelligently with both their users and their surroundings. One of the primary areas of interest in this field is the creation of electronic skins, which are elastic or flexible arrays of sensors that mimic the human somatosensory system. Pressure, strain, temperature, humidity, light, and even magnetic fields are just a few of the environmental stimuli that these sophisticated sensor networks are made to identify and measure. One of the recent advancements in this field is the integration of a flexible sensor matrix onto a polyimide substrate, which allows for the simultaneous detection of several physical stimuli in a small, three-dimensional manner. Such an invention opens the door to advanced applications in health monitoring systems, prosthetics, robotics, and human–machine interfaces (HMIs) [38]. In order to provide wireless connection, data transfer, and real-time visualisation, wearable systems are concurrently integrating optoelectronic displays and photonic components. The usefulness and responsiveness of wearable platforms are increased by these integrated modules, which also minimise electromagnetic interference and improve the user interface.

One of the key obstacles to wearable technology's long-term, untethered functioning is energy management. When it comes to supplying sustained power, conventional batteries are inadequate, particularly for applications requiring constant monitoring. The combination of energy collecting and storage technologies is addressing this constraint. Motion, heat, and light are examples of ambient energy sources that may be transformed into useful electricity via hybrid systems that include many transduction processes, including piezoelectric, thermoelectric, triboelectric, and photovoltaic effects. Though promising, these systems currently have efficiency issues; frequently, they need to gather energy over long periods of time in order to power brief activity spurts. In order to achieve fully autonomous and continuous functioning, ongoing research attempts to improve energy conversion rates and storage capacities.

A revolutionary change has occurred with the merging of wearable technology and artificial intelligence. These systems can now handle complicated, multimodal data streams and accurately spot patterns thanks to machine learning techniques. Capability is opening up new applications in fields like biometric security, smart surroundings, tailored medicine, and immersive VR/AR experiences [39].

8. Conclusion

AI and flexible electronics are revolutionising wearable and implantable technology, particularly in the medical field. Smarter diagnosis and treatment are made possible by these systems' benefits, which include comfort, biocompatibility, and continuous vital sign monitoring. By facilitating adaptive learning, intelligent decision making, and real-time data processing on the device itself, embedded AI improves these gadgets. Additionally, AI speeds up defect identification, device optimisation, and material discovery, enhancing production quality and performance. To fully utilise these technologies, however, several issues must be resolved, including low power, signal noise, integration hurdles, and data privacy issues. Future wearables that are intelligent, multipurpose, and self-sustaining will be made possible by advancements like integrated optoelectronics, hybrid energy harvesting, and electronic skin. An important step toward smarter, more responsive systems is being taken with the combination of AI and flexible electronics, which is opening the door to more individualised, effective and linked healthcare solutions.

Declaration

Competing Interests: The authors declare that they have no known competing financial interests or personal relationships that could have appeared to influence the work reported in this paper.

Ethical Issues: There are no ethical issues. All data in this paper is publicly available.

Author Contribution Statement: A.A, H.K.M, L. H.F. and M.A. conceived idea and designed the research; Analyzed interpreted the data and wrote the paper.

Funding Statement: This research did not receive any specific grant from funding agencies in the public, commercial, or not-for-profit sectors.

Consent to Publish: All authors are agreed to publish version of the manuscript in this journal.

References

1. “Complementing the Genome with an ‘Exposome’: The Outstanding Challenge of Environmental Exposure Measurement in Molecular Epidemiology | Cancer Epidemiology, Biomarkers & Prevention | American Association for Cancer Research.” Accessed: Jun. 24, 2025. [Online]. Available:https://aacrjournals.org/cebp/article/14/8/1847/258124/Complementing-the-Genome-with-an-Exposome-The

2. “AI-Enabled Wearable and Flexible Electronics for Assessing Full Personal Exposures: The Innovation.” Accessed: Jun. 12, 2025. [Online]. Available: https://www.cell.com/the-innovation/fulltext/S2666-6758(20)30031-X

3. Z. Shen *et al*., “Progress of flexible strain sensors for physiological signal monitoring,” *Biosens. Bioelectron.*, vol. 211, p. 114298, Sep. 2022, doi: 10.1016/j.bios.2022.114298.

4. K. Huang, Z. Ma, and B. L. Khoo, “Advancements in Bio-Integrated Flexible Electronics for Hemodynamic Monitoring in Cardiovascular

Healthcare," *Adv. Sci.*, vol. n/a, no. n/a, p. 2415215, doi: 10.1002/advs.202415215.

5. J. Wang *et al.*, "Ultrasensitive, Highly Stable, and Flexible Strain Sensor Inspired by Nature," *ACS Appl. Mater. Interfaces*, vol. 14, no. 14, pp. 16885–16893, Apr. 2022, doi: 10.1021/acsami.2c01127.

6. "Recent Progress in Energy Harvesting Technologies for Self-Powered Wearable Devices: The Significance of Polymers - Afshar - 2025 - Polymers for Advanced Technologies - Wiley Online Library." Accessed: Jun. 24, 2025. [Online]. Available: https://onlinelibrary.wiley.com/doi/full/10.1002/pat.70187?casa_token=KUwbZy_6jYEAAAAA%3AGMaNYCSCkB55Qb4KIZogZG5Vo7yjZUAoWN05HZbR4qnDyesbYFLDLdn6o-0v1OpVBLQyRoi499aRD8A

7. F. Akhtar and M. H. Rehmani, "Energy Harvesting for Self-Sustainable Wireless Body Area Networks," *IT Prof.*, vol. 19, no. 2, pp. 32–40, Mar. 2017, doi: 10.1109/MITP.2017.34.

8. Y. H. Kwon *et al.*, "Triboelectric energy harvesting technology for self-powered personal health management," *Int. J. Extreme Manuf.*, vol. 7, no. 2, p. 022005, Dec. 2024, doi: 10.1088/2631-7990/ad92c7.

9. "Green Artificial Intelligence | 15 | Biodegradable and Biocompatible M." Accessed: Jun. 24, 2025. [Online]. Available: https://www.taylorfrancis.com/chapters/edit/10.1201/9781003546382-15/green-artificial-intelligence-hamid-kanchan-bhatt-naseer-ahmed-priyanka-chauhan

10. S. Lee, Q. Shi, and C. Lee, "From flexible electronics technology in the era of IoT and artificial intelligence toward future implanted body sensor networks," *APL Mater.*, vol. 7, no. 3, p. 031302, Feb. 2019, doi: 10.1063/1.5063498.

11. "Recent Progress and Challenges of Implantable Biodegradable Biosensors." Accessed: Jun. 24, 2025. [Online]. Available: https://www.mdpi.com/2072-666X/15/4/475

12. "Artificial intelligence enhanced sensors - enabling technologies to next-generation healthcare and biomedical platform | Bioelectronic Medicine." Accessed: Jun. 24, 2025. [Online]. Available: https://link.springer.com/article/10.1186/s42234-023-00118-1

13. U. Afzal *et al.*, "Chemical engineering for advanced flexible sensors: Novel carbon-metal oxide nanocomposites with superior multi-sensing behavior," *Sens. Actuators B Chem.*, vol. 431, p. 137449, May 2025, doi: 10.1016/j.snb.2025.137449.

14. S. Zhao, F. Blaabjerg, and H. Wang, "An Overview of Artificial Intelligence Applications for Power Electronics," *IEEE Trans. Power Electron.*, vol. 36, no. 4, pp. 4633–4658, Apr. 2021, doi: 10.1109/TPEL.2020.3024914.

15. C. C. Vu, "Embedded-machine learning and soft, flexible sensors for wearable devices - viewing from an AI engineer," *Mater. Today Phys.*, vol. 42, p. 101376, Mar. 2024, doi: 10.1016/j.mtphys.2024.101376.

16. S. Lin *et al.*, "An ultralight, flexible, and biocompatible all-fiber motion sensor for artificial intelligence wearable electronics," *Npj Flex. Electron.*, vol. 6, no. 1, pp. 1–8, Apr. 2022, doi: 10.1038/s41528-022-00158-8.

17. C. C. Vu, "Embedded-machine learning and soft, flexible sensors for wearable devices - viewing from an AI engineer," *Mater. Today Phys.*, vol. 42, p. 101376, Mar. 2024, doi: 10.1016/j.mtphys.2024.101376.

18. Y. Wang, Y. Wang, M. Xu, F. Dai, and Z. Li, "Flat Silk Cocoon Pressure Sensor Based on a Sea Urchin-like Microstructure for Intelligent Sensing," *ACS Sustain. Chem. Eng.*, vol. 10, no. 51, pp. 17252–17260, Dec. 2022, doi: 10.1021/acssuschemeng.2c05540.

19. Y. Ma *et al.*, "Flexible all-textile dual tactile-tension sensors for monitoring athletic motion during taekwondo," *Nano Energy*, vol. 85, p. 105941, Jul. 2021, doi: 10.1016/j.nanoen.2021.105941.

20. X. Zhang, W. Xia, C. Cao, P. Che, H. Pan, and Y. Chen, "Graphene doping to enhance the mechanical energy conversion performances of GR/KNN/P(VDF-TrFE) flexible piezoelectric sensors," *Phys. Chem. Chem. Phys.*, vol. 25, no. 2, pp. 1257–1268, Jan. 2023, doi: 10.1039/D2CP05091A.

21. C. Li, P. Wang, and D. Zhang, "Self-healable, stretchable triboelectric nanogenerators based on flexible polyimide for energy harvesting and self-powered sensors," *Nano Energy*, vol. 109, p. 108285, May 2023, doi: 10.1016/j.nanoen.2023.108285.

22. "A Fully Integrated Flexible Tunable Chemical Sensor Based on Gold-Modified Indium Selenide Nanosheets | ACS Sensors." Accessed: Jun. 24, 2025. [Online]. Available: https://pubs.acs.org/doi/full/10.1021/acssensors.2c00281?casa_token=3pw285GPDvwAAAAA%3AQdg1YJJvevrsQHkodNXYzkzh35zpP-e8Riu7KjrZzbDUTqrEefTEkavfsbfMdPQ0oqqs82Hq1Iz7tiE

23. L. Zhang *et al.*, "A Fully Integrated Flexible Tunable Chemical Sensor Based on Gold-Modified Indium Selenide Nanosheets," *ACS Sens.*, vol. 7, no. 4, pp. 1183–1193, Apr. 2022, doi: 10.1021/acssensors.2c00281.

24. "Sensing–transducing coupled piezoelectric textiles for self-powered humidity detection and wearable biomonitoring - Materials Horizons (RSC Publishing)." Accessed: Jun. 24, 2025. [Online]. Available: https://pubs.rsc.org/en/content/articlelanding/2023/mh/d2mh01466a/unauth

25. X. Wang, L. Gong, Z. Li, Y. Yin, and D. Zhang, "A room temperature ammonia gas sensor based on cerium oxide/MXene and self-powered by a freestanding-mode triboelectric nanogenerator and its multifunctional monitoring application," *J. Mater. Chem. A*, vol. 11, no. 14, pp. 7690–7701, Apr. 2023, doi: 10.1039/D2TA07917H.

26. H.-Y. Lin, "Embedded Artificial Intelligence: Intelligence on Devices," *Computer*, vol. 56, no. 9, pp. 90–93, Sep. 2023, doi: 10.1109/MC.2023.3280397.

27. H. Ren, D. Anicic, and T. Runkler, "TinyOL: TinyML with Online-Learning on Microcontrollers," arXiv.org. Accessed: Jun. 12, 2025. [Online]. Available: https://arxiv.org/abs/2103.08295v3

28. C. C. Vu, "Embedded-machine learning and soft, flexible sensors for wearable devices - viewing from an AI engineer," *Mater. Today Phys.*, vol. 42, p. 101376, Mar. 2024, doi: 10.1016/j.mtphys.2024.101376.

29. "Enhancing PCB Quality Control through AI-Driven Inspection: Leveraging Convolutional Neural Networks for Automated Defect Detection in Electronic Manufacturing Environments by Harshit Kumar Ghelani: SSRN." Accessed: Jun. 12, 2025. [Online]. Available: https://papers.ssrn.com/sol3/papers.cfm?abstract_id=5160737

30. H. Ghelani, *AI-Driven Quality Control in PCB Manufacturing: Enhancing Production Efficiency and Precision*. 2024.

31. A. Goti, "AI-Driven PCB Reliability Testing for IPC-9701 Compliance," Mar. 10, 2025, *Social Science Research Network, Rochester, NY*: 5237687. doi: 10.2139/ssrn.5237687.

32. J. Song, Gao, Shaohua, Zhu , Yunqiang, and C. and Ma, "A survey of remote sensing image classification based on CNNs," *Big Earth Data*, vol. 3, no. 3, pp. 232–254, Jul. 2019, doi: 10.1080/20964471.2019.1657720.

33. R. Mishra, D. Mishra, and R. Agarwal, "An Artificial Intelligence-Powered Approach to Material Design," 2024, pp. 62–89.

34. X. Bai and X. Zhang, "Artificial Intelligence-Powered Materials Science," *Nano-Micro Lett.*, vol. 17, no. 1, p. 135, Feb. 2025, doi: 10.1007/s40820-024-01634-8.

35. Imran, F. Qayyum, D.-H. Kim, S.-J. Bong, S.-Y. Chi, and Y.-H. Choi, "A Survey of Datasets, Preprocessing, Modeling Mechanisms, and Simulation Tools Based on AI for Material Analysis and Discovery," *Materials*, vol. 15, no. 4, Art. no. 4, Jan. 2022, doi: 10.3390/ma15041428.

36. D. Baran, D. Corzo, and G. T. Blazquez, “Flexible Electronics: Status, Challenges and Opportunities,” *Front. Electron.*, vol. 1, Sep. 2020, doi: 10.3389/felec.2020.594003.

37. A. Yadav, *GEN AI-DRIVEN ELECTRONICS: INNOVATIONS, CHALLENGES AND FUTURE PROSPECTS*. 2023. doi: 10.5281/zenodo.8165255.

38. K. Potter, M. Lord, and G. O. Olaoye, “Future Unraveled The Wonders of Wearable and Flexible Electronics,” Oct. 05, 2023, *OSF*. doi: 10.31219/osf.io/5xkfw.

39. Y. Zang, F. Zhang, C. Di, and D. Zhu, “Advances of flexible pressure sensors toward artificial intelligence and health care applications,” *Mater. Horiz.*, vol. 2, no. 2, pp. 140–156, 2015, doi: 10.1039/C4MH00147H.

Journal of Engineering, Science and Technological Trends (JESTT)

Vol. 2, Issue 2, July 2025
DOI: https://doi.org/10.64060/jestt.v2i2.2

Review

Critical Review on the Phase Change Properties of VO_2: Influence of Synthesis Methods and Transition Mechanisms

Ansa Firdous[1]* and Abrar Ashraf[2]

[1]Government College University Faisalabad, Pakistan
[2] Departamento de Engenharia de Materiais, Escola de Engenharia de Lorena (EEL), Universidade de São Paulo (USP), Lorena 12.612 - 550, Sao Paulo, Brazil
* Corresponding Email: ansaeducation7@gmail.com (A. Firdous)

Received: 29 January 2025 / Revised: 01 June 2025 / Accepted: 25 June 2025 / Published online: 10 July 2025

ABSTRACT

Vanadium dioxide (VO_2) is a strongly correlated material that exhibits a reversible metal-insulator transition (MIT) near room temperature (~68°C), accompanied by a structural phase transition from a monoclinic (M1, insulating) to a tetragonal rutile (R, metallic) phase. This unique property makes VO_2 a promising candidate for applications in smart windows, optoelectronic switches, and thermal sensors. However, the phase transition characteristics, such as transition temperature, hysteresis width, and optical/electrical contrast, are highly dependent on the synthesis method. This review critically examines the impact of different synthesis techniques (e.g., chemical vapour deposition, sol-gel, sputtering, pulsed laser deposition, and hydrothermal synthesis) on the phase transition properties of VO_2. A comparative analysis is presented, highlighting how stoichiometry, strain, defects, and doping influence the MIT. Additionally, the fundamental chemistry governing the phase transition is discussed, with a focus on electron correlation effects and lattice dynamics. A comprehensive comparison table summarises the synthesis methods, their effects on phase transition properties, and key challenges.

Keywords*:* Defect chemistry; Mott transition; Phase-change materials; Thermochromic materials

1. Introduction

Vanadium dioxide (VO_2) has emerged as one of the most intriguing functional materials in condensed matter physics and materials science due to its remarkable metal-insulator transition (MIT) near 68°C [1],[2]. This first-order phase transformation involves a reversible structural change from a low-temperature monoclinic phase (M1, $P2_1/c$ space group) to a high-temperature tetragonal rutile phase (R), accompanied by dramatic alterations in its electronic and optical properties [3]. The transition manifests as an abrupt decrease in electrical resistivity by up to five orders of magnitude and significant modulation of infrared transmittance, making VO_2 particularly attractive for applications in smart windows, optical switches, and thermal sensors [4],[5]. These exceptional properties stem from the complex interplay between electron-electron correlations (Mott-Hubbard mechanism) and structural distortions (Peierls instability), positioning VO_2 as a prototypical system for studying strongly correlated electron materials and coupled electronic-structural phase transitions [6],[7].

The physics underlying VO_2's phase transition has been the subject of extensive research since its discovery in 1959 by Morin [8]. The insulating M1 phase features paired vanadium ions along the c-axis, creating a dimerised structure with split d‖ orbitals that establish a bandgap of approximately 0.6 eV [1],[9],[10]. Upon heating through the transition temperature (T_t), these dimers dissociate, leading to a delocalisation of d-electrons and the formation of a metallic state with overlapping energy bands [11]. This electronic reorganisation occurs concomitantly with structural changes in the VO_6 octahedra coordination, where the V-V distance evolves from alternating short (2.65 Å) and long (3.12 Å) separations in the M1 phase to a uniform spacing (2.87 Å) in the R phase [5],[12]. The transition is highly sensitive to external stimuli, including temperature, electric fields, and optical excitation, enabling multiple control modalities for device applications.

The practical implementation of VO_2 in functional devices critically depends on the ability to precisely control its phase transition characteristics, which are intimately linked to the material's synthesis and processing conditions. Various fabrication methods, including physical vapour deposition, chemical vapour deposition, and solution-based approaches, produce VO_2 with distinct microstructural features that profoundly influence its MIT behaviour [3],[13],[14]. Key parameters such as crystallinity, stoichiometry, strain state, and defect concentration are largely determined by the synthesis technique and processing parameters. For instance, oxygen non-stoichiometry can introduce charge carriers that modify the transition temperature, while epitaxial strain from lattice-mismatched substrates can stabilise intermediate phases or shift T_t by tens of degrees. Additionally, nanoscale confinement effects become prominent in low-dimensional VO_2 structures, where surface and interface contributions can significantly alter the transition thermodynamics [1].

Understanding the relationship between synthesis methods and phase transition properties is essential for optimising VO_2's performance in specific applications. Different deposition techniques offer varying degrees of control over critical material parameters - while physical vapour deposition methods like pulsed laser deposition can produce high-quality epitaxial films with sharp transitions, they often lack scalability [15],[16]. Conversely, chemical and solution-based methods may be more suitable for large-area applications but typically introduce more defects and heterogeneity [17]. The growing interest in VO_2-based devices has driven the development of novel synthesis approaches that combine the advantages of multiple techniques while mitigating their limitations. Recent advances in atomic layer deposition and hybrid processing methods have enabled unprecedented control over VO_2's structural and electronic properties at the nanoscale.

This review systematically examines the various synthesis methods for VO_2 and their impact on the material's phase transition characteristics. By critically analysing the relationship between fabrication techniques, structural properties, and MIT behaviour, we aim to provide a comprehensive resource for researchers seeking to optimise VO_2 for specific applications. The discussion encompasses fundamental aspects of phase transition chemistry, detailed comparisons of synthesis methodologies, and their respective influences on transition temperature, hysteresis, and switching dynamics. Ultimately, this work seeks to establish structure-property-processing relationships that can guide the rational design of VO_2-based materials with tailored performance characteristics for advanced technological applications.

2. Phase Transition Chemistry of VO_2

The metal-insulator transition (MIT) in vanadium dioxide (VO_2) is a complex phenomenon governed by coupled electronic and structural transformations. Below the critical transition temperature ($T_t \approx 68°C$), VO_2 exists in a low-temperature monoclinic phase (M1, space group $P2_1/c$), which is insulating, while above T_t, it transitions to a high-temperature tetragonal rutile phase (R, space group $P4_2/nm$), exhibiting metallic conductivity [4],[18],[19]. This transition is driven by strong electron-electron correlations (Mott-Hubbard mechanism) and structural distortions (Peierls instability), making VO_2 a prototypical correlated electron material. The transmission diagram can be seen in Figure 1:

2.1. Electronic Transition Mechanism

In the insulating M1 phase, vanadium (V^{4+}) ions undergo dimerisation along the *c*-axis, resulting in a pairing distortion that splits the degenerate $d_{\parallel}$ orbitals $(d_{x^2-y^2})$ into bonding and antibonding states. This Peierls-like distortion, combined with strong on-site Coulomb repulsion (U), opens a Mott-Hubbard gap (~0.6 eV), rendering the material insulating [21],[22]. The electronic transition can be represented by the following charge disproportionation reaction in (1):

$$2V^{4+} \rightleftharpoons V^{3+} + V^{5+} \text{ (in the M1 phase)} \qquad \textbf{(1)}$$

Above T_t, the *V-V* dimers dissociate, leading to a delocalisation of *d*-electrons and the collapse of the bandgap. The metallic R phase is characterised by overlapping $d_{\parallel}$ bands, resulting in enhanced electrical conductivity.

2.2. Structural Transition Mechanism

The M1-to-R transition involves a cooperative distortion of the VO_6 octahedra [23]. In the M1 phase, the vanadium chains exhibit alternating short (≈ 2.65 Å) and long (≈ 3.12 Å) V-V distances due to dimerisation, while the R phase adopts a symmetric rutile structure with uniform V-V spacing (≈ 2.87 Å). The structural transformation is accompanied by a significant unit cell volume change (~1%), which contributes to the first-order nature of the transition.

2.3. Key Factors Influencing the MIT

- ***Stoichiometry and Defects***: Oxygen non-stoichiometry ($VO_{2 \pm x}$) introduces point defects such as oxygen vacancies (V_o) or interstitials (O_i), which perturb the electronic structure and alter T_t [24]. For example, oxygen-deficient VO_2 tends to exhibit a reduced T_t due to increased electron doping shown in (2):

$$VO_2 \rightarrow VO_{2-x} + xV\ddot{O} + 2xe^- \qquad \textbf{(2)}$$

  Where $V\ddot{O}$ denotes a doubly charged oxygen vacancy.

- ***Epitaxial Strain***: Substrate-induced strain can stabilise metastable phases (e.g., the M2 or T phase) or shift T_t. Compressive strain typically lowers T_t, while tensile strain may increase it. For instance, VO_2 grown on TiO_2 (001) experiences compressive strain, reducing T_t by up to 20°C [25].
- ***Doping Effects***: Cation substitution (e.g., W^{6+}, Mo^{6+}, Ti^{4+}) can significantly modulate T_t. Tungsten doping (W^{6+}) is particularly effective, decreasing T_t by ~20–25°C per at% W due to electron donation shown in (3) [26]:

$$V^{4+}_{1-x}\, W^{6+}_x O_2 \rightarrow V^{4+}_{1-2x}\, V^{3+}_x\, W^{6+}_x O_2 \qquad \textbf{(3)}$$

  Conversely, aliovalent dopants like Al^{3+} or Cr^{3+} increase T_t by introducing hole carriers.

- ***Grain Size and Morphology***: Nanocrystalline VO_2 exhibits a broadened MIT due to surface and interface effects [27]. Quantum confinement in nanoparticles (< 20 nm) can suppress the transition entirely, while mesoporous films show reduced thermal hysteresis.

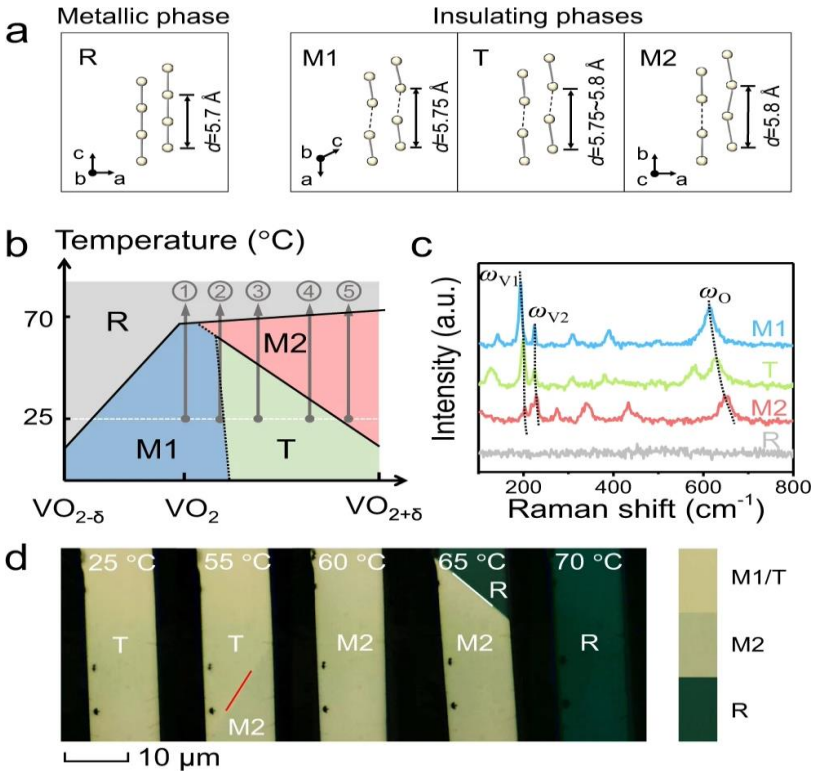

Figure 1: (a). *Schematics of the arrangement of V ions in different VO_2 phases (M1, T, M2, and R). The solid circles represent the V ions, solid lines represent a short V–V distance of <0.3 nm, and dash lines connect the neighboring V ions with a V–V distance of >0.3 nm,* **(b).** *Schematics of stoichiometry–temperature phase diagram for VO_2 crystals. The gray, blue, green, and red regions in the diagram represent the R phase, M1 phase, T phase, and M2 phase, respectively. The gray arrows (routes 1–5) trace the phase evolution process of VO_2 with various oxygen contents from room temperature,* **(c).** *Characteristic Raman spectra of VO_2 phases. Dash lines trace ω_{V1}, ω_{V2}, and ω_O phonon frequencies in the Raman spectra and* **(d).** *Temperature-dependent optical images of a single VO_2 beam upon heating, revealing its whole domain evolution process corresponding to route 3 of* ***b****. The red line shows the position of the domain wall between T and M2 phases, while the white line shows the position of the M2-R domain wall* [20].

2.4. Summary of Phase Transition Chemistry

The MIT in VO_2 is a delicate interplay of electronic correlation, lattice dynamics, and defect chemistry. Precise control over stoichiometry, strain, and doping is essential for tailoring the transition properties for specific applications. The following Table 1 summarises key chemical and structural aspects of the MIT:

Table 1:
Chemical and structural aspects of the MIT

Parameter	M1 Phase (Insulating)	R Phase (Metallic)
Crystal Structure	Monoclinic ($P2_1/c$)	Tetragonal Rutile ($P4_2/mnm$)
V-V Dimerization	Present (2.65 Å / 3.12 Å)	Absent (uniform 2.87 Å)
Bandgap	~0.6 eV (Mott-Hubbard)	Closed (metallic)
Dominant Mechanism	Peierls + Mott-Hubbard	Band overlap

3. Synthesis Methods and Their Impact on Phase Transition Properties

The synthesis of vanadium dioxide (VO_2) is a critical factor in determining its metal-insulator transition (MIT) characteristics, as different fabrication techniques produce materials with distinct structural, morphological, and electronic properties. The choice of synthesis method influences key parameters such as crystallinity, stoichiometry, grain size, and defect concentration, all of which play crucial roles in modulating the transition temperature (T_t), hysteresis width, and switching sharpness. This section provides a detailed examination of various synthesis approaches and their specific effects on VO_2's phase transition behaviour.

3.1. Physical Vapour Deposition (PVD) Methods

Among physical deposition techniques, magnetron sputtering and pulsed laser deposition (PLD) are widely used for VO_2 thin film fabrication [28]. Magnetron sputtering, which involves reactive deposition of vanadium in an oxygen-argon atmosphere, offers excellent control over film stoichiometry through precise regulation of oxygen partial pressure. The process can be described by (4):

$$V\ (target) + O_2 \rightarrow VO_x\ (film) \qquad (4)$$

The process typically requires post-deposition annealing at 400-500°C to achieve optimal crystallinity, with the resulting films exhibiting well-defined MIT characteristics. However, defect formation, particularly oxygen vacancies, can lead to hysteresis

broadening, while stress accumulation in thicker films may cause mechanical failure. PLD, utilising laser ablation of a vanadium target in an oxygen environment, produces highly epitaxial films with exceptionally sharp transitions ($\Delta T < 5°C$) [29]. PLD utilises laser ablation of a vanadium target in an oxygen background as shown in (5):

$$V\ (target) + O_2 \xrightarrow{laser} VO_2\ (film) \qquad (5)$$

The technique allows for strain engineering through substrate selection, with Al_2O_3 and TiO_2 being common choices for modulating T_t. Despite its superior film quality, PLD suffers from limitations in deposition area and high equipment costs, making it less suitable for large-scale applications.

3.2. Chemical Vapour Deposition (CVD) Techniques

Chemical vapour deposition methods, including atmospheric-pressure CVD (APCVD) and metal-organic CVD (MOCVD), provide alternative routes for VO_2 synthesis. APCVD employs halide precursors such as $VOCl_3$ at elevated temperatures (500-600°C), resulting in polycrystalline films with grain size dependent on deposition temperature [30]. APCVD employs halide precursors at elevated temperatures, as in (6):

$$VOCl_3 + H_2O \rightarrow VO_2 + 3HCl\ (500-600°C) \qquad (6)$$

While higher temperatures improve crystallinity and reduce T_t, the method often produces films with significant surface roughness and challenges in thickness control below 50 nm. MOCVD, using organometallic precursors like vanadyl acetylacetonate, operates at lower temperatures (300-450°C) and enables conformal coatings on complex geometries [31]. MOCVD uses organometallic precursors as in (7):

$$VO\ (ac)_2 \rightarrow VO_2 + \text{volatile byproducts}\ (300-450\ °C) \qquad (7)$$

However, carbon incorporation from precursor decomposition can reduce T_t by 10-15°C and may introduce electronic defects. Both CVD approaches offer better scalability than PVD methods but require careful optimisation to minimise impurities and defects that could degrade MIT performance.

3.3. Solution-Processed Methods

Solution-based synthesis techniques, including sol-gel and hydrothermal methods, present cost-effective alternatives for VO_2 preparation. The sol-gel process involves hydrolysis-condensation of vanadium alkoxides followed by high-temperature annealing (>500°C), yielding materials with broadened hysteresis (ΔT up to 30°C) due to high defect concentrations [32],[33]. Nanoparticle size effects become prominent below 20 nm, with quantum confinement potentially suppressing the MIT entirely. Involves hydrolysis-condensation of vanadium alkoxides, as can be seen in (8):

$$VO(OR)_3 + H_2O \rightarrow VO(OH)_x \xrightarrow{\Delta} VO2 \qquad (8)$$

Hydrothermal synthesis, conducted in aqueous solutions at elevated pressures, produces various nanostructures such as nanowires and nanorods [13],[34]. Autoclave-based crystallisation can be seen in (9):

$$V_2O_5 + \text{reductant} \rightarrow VO_2\ \text{nanostructures} \qquad (9)$$

These materials exhibit anisotropic MIT behaviour and size-dependent transition characteristics, with surface defects often mediating transition broadening. While solution methods offer advantages in scalability and nanostructure control, they typically require post-synthesis treatments to achieve the desired stoichiometry and crystallinity, and may introduce organic residues that affect electronic properties.

3.4. Advanced Deposition Techniques

Molecular beam epitaxy (MBE) and atomic layer deposition (ALD) represent the state-of-the-art in precision VO_2 fabrication. MBE provides atomic-level control under ultra-high vacuum conditions, producing films with atomically sharp interfaces and extremely narrow hysteresis (<1°C) [35]. Ultra-high vacuum growth, as can be seen (10):

$$V\ (effusion) + O_2 \rightarrow VO_2\ (atomic\ layer\ control) \qquad (10)$$

This method enables fundamental studies of strain and interface effects but suffers from prohibitively low growth rates and high costs. ALD, based on self-limiting surface reactions, offers exceptional conformality and thickness control at the Angstrom level, making it ideal for coating high-aspect-ratio structures [36]. Self-limiting surface reactions as in (11):

$$VCl_4 + H_2O \rightarrow VO_2 + 4HCl \qquad (11)$$

However, ALD-grown VO_2 often contains amorphous components that lower T_t, and may incorporate halide impurities from precursors. These advanced techniques, while not yet suitable for mass production, provide invaluable insights into structure-property relationships and serve as benchmarks for material quality.

The following Table 2 summarises key synthesis techniques and their effects on VO_2 phase transition properties.

4. Key Challenges and Future Perspectives in VO_2 Research

Despite significant advancements in the synthesis and characterisation of VO_2, several critical challenges persist that limit its practical implementation in next-generation devices.

4.1. Current Challenges

- ***Stoichiometric Precision***: Maintaining exact VO_2 stoichiometry remains challenging, as oxygen vacancies ($VO^{\cdot\cdot}$) and non-stoichiometric phases ($VO_2 \pm \delta$) dramatically influence the metal-insulator transition (MIT) characteristics, including transition temperature (T_c), hysteresis width, and switching dynamics. Even minor deviations ($\delta > 0.01$) can suppress the MIT or induce intermediate phases.
- ***Scalability Limitations***: While high-precision techniques like molecular beam epitaxy (MBE) and pulsed laser deposition (PLD) yield superior single-crystalline films with sharp transitions, their low throughput and high costs hinder industrial adoption. Alternative methods, such as chemical vapour deposition (CVD), offer better scalability but often compromise on film quality and transition sharpness.

Table 2:
Effects of synthesis techniques on VO_2 phase transition

Synthesis Method	Crystallinity	Typical T_t (°C)	Hysteresis Width	Key Advantages	Key Challenges
Magnetron Sputtering	Polycrystalline/Epitaxial	60–75	5–15°C	Scalable, tunable strain	Defects, requires annealing
PLD	Highly Epitaxial	65–70	1–5°C	High-quality films	Expensive, small area
APCVD	Polycrystalline	65–75	10–20°C	Good uniformity	Rough morphology
MOCVD	Polycrystalline	50–70	10–25°C	Conformal coatings	Carbon contamination
Sol-Gel	Nanoporous/Polycrystalline	60–80	15–30°C	Low cost, scalable	High defects, broad hysteresis
Hydrothermal	Nanostructured	40–70	10–40°C	High surface area	Stoichiometry control difficult
MBE	Single-crystal Epitaxial	~68	<1°C	Ultra-precise	Extremely costly
ALD	Amorphous/Nanocrystalline	50–65	10–20°C	Atomic-level control	Low crystallinity

- ***Precise Property Tuning***: Although doping (e.g., W^{6+}, Mo^{6+}) and strain engineering can modulate T_c, achieving predictable and uniform property control across large-area samples remains difficult. Substrate-induced strain, in particular, can lead to inhomogeneous phase distributions and metastable intermediate states (e.g., M2 or T phases).
- ***Interface and Substrate Effects***: In thin-film architectures, interfacial reactions, lattice mismatch, and thermal expansion differences can dominate MIT behaviour, often masking intrinsic material properties. This is especially problematic for heterostructure integration in device applications.

4.2. Future Research Directions

To address these challenges, future efforts should prioritise:

- ***Low-Temperature Synthesis***: Developing growth techniques that enable high-quality VO_2 deposition below 300°C would facilitate integration with flexible substrates (e.g., polymers) and temperature-sensitive device architectures. Plasma-enhanced atomic layer deposition (PE-ALD) and photochemical solution processing are promising avenues.
- ***Defect Engineering***: Advanced characterisation techniques (e.g., in-situ TEM, XAS) combined with computational modelling can help establish defect-property relationships, enabling targeted mitigation of oxygen vacancies and grain boundary effects that broaden hysteresis.
- ***Hybrid Fabrication Strategies***: Combining the strengths of different methods, such as ALD for interfacial control, followed by CVD for bulk growth, could provide an optimal balance between scalability and film quality. Additionally, additive manufacturing approaches may enable novel VO_2 nanostructuring.
- ***Device-Oriented Optimisation***: Future work should focus not only on fundamental material properties but also on integration challenges, including contact engineering, interfacial stability, and cycling endurance for practical applications in memristors, smart coatings, and thermal switches.

5. Conclusion

The phase transition properties of VO_2 are highly sensitive to the synthesis method, which affects stoichiometry, strain, and microstructure. Physical deposition techniques (sputtering, PLD) yield high-quality films with sharp transitions, while solution-based methods offer scalability at the cost of broader hysteresis. Understanding the interplay between synthesis conditions and MIT behaviour is crucial for optimising VO_2 for applications in smart coatings, sensors, and electronic devices. Future advancements in defect control and strain engineering will further enhance the performance of VO_2-based technologies.

Declaration

Competing Interests: The authors declare that they have no known competing financial interests or personal relationships that could have appeared to influence the work reported in this paper.

Ethical Issues: There are no ethical issues. All data in this paper is publicly available.

Author Contribution Statement: A.F. and A. A. conceived idea and designed the research; Analyzed interpreted the data and wrote the paper.

Funding Statement: This research did not receive any specific grant from funding agencies in the public, commercial, or not-for-profit sectors.

Consent to Publish: The Authors have agreed to publish version of the manuscript in this journal.

References

1. Li, Z., Z. Zhang, and X. Zhou, Chemical Modulation of Metal–Insulator Transition toward Multifunctional Applications in Vana-dium Dioxide Nanostructures. Small, 2023. 19(44): p. 2305234.
2. Zhang, Y., et al., Recent progress on vanadium dioxide nanostruc-tures and devices: Fabrication, properties, applications and per-spectives. Na-nomaterials, 2021. 11(2): p. 338.
3. Kumar, A., et al., A comprehensive review on synthesis, phase transi-tion, and applications of VO2. Journal of Superconductivity and Novel Mag-netism, 2024. 37(3): p. 475-498.
4. Cao, X., et al., Challenges and opportunities toward real applica-tion of VO2-based smart glazing. Matter, 2020. 2(4): p. 862-881.
5. Afzal, U., et al., Chemical Engineering for Advanced Flexible Sen-sors: Novel Carbon-Metal Oxide Nanocomposites with Superior Multi-Sensing Behavior. Sensors and Actuators B: Chemical, 2025: p. 137449.
6. Liu, Y., et al., An interesting functional phase change material VO2: re-sponse to multivariate control and extensive applications in op-tics and electronics. Advanced Electronic Materials, 2024. 10(4): p. 2300699.
7. Hong, W.-K., et al., Metal-insulator phase transition in quasi-one-dimensional VO2 structures. Journal of Nanomaterials, 2015. 2015(1): p. 538954.
8. Haddad, E., et al., Review of the VO2 smart material applications with emphasis on its use for spacecraft thermal control. Frontiers in Materials, 2022. 9: p. 1013848.
9. Davenport, M.A., Investigation of structural changes in vanadium contain-ing transition metal oxides. 2020: The University of Ala-bama.
10. Whittaker, L., Synthesis, characterization and phase transitions of single-crystalline vanadium (IV) oxide nanostructures. 2011: State University of New York at Buffalo.
11. Eyert, V., The metal-insulator transitions of VO2: A band theoreti-cal approach. Annalen der Physik, 2002. 514(9): p. 650-704.
12. Hu, P., et al., Vanadium oxide: phase diagrams, structures, synthesis, and applications. Chemical Reviews, 2023. 123(8): p. 4353-4415.
13. Li, M., et al., Hydrothermal synthesis of VO2 polymorphs: ad-vantages, challenges and prospects for the application of energy ef-ficient smart windows. Small, 2017. 13(36): p. 1701147.
14. Zhang, L., et al., VO2 (A) nanorods: One-pot synthesis, formation mecha-nism and thermal transformation to VO2 (M). Ceramics Inter-national, 2018. 44(16): p. 19301-19306.
15. Yu, J., et al., Recent Advances on Pulsed Laser Deposition of Large-Scale Thin Films. Small Methods, 2024. 8(7): p. 2301282.
16. Muratore, C., A.A. Voevodin, and N.R. Glavin, Physical vapor depo-sition of 2D Van der Waals materials: a review. Thin Solid Films, 2019. 688: p. 137500.
17. Guo, B., et al., Direct synthesis of high-performance thermal sensi-tive VO2 (B) thin film by chemical vapor deposition for using in un-cooled in-frared detectors. Journal of Alloys and Compounds, 2017. 715: p. 129-136.
18. Wen, C., et al., A review of the preparation, properties and applica-tions of VO2 thin films with the reversible phase transition. Frontiers in Materials, 2024. 11: p. 1341518.
19. Pouget, J.-P., Basic aspects of the metal–insulator transition in vanadium dioxide VO $ _ {2} $: a critical review. Comptes Rendus. Physique, 2021. 22(1): p. 37-87.
20. Shi, R., et al., Phase management in single-crystalline vanadium dioxide beams. Nature Communications, 2021. 12(1): p. 4214.
21. Shao, Z., et al., Recent progress in the phase-transition mechanism and modulation of vanadium dioxide materials. NPG Asia Materials, 2018. 10(7): p. 581-605.
22. Valakh, M.Y., et al., Variation of the metal-insulator phase transi-tion temperature in VO2: An overview of some possible implementa-tion methods. Semicond. Physics, Quantum Electronics & Optoelec-tronics, 2024. 27(2): p. 136.
23. Hiroi, Z., Structural instability of the rutile compounds and its rele-vance to the metal–insulator transition of VO2. Progress in Solid State Chemis-try, 2015. 43(1-2): p. 47-69.
24. Zhang, J., et al., Evolution of structural and electrical properties of oxy-gen-deficient VO2 under low temperature heating process. ACS applied materials & interfaces, 2017. 9(32): p. 27135-27141.
25. Yang, Y., et al., Thickness effects on the epitaxial strain states and phase transformations in (001)-VO2/TiO2 thin films. Journal of Ap-plied Phys-ics, 2019. 125(8).
26. Hu, L., et al., Porous W-doped VO 2 films with simultaneously en-hanced visible transparency and thermochromic properties. Journal of Sol-Gel Science and Technology, 2016. 77: p. 85-93.
27. Paik, T., et al., Solution-processed phase-change VO2 metamaterials from colloidal vanadium oxide (VO x) nanocrystals. ACS nano, 2014. 8(1): p. 797-806.
28. Ba, C., et al., Fabrication of high-quality VO2 thin films by ion-assisted dual ac magnetron sputtering. ACS Applied Materials & In-terfaces, 2013. 5(23): p. 12520-12525.
29. Barimah, E.K., et al., Infrared optical properties modulation of VO2 thin film fabricated by ultrafast pulsed laser deposition for thermo-chromic smart window applications. Scientific Reports, 2022. 12(1): p. 11421.
30. Vernardou, D., M.E. Pemble, and D.W. Sheel, The Growth of Ther-mochromic VO2 Films on Glass by Atmospheric-Pressure CVD: A Com-parative Study of Precursors, CVD Methodology, and Sub-strates. Chemi-cal Vapor Deposition, 2006. 12(5): p. 263-274.
31. Mathur, S., et al., Metal–Organic Chemical Vapor Deposition of Metal Oxide Films and Nanostructures. Ceramics Science and Technology, 2013: p. 291-336.
32. Landau, M.V., Sol–gel process. Handbook of Heterogeneous Ca-talysis: Online, 2008: p. 119-160.
33. Chae, B.-G., et al., Highly oriented VO2 thin films prepared by sol-gel deposition. Electrochemical and solid-state letters, 2005. 9(1): p. C12.
34. Popuri, S.R., et al., Rapid hydrothermal synthesis of VO2 (B) and its con-version to thermochromic VO2 (M1). Inorganic chemistry, 2013. 52(9): p. 4780-4785.
35. Fan, L., et al., Growth and phase transition characteristics of pure M-phase VO2 epitaxial film prepared by oxide molecular beam epi-taxy. Applied Physics Letters, 2013. 103(13).
36. Prasadam, V., et al., Study of VO2 thin film synthesis by atomic layer deposition. Materials Today Chemistry, 2019. 12: p. 332-342.

Journal of Engineering, Science and Technological Trends (JESTT)

Vol. 2, Issue 2, July 2025
DOI: https://doi.org/10.64060/jestt.v2i2.3

Review

Electrochemical Biosensors for Real-Time Oxidative Stress Monitoring in Saliva

Hafiza Kanza Maryam[1]*, Abdullah[1] and Hafiza Fatima[2]

[1]School of Chemistry, University of the Punjab, Quaid-e-Azam Campus, Lahore, 54590, Pakistan
[2]Department of Chemistry, Lahore College for Women University, Pakistan
* Corresponding Email: k.maryam.edu@gmail.com (H. K. Maryam)

Received: 02 March 2025 / Revised: 27 May 2025 / Accepted: 20 June 2025 / Published online: 25 August 2025 (V-2)

ABSTRACT

Oxidative stress, resulting from an imbalance between reactive oxygen species and antioxidant defences, is a critical factor in the onset and progression of numerous diseases, including cancer, cardiovascular conditions, and neurological disorders. Early detection of oxidative stress biomarkers is essential for timely diagnosis and effective treatment. Saliva has emerged as a highly attractive biofluid for this purpose due to its non-invasive, easily accessible, and cost-effective collection. Recent advancements in electrochemical biosensors have significantly enhanced the sensitivity, selectivity, and reliability of detecting oxidative stress indicators in saliva. These innovative sensing platforms enable real-time monitoring of key biomarkers at low concentrations, offering great potential for clinical and point-of-care applications. However, challenges such as sensor stability, biofouling, and interference from complex salivary components remain to be addressed to ensure robust performance in practical settings. This review summarises the latest developments in electrochemical biosensing of salivary oxidative stress biomarkers, highlights existing limitations, and discusses prospective strategies to overcome current barriers. The continued evolution of this technology promises to facilitate early disease detection and improve patient outcomes through accessible and precise oxidative stress monitoring.

Keywords*:* Disease monitoring; Electrochemical biosensors; Non-invasive diagnostics; Oxidative stress; Point-of-care sensing; Reactive oxygen species

1. Introduction

A pathological state caused by an imbalance between antioxidant defence mechanisms and reactive oxygen/nitrogen species (ROS/RNS), oxidative stress is a major factor in the development and progression of many chronic diseases, such as diabetes, cancer, autoimmune diseases, cardiovascular diseases, and neurodegenerative disorders [1]. Protein folding and oxidative phosphorylation are two examples of regular biological processes that produce reactive oxygen and nitrogen species (ROS and RNS) [2]. These comprise both non-radical (like hydrogen peroxide and hypochlorous acid) and radical (like superoxide, hydroxyl, and nitric oxide) forms, each with unique biological functions and reactivities [3]. Although ROS and RNS are vital for cell signalling, too much of them can lead to oxidative stress and harm various parts of the cell. Even with their acknowledged importance, research is still ongoing to distinguish between their physiological and pathological functions [4]. Despite the critical role of reactive oxygen and nitrogen species (ROS/RNS) in cellular signalling and stress responses, there is a lack of effective tools for their selective and real-time detection in living systems. Electrochemical methods using custom-designed microelectrodes offer promising solutions, enabling direct, in situ monitoring of specific ROS/RNS like hydrogen peroxide (H_2O_2), nitric oxide (NO), peroxynitrite ($ONOO^-$), and superoxide ($O_2^{\bullet-}$) with high spatial and temporal resolution [5].

Under normal conditions, antioxidant systems tightly regulate ROS levels to maintain redox balance. However, both deficiency and excess of ROS can disrupt physiological processes [6]. Low ROS levels impair immune response, wound healing, and cell signaling, while excess ROS leads to oxidative damage of DNA, proteins, and lipids markers such as 3-nitrotyrosine (3-NT), Malondialdehyde (MDA), and 8-Hydroxy-2'-deoxyguanosine (8-OHdG) are often used to assess this damage in clinical samples [7].

Still, these biomarkers reflect downstream effects rather than real-time ROS dynamics and fail to distinguish between specific ROS types. Current analytical techniques like electron paramagnetic resonance and photon-emission spectroscopy are limited by cost, complexity, and low temporal resolution [8]. Thus, there is a pressing need for highly sensitive, selective, and rapid-response tools capable of detecting specific ROS in real-time. Developing such electrochemical sensors remains a key challenge in advancing our understanding of oxidative stress and improving disease diagnostics and treatment evaluation.

Saliva's simplicity of collection, low sample processing requirements, and association with systemic health have made it an attractive non-invasive biological fluid for the identification of oxidative stress indicators [9]. Conventional analytical techniques like GC-MS, ELISA, LC-MS/MS, and HPLC have been used to measure these biomarkers in biological matrices [10]. These methods are less appropriate for point-of-care or real-time monitoring applications, though, because they frequently include drawbacks, including high costs, laborious procedures, the requirement for trained staff, and complicated equipment.

Because of their intrinsic benefits, high sensitivity, specificity, portability, minimal sample volume needs, quick response, and compatibility with wearable formats, electrochemical biosensors present a strong alternative [11]. By boosting active surface area, enhancing conductivity, and facilitating selective molecular recognition, the incorporation of nanomaterials like metal nanoparticles (like AuNPs), graphene oxide nanoribbons (GONRs), multi-walled carbon nanotubes (MWCNTs), and molecularly imprinted polymers (MIPs) has further improved the performance of these sensors [12],[13]. MIP-based electrochemical sensors are particularly well-suited for detecting tiny oxidative stress indicators like 3-NT and 8-OHdG in intricate biological settings like saliva because they replicate antibody-antigen interactions with enhanced stability and reduced manufacturing costs [14].

With an emphasis on 3-NT, 8-OHdG, MDA, and ROS, this review aims to give readers a thorough grasp of saliva as a potentially useful diagnostic fluid, emphasising its capacity to track both mental and physical function. The development of electrochemical biosensors as dependable instruments for their detection is next covered, along with an examination of important oxidative stress indicators. These biosensors are perfect for continuous and non-invasive health monitoring since they have real-time sensing capabilities and can be easily integrated with wearable electronic platforms.

2. Salivary oxidative stress biomarkers

Saliva has drawn interest as a diagnostic fluid since it is simple to collect, requires little training, and can be self-collected, making it available to a variety of people, including young children and the elderly. Samples are convenient since they may be collected in a variety of locations, including at home or work. Biomolecules such as proteins, hormones, and enzymes found in saliva are connected to stress, illness, and general well-being [15]. Saliva-based diagnostic tests for ailments like stress, mental health, and oral disorders have been developed as a result of these advantages. However, there are still issues like pollutants, individual biomarker variance, and temporal lags between blood and saliva changes. Saliva's non-invasiveness, ease of collection, and capacity to track a variety of biomarkers connected to stress, illness, and general health have made it a potential diagnostic fluid.

Proteins, enzymes, and hormones are just a few of the macromolecules found in saliva that represent physiological alterations linked to illness and stress. Salivary α-amylase, chromogranin A (CgA), cortisol, brain-derived neurotrophic factor (BDNF), and immunoglobulin A (IgA) are some of the biomarkers frequently examined in stress research [16],[17],[18]. For example, both acute and chronic stress cause an increase in salivary α-amylase, whereas cortisol levels rise during acute stress but may become dysregulated under chronic stress. Stress usually causes immunoglobulin A levels to drop, which is a sign of immunological suppression. Increased levels of CgA, a protein generated by the adrenal glands under stress, are seen under both acute and chronic stress. CgA is also used to measure alterations associated with stress [19].

Furthermore, stress can affect BDNF, a growth factor implicated in brain plasticity, which exhibits higher levels during acute stress but lower levels under chronic stress [20]. Saliva has a lot of promise for diagnostics; however, there are still issues with biomarker variability because of things like sample collecting techniques, time lags between blood and saliva changes, and individual variations in concentration gradients. Saliva, however, provides an easy-to-use way to track health and stress reactions, and research is being done to maximise its utility in clinical settings.

One well-researched ROS that serves as a signalling molecule and an indication of oxidative imbalance is hydrogen peroxide (H_2O_2) [21]. The nitration of tyrosine residues in proteins produces 3-nitrotyrosine (3-NT), a particular marker that indicates oxidative and nitrosative damage [22]. Through their involvement in redox-sensitive signalling cascades, protein phosphorylation levels, which are changed in oxidative environments, also function as indirect indicators. As an indicator of oxidative DNA damage, 8-Hydroxy-2'-deoxyguanosine (8-OHdG) is one of the most researched oxidative stress biomarkers currently being explored. Furthermore, 3-nitrotyrosine (3-NT) has emerged as a crucial indicator of protein nitration, indicating oxidative protein damage [4]. Reactive oxygen species (ROS), which are a direct indicator of oxidative stress levels, and Malondialdehyde (MDA), a byproduct of lipid peroxidation, are also important indicators of oxidative imbalance in the body [23]. The increased attention paid to these biomarkers, in particular, 8-OHdG, 3-NT, and MDA, highlights their potential for real-time oxidative stress monitoring and early disease diagnosis, offering insight into the mechanisms driving stress and related illnesses. Table 2 represents the electrochemical biosensors for Key salivary oxidative stress biomarkers

The pre-analytical stability of saliva oxidative indicators varies greatly with temperature, storage period, and enzymatic activity. Saliva, as opposed to blood, is abundant in enzymes such as amylase and proteases that can hydrolyse biomarkers for MDA, 3-nitrotyrosine, and 8-OHdG as soon as they are sampled. Studies have shown that biomarker concentrations significantly decrease within 30 to 60 minutes if cooling is delayed or protease inhibitors are not added. Effective sample handling requires fast chilling, storage at −20°C or lower, and the absence of freeze-thaw cycles. Accuracy may also be impacted by consistency in salivary flow and collection methods. Hence, standardised methods are important for biosensor-based diagnoses to be reliable.

3. Comparative analysis of the diagnostic accuracy of salivary oxidative stress biomarkers: Saliva vs blood, urine and cerebrospinal fluid (CSF)

Table 1:
Comparative analysis of biofluids for detection of oxidative stress biomarkers.

Parameter	Blood/Serum	Urine	CSF	Saliva
Invasiveness	High	Moderate	High	None
Sample Volume Needed	Moderate to High	Moderate to High	High	Low
Biomarker Stability	High (under storage)	Moderate	High	Low (enzyme activity)
Real-time Monitoring	Difficult	Not practical	Not practical	Easily achievable
Point-of-Care Compatibility	Limited	Moderate	Poor	Excellent
Cost and Simplicity	Expensive	Moderate	Expensive	Low-cost
Clinical Standardization	Established	Partial	Established	Emerging

Saliva offers a practical, easily available, non-invasive biofluid for evaluating oxidative stress biomarkers, but its diagnostic accuracy in comparison to more conventional fluids such as blood, urine, and cerebrospinal fluid (CSF) remains a major problem. Table 1 shows the comparative analysis of biofluids for detection of oxidative stress biomarkers. Because of things like selective diffusion across acinar cells, active transport processes, and enzymatic degradation by salivary enzymes like amylase and peroxidase, the levels of oxidative stress indicators in saliva are often significantly lower than in plasma or CSF. For example, the levels of 8-hydroxy-2′-deoxyguanosine (8-OHdG) in plasma can range from 0.2 to 1.0 ng/mL, whereas in saliva they are normally between 0.05 and 0.3 ng/mL [24]. Malondialdehyde (MDA) and 3-nitrotyrosine can also be found in saliva, although in smaller amounts than in blood. Despite these variations, several studies have demonstrated statistically significant relationships between oxidative stress marker concentrations in serum and saliva in clinical populations, such as patients with neurological disorders, diabetes, and cardiovascular disease [9],[21].

Additionally, saliva can be collected by self-collection to reduce patient discomfort and contamination risk, unlike blood and CSF, which require invasive procedures and specialised care. According to Monosik et al. [11], this makes saliva the best material for repeated or real-time monitoring, especially when paired with electrochemical biosensor technologies that offer great sensitivity and specificity at low analyte concentrations. However, pre-analytical factors such as sample collection method, circadian rhythms, hydration, and food intake can affect biomarker levels, reducing the diagnostic utility of saliva. Furthermore, unless processed or stabilised immediately, saliva may degrade labile biomarkers due to its increased susceptibility to biochemical instability brought on by enzymatic activity and pH fluctuations. However, the detection of salivary oxidative stress biomarkers at clinically relevant concentrations has significantly improved with recent developments in wearable biosensing technologies, molecularly imprinted polymers, and nanomaterials. Saliva-based diagnostics can therefore provide a scalable, affordable, and efficient substitute for traditional fluids with the right standardisation and validation, especially for point-of-care and personalised treatment.

4. Electrochemical Biosensing Principle

The principles of electrochemistry, which investigate the connection between electrical energy and chemical reactions, specifically, redox processes, in which electrons are transported between molecules, form the basis of electrochemical sensing techniques [25]. Since many biological processes, including cellular respiration and neural activity, depend on these reactions, electrochemical techniques are extremely important for use in biomedical and diagnostic settings [26]. The measurement of electrical current produced by redox reactions at electrode surfaces is the fundamental component of electrochemical detection. This current enables accurate quantitative analysis since it is proportional to the target analyte's concentration.

Important methods include electrochemical impedance spectroscopy (EIS), which examines the resistance to charge transfer at the electrode interface; amperometry, which keeps a constant potential to track changes in current in real time; and voltammetry, which varies the potential and the current that results reveals the redox behavior of analytes [27]. These techniques provide great sensitivity, quick reaction, and the capacity to identify biomarkers at trace levels in complicated matrices like blood or saliva, particularly when supplemented with nanomaterials or molecularly imprinted polymers (Figure 1). They are essential instruments in contemporary biosensing because of their versatility and diagnostic capabilities, especially when it comes to identifying disease-associated biomarkers like 3-nitro-L-tyrosine.

4.1. Electrochemical sensing of 8-Hydroxy-2'-deoxyguanosine

Targeting nucleotides, nucleosides, and DNA bases, oxidative stress can cause damage to genomic DNA. Guanine is particularly susceptible because of its low oxidation potential [28]. 8-oxoguanine (8-oxoG) and its deoxynucleoside form, 8-hydroxy-2′-deoxyguanosine (8-OHdG), are the main oxidation products of guanine [29]. Since these substances are the most common and well-established indicators of oxidative DNA damage, 8-OHdG is frequently utilised as an indicator to evaluate oxidative stress at the molecular level. A number of electrochemical platforms have been created to detect 8-oxodG, a biomarker of oxidative DNA damage, with high sensitivity. The sensitive and selective electrochemical detection of 8-oxodG, a crucial indicator of oxidative DNA damage, has been thoroughly investigated using conducting polymers, nanostructured materials (NsM), and biomolecular recognition components. Peak currents were improved and oxidation potentials were shifted to more negative values by electropolymerized films such as poly(3-methylthiophene) (P3MT) and poly(3-acetylthiophene) (P3AT) modified glassy carbon electrodes (GCE). The detection limits of these systems were as low as 0.10 µM and 31.3 nM, respectively [30],[31]. With LODs of 56 nM, mixed DNA–P3MT films likewise showed excellent sensitivity. To improve selectivity for 8-oxoG and guanine, metallopolymers such as $[Os(bpy)_2(PVP)_{10}Cl]^+$ and $[Ru(bpy)_2(PVP)_{10}Cl]^+$ were employed [32]. When 8-oxodG was present during the synthesis of molecularly imprinted polymers (MIPs), highly selective recognition sites were made possible, resulting in LODs as low as 3 nM and even 0.74 pg/mL (≈2.6 pM) [33],[34]. With LODs as low as 100 fg/mL, immunosensors that used 8-oxodG antibodies mounted on electrodes modified with nanomaterials (such as ZnO nanorods or rGO) showed exceptional selectivity and detection capabilities [35]. Because of their non-immunogenic nature, low cost, and great specificity, aptamer-based sensors have become extremely useful in-

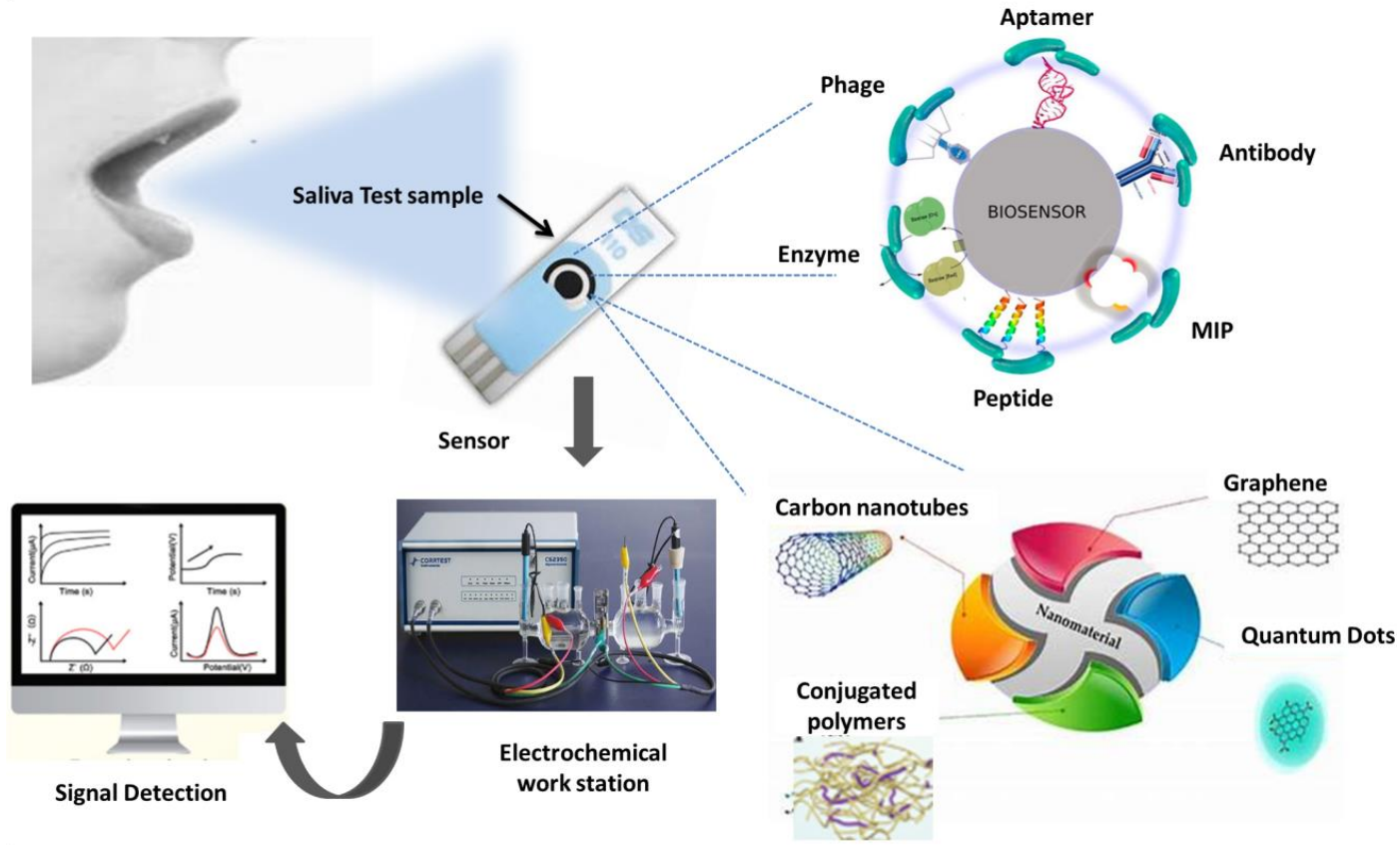

Figure 1. *A visual representation of biosensor for electrochemical detection of oxidative stress biomarkers in saliva*.

struments. Novel designs that combined aptamers with DNAzymes, hybridisation chain reaction (HCR), and other signal amplification techniques produced ultralow LODs down to 24.34 fM while preserving great selectivity against interfering compounds and wide linear ranges [36]. Together, these cutting-edge electrochemical platforms, which include polymers, nanomaterials, MIPs, dendrimers, immunosensors, and aptasensors, provide reliable, sensitive, and specific methods for detecting 8-oxodG in intricate biological matrices, thereby bolstering their potential for use in oxidative stress monitoring and clinical diagnostics.

4.2. Electrochemical sensing of Malondialdehyde

As a byproduct of the oxidation of arachidonic acid (AA), an unsaturated fatty acid, malondialdehyde (MDA) is a key biomarker of lipid peroxidation and oxidative stress. Therefore, it is essential to develop trustworthy techniques for its detection in plasma, serum, and salivary fluid, as monitoring MDA levels in biological systems can be used to determine oxidative stress. Lipid peroxidation products have been identified using both chemical and electrochemical methods. Yuan et al. [37] used multi-walled carbon nanotubes (MWNTs) to create a label-free electrochemical biosensor for MDA detection (Figure 2). After MWNTs and chitosan (CS) were added to a glassy carbon electrode (GCE), glutaraldehyde (GluA), complement factor H (CFH), and bovine serum albumin (BSA) were immobilised to act as links, recognition, and blocking agents, respectively. Every alteration step was validated by cyclic voltammetry (CV) and electrochemical impedance spectroscopy (EIS). While subsequent surface alterations raised resistance and decreased current, suggesting effective layer development, MWNTs improved electron transport. Using differential pulse voltammetry (DPV), the sensor obtained a linear range of 0.1–90 µmol¹ and a detection limit of 0.047 µmol¹; however, stability data were not provided.

Later, a study showed that layer-by-layer nanocomposites made of polymers and nanoparticles performed exceptionally well electroanalytically and in terms of conductivity [38]. MDA was detected in exhaled breath condensate via DPV using quantum dots and polyarginine, with a detection limit of 0.329 nM. For the detection of MDA in breath and serum, Hasanzadeh et al. [23] used a polypurine-modified gold electrode (PT/Au), which produced good stability (90 percent signal retention after 100 analyses), a linear range of 0.78–3.10 mM, and a detection limit of 34 nM. The conductive polymers and nanomaterials' high conductivity, vast surface area, and abundance of active sites are what give these studies their improved performance.

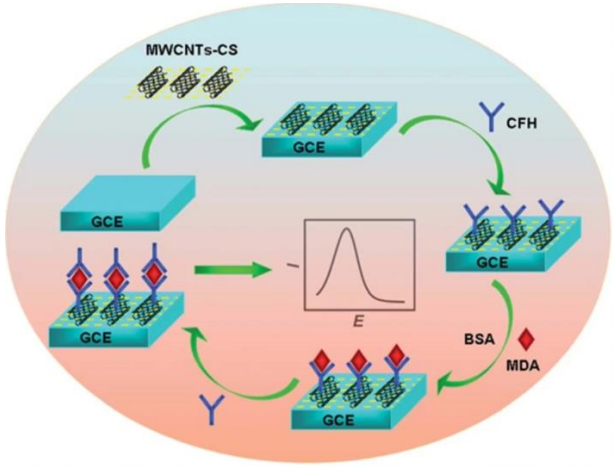

Figure 2. *An illustration showing how the synthesis of label-free biosensors for MDA detection* [37].

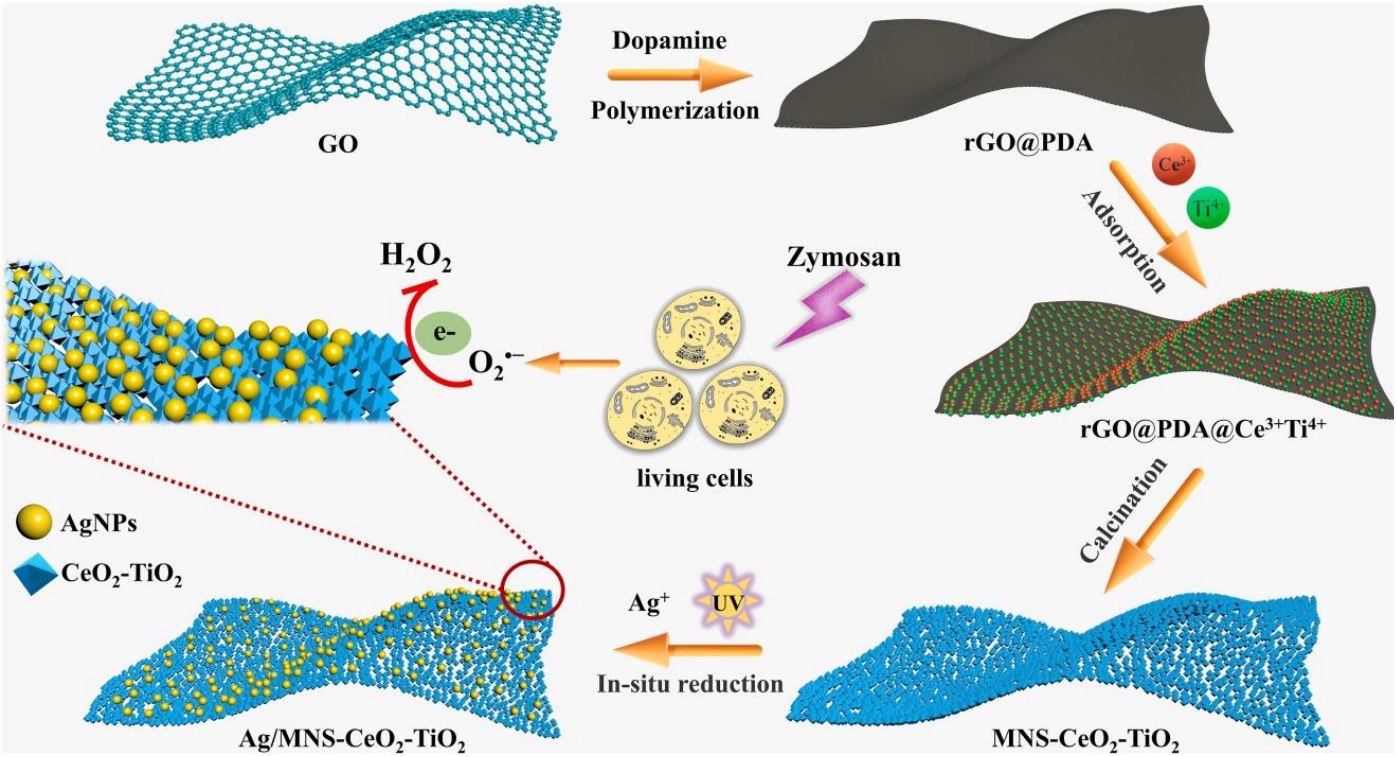

Figure 3. *Development of Ag/MNS-CeO_2-TiO_2 materials and the identification of superoxide anions generated by cells* [42].

4.3. Electrochemical sensing of Malondialdehyde

Electrochemical detection of reactive oxygen and nitrogen species (ROS/RNS) is one of the effective methods for tracking oxidative stress in biological fluids, specifically in saliva. ROS and RNS are immediately detected by chemical sensors at their distinctive redox potentials. For instance, the oxygen/superoxide redox pair is detected at about -0.33 V versus NHE, whereas nitric oxide (NO) is oxidised at about 0.8 V vs Ag/AgCl [1]. Amatore et al. [39] and associates' groundbreaking research using platinumized carbon microelectrodes to identify ROS/RNS in individual cells and even inside phagolysosomes. Catalytic materials, such as Prussian blue composites or gold nanocones, are employed to boost sensitivity and further enhance performance. This allows for the detection of hydrogen peroxide (H_2O_2) at low concentrations, even in complicated samples like blood or serum.

In contrast, biological sensors use redox-active proteins that are immobilised on the electrode surface in order to selectively identify the target species. For example, superoxide ($O_2^{-\cdot}$) can be detected using cytochrome c (Cyt C), which facilitates electron

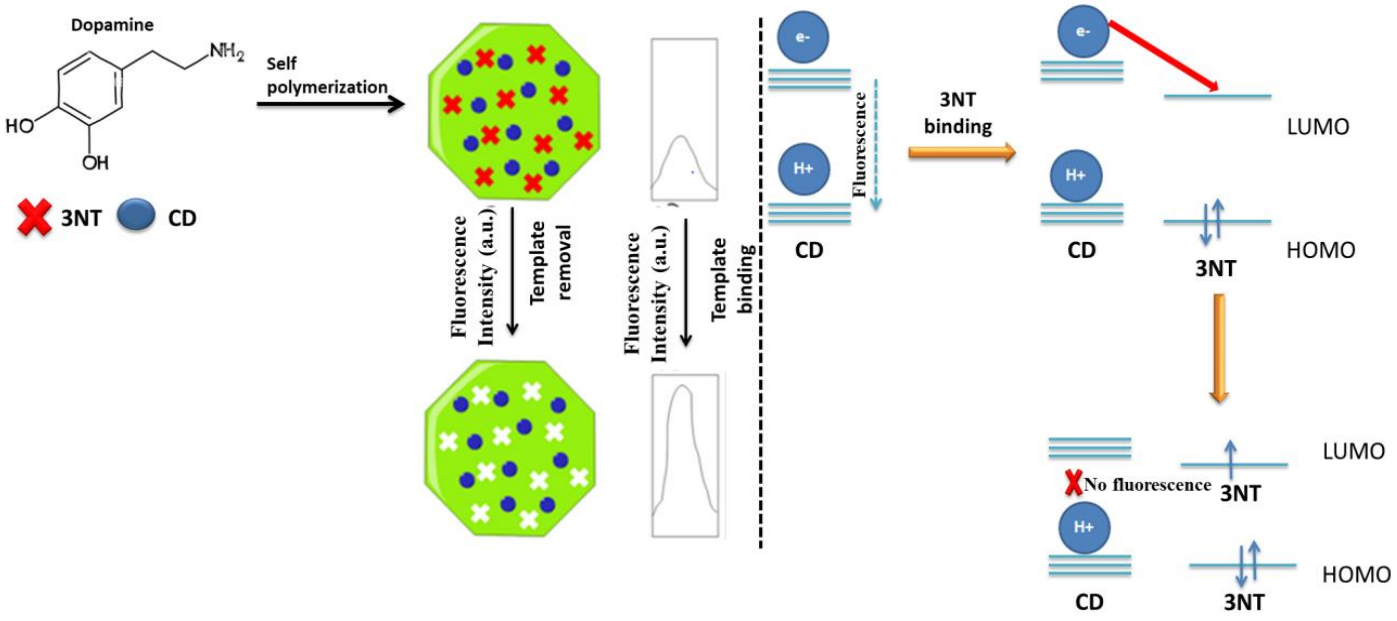

Figure 4. *The BMIP@CDs sensor's fluorescence quenching mechanism* [47].

transfer upon binding and produces a detectable biocatalytic current [40]. Despite the excellent selectivity of these biosensors, their long-term stability and immobilisation complexity can be problematic. More recent methods use hybrid nanomaterials like graphene/AgNP/CeO_2/TiO_2 or enzyme mimetics like $MnTiO_3$ or manganese phosphate (Figure 3) to more robustly simulate enzymatic activity [41],[42].

Because of their short half-life and reactivity, NO and its reactive product, peroxynitrite, require sensors with high sensitivity and fast response [43]. Selectivity is frequently attained by covering CFMEs with selective barriers such as Nafion, chitosan, or o-phenylenediamine since NO oxidises at potentials that overlap with those of other species [44]. Recent developments include Cyt c-modified nanoporous gold electrodes that have low detection limits and great sensitivity for detecting $O_2^{-\cdot}$ in tissues such as skeletal muscle [45]. Even with these developments, further research is required to confirm the specificity of some of the more recent materials, especially in intricate biological settings.

4.3. Electrochemical sensing of 3-Nitrotyrosine (3-NT)

Using a variety of materials and methods, several novel sensors have been created for the detection of 3-nitrotyrosine (3-NT), a crucial indicator of oxidative stress. For precise 3-NT detection in biological fluids, Govindasamy et al. [46] developed an amperometric sensor based on cadmium tungstate nanodots with reduced graphene oxide. This sensor has a low detection limit (LOD) of 3.24 nM, a broad linear range (18.5 nM to 1.84 mM), and good sensitivity. Similar to this, Jalili et al. [47] reported a new molecularly imprinted polymer (MIP) sensor that uses green-light emitting carbon dots (BMIP@CD) showed good serum analysis with high recovery and repeatability (Figure 4). It is less expensive and more resilient than antibody-based sensors.

Additionally, lab-on-a-chip electrochemical paper-based sensors provide a portable, affordable solution for point-of-care diagnostics with a limit of detection of 49.2 nM. In serum from patients with minor hepatic encephalopathy, optical sensors such as a binuclear platinum complex demonstrated remarkable sensitivity (LOD: 4.7×10^{-10} M) and selectivity for 3-NT detection [48]. The LOD of 25.14 pM provided by copper ferrite nanodots embedded in reduced graphene oxide was exceptionally low [49]. While surface acoustic wave (SAW) biosensors in conjunction with electrospray ionisation-mass spectrometry allowed for label-free analysis of nitrated peptides, electrochemical sensors that included MIP-doped gold nanoparticles demonstrated good specificity and sensitivity with a limit of detection of 50 nM [50]. A localised surface plasmon resonance (NDG-LSPR) sensor based on graphene doped with nickel showed good selectivity for 3-NT and a limit of detection of 0.13 pg/mL [51].

Outperforming conventional ELISA techniques, bimetallic Fe/Pd nanoparticles with molecular imprinting provided a durable, affordable, and efficient instrument for 3-NT detection in clinical fluids [52]. Finally, immunofluorescent detection of 3-NT-modified tyrosine residues under oxidative circumstances was made possible by peptide-functionalized fluorescent particles (PFFPs), supporting applications in therapeutic screening and disease monitoring [51]. These new developments demonstrate the expanding potential of sophisticated sensors in the evaluation of clinical oxidative stress.

Table 2:

Electrochemical Biosensors for Key Salivary Oxidative Stress Biomarkers. (ITO: indium tin oxide; AuNTAs: gold nanotriangles arrays; PtNPs: platinum nanoparticles; DPV: differential pulse voltammetry; SWCNT: single-wall carbon nanotubes; GCE: glassy carbon electrode; MWCNT: multiwalled carbon nanotubes; **ErGO**: electrochemically reduced graphene oxide; SWV: square wave voltammetry; CV: cyclic voltammetry; **SPCE**: screen-printed carbon electrode; **MGO**: magnetic graphene oxide; MIPy: molecularly imprinted polypyrrole; $La_2Sn_2O_7$: lanthanum stannate; f−HNT: functionalized halloysite nanotubes; **MIP**: molecularly imprinted polymer; **AMWCNT**: aminated multi-walled carbon nanotubes; **GONRs**: graphene oxide nanoribbons; **MoS_2**: molybdenum disulfide; **$BiVO_4$:** bismuth vanadate; **ZSM-5:** zeolite socony mobil-5; $Mn_3(PO_4)_2$: manganese(II) phosphate; PDDA: Poly(diallyldimethylammonium chloride); AMP: amperometery).

No.	Biomarker	Material	Technique	LOD	Reference(s)
1	8-OHdG	ITO/AuNTAs/PtNPs portable electrochemical device	DPV	10 ng/mL–100 µg/mL	[53]
2	8-OHdG	SWCNT-Nafion/GCE	DPV	0.03–1.25 µM	[54]
3	8-OHdG	MWCNT/ErGO/GCE	(SWV)	3–75 µM	[55]
4	MDA	GCE/MWCNTs	CV	0.02–40 µM	[37]
5	MDA	SPCE/MGO@MIPy	DPV	0.01–100 µM	[56]
6	3-NT	$La_2Sn_2O_7$/f−HNT	DPV	0.5–214 µM	[57]
7	3-NT	MIP/AMWCNT@GONRs	DPV	0.2–50.0 µM	[50]
8	3-NT	MoS_2@$BiVO_4$	CV	0.001–526.3 µM	[58]
9	ROS	ITO/ZSM-5, $Mn_3(PO_4)_2$, PDDA	Amp	5.0×10^{7} – 1.2×10^{3} dm^2/L	[59]
10	ROS	Ceria-nanoparticle nanozyme on SPCE	CV	1- 100 µM	[60]

5. Recent Advances in Saliva-Based Electrochemical Biosensors

More attention must be paid to emerging illnesses associated with oxidative stress, especially in light of quick and easy diagnostics. Improvements in biosensor technology, such as the creation of wearable and mouthguard-based electrochemical biosensors, are desperately needed. For point-of-care (POC) applications, these cutting-edge technologies have great potential since they enable the early and non-invasive detection of oxidative stress indicators, which is essential for prompt diagnosis and efficient disease management.

Enhancing the sensitivity, selectivity, and mobility of electrochemical biosensors for a salivary oxidative stress indicator has been the main focus of recent advancements. The electrochemical characteristics of sensor platforms have been greatly improved by the introduction of nanostructured materials such as graphene oxide, carbon nanotubes, and gold nanoparticles. Furthermore, biomarker recognition has improved with the use of molecularly imprinted polymers (MIPs), particularly for 3-nitrotyrosine and 8-OHdG. The prohibitive expense of high-end nanomaterials such as gold nanoparticles and graphene constrains the mass production of salivary electrochemical biosensors [61]. Although the cost of synthesis and purification is significant, these materials function exceptionally well [62]. To combat this, research is being done on low-cost substitutes such as metal oxides, polymer nanocomposites, and carbon produced from biomass, which show comparable sensitivity at a lower cost [63]. Similarly, green solvents and electropolymerization are used to optimise molecularly imprinted polymers (MIPs), reducing production costs [64]. For point-of-care applications, pairing with screen-printed electrodes and paper-based platforms also makes mass production affordable.

Real-time monitoring of salivary biomarkers linked to oxidative stress has been transformed by the combination of wearable technology with electrochemical biosensing. The goal of these developments is to offer continuous, non-invasive, and customised health monitoring options.

Mouthguard biosensors that can identify salivary metabolites have been developed thanks to creative designs. An instrumented mouthguard that non-invasively measures salivary uric acid levels was demonstrated by Kim et al. [65]. To enable real-time wireless data transfer to smartphones and other devices, this device combines a uricase-modified screen-printed electrode system with miniature electronics, such as a potentiostat, microprocessor, and Bluetooth Low Energy (BLE) transmitter. OECTs have the potential to be used in wearable biosensors, providing enhanced sensitivity and signal amplification for the detection of low-abundance analytes, as demonstrated by Duan et al. [66]. These gadgets make it easier to track salivary biomarkers in real-time, which improves point-of-care diagnostic performance. Wearable biosensors can be seamlessly integrated with cell phones thanks to the use of wireless connection modules. Proactive health management is supported by this connectivity, which allows consumers to share data with healthcare providers, follow health measures over time, and get rapid feedback.

Wearable electrochemical biosensors for salivary analysis are now much more functional and user-friendly thanks to the development of wireless and microfluidic technology. Figure 5 shows the evolution of wearable electrochemical sensors based on bioreceptors. Wearable biosensors have integrated microfluidic devices to effectively handle tiny amounts of saliva. These technologies make it easier to handle samples precisely, use fewer reagents, and allow multiplexed detection of different biomarkers. For instance, wearable technology with microfluidic channels can track salivary metabolites like uric acid and lactate over time, giving important information about a person's level of oxidative stress.

6. Challenges and Limitations

Age, food, oral health, circadian rhythm, and other physiological and lifestyle factors all affect the baseline levels of oxidative stress indicators in saliva [67]. Age-related alterations in redox metabolism can alter the levels of oxidative stress markers; older individuals often exhibit higher levels of MDA and 8-OHdG due to accumulated oxidative damage and weakened antioxidant defences [68]. Another crucial factor is nutrition; for example, consuming

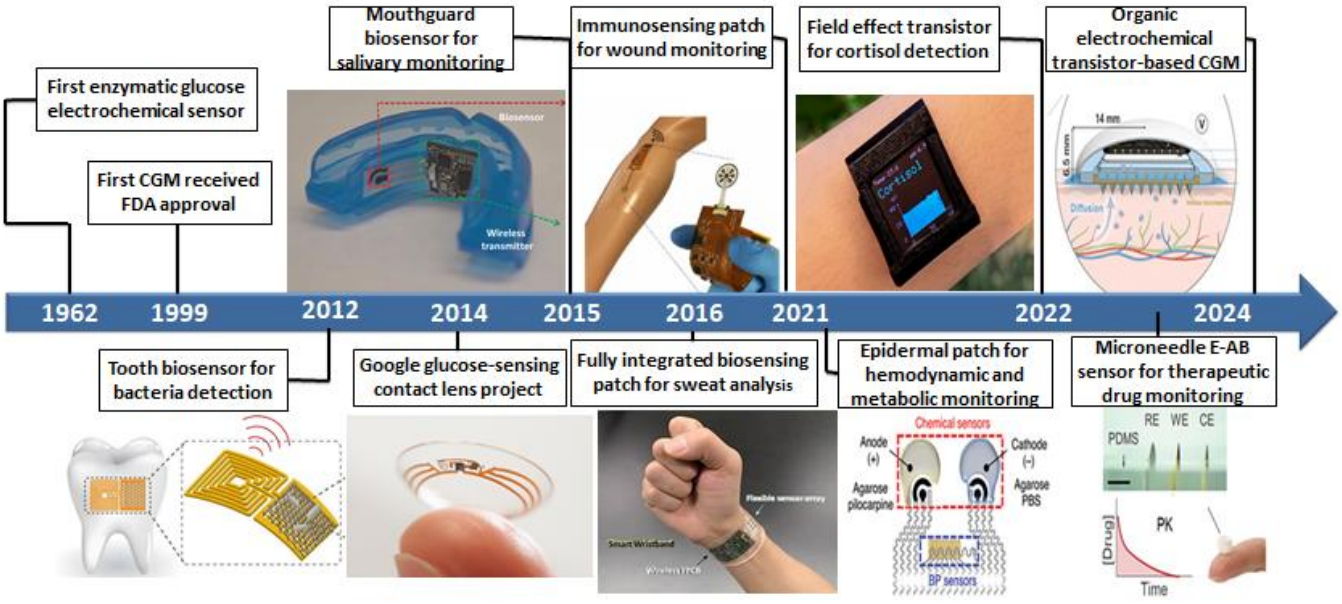

Figure 5. *The evolution of wearable electrochemical sensors based on bioreceptors* [66].

too many processed foods or polyunsaturated fats can increase lipid

peroxidation and, in turn, MDA levels, whereas diets high in antioxidants have been demonstrated to suppress the production of biomarkers. Another important factor is oral health; independent of systemic health, gingivitis or periodontitis can cause local oxidative stress and artificially raise salivary ROS and 3-nitrotyrosine levels. Salivary biomarkers have also been shown to exhibit circadian rhythms; for example, cortisol and 8-OHdG are two analytes that peak in the morning and then decline throughout the day. False-positive or false-negative diagnoses are more likely when these physiological variations are not taken into consideration. Therefore, it is essential to standardise sample timing of collection and account for individual physiological characteristics to provide valid clinical interpretation and calibration of biosensors.

A number of significant restrictions and difficulties prevent saliva-based electrochemical biosensors for oxidative stress indicators from being widely used in clinical settings and being commercialised. Target biomarkers like 3-nitrotyrosine (3-NT), 8-hydroxy-2′-deoxyguanosine (8-OHdG), Malondialdehyde (MDA), and reactive oxygen species (ROS) are among the most important problems. These biomarkers are frequently found in saliva at nanomolar to picomolar concentrations, which calls for ultra-sensitive detection techniques. Saliva's complex and varied composition, which includes variations in pH, protein content, viscosity, and enzyme activity brought on by dietary changes, circadian rhythms, or personal health conditions, can also have a substantial impact on sensor performance, resulting in inconsistent and poor reproducibility [24].

The non-specific adsorption of salivary proteins and other interfering chemicals onto the sensor surface is another significant drawback. This can lead to electrode fouling, signal instability, and a gradual decrease in sensitivity [69]. The absence of defined procedures for the collection, handling, and processing of saliva further complicates matters, making it challenging to compare findings across several platforms or research studies. Additionally, selectivity is still problematic, especially when sensors exhibit cross-reactivity with compounds that share structural similarities, leading to erroneous results.

Furthermore, a lot of biosensors depend on biological recognition components like enzymes or antibodies, which are naturally unstable and have short shelf lives, particularly in environments with variable humidity or temperature [70]. Although it holds promise for real-time, non-invasive diagnostics, the incorporation of these sensors into wearable platforms introduces another level of complexity because it necessitates robust miniaturisation, power efficiency, wireless data transmission, and biocompatibility, all of which raise production costs and technical obstacles. Lastly, batch-to-batch variability frequently plagues sensor fabrication techniques, especially those employing nanomaterials or molecularly imprinted polymers. This compromises repeatability and restricts scalability for mass production. All of these drawbacks point to the necessity of ongoing advancements in sensor design, fabrication methods, and materials to fully utilise saliva-based electrochemical biosensors in oxidative stress diagnostics.

7. Future Perspectives

The area of electrochemical biosensing based on saliva is on the brink of major change, fueled by material sciences development, wearable technology, and integration into digital health. The incorporation of biosensors into Internet of Things (IoT) systems and smart wearables is the main focus of future development. This will enable wireless data transfer and remote clinician input, enabling continuous real-time monitoring of biomarkers for oxidative stress. Early disease identification and proactive healthcare will be made possible by this. Meanwhile, advancements in next-generation low-cost nanomaterials such as carbon quantum dots, metal-organic frameworks (MOFs), and biodegradable polymers are expected to enhance sensor performance while permitting ecologically benign, large-scale manufacture. When combined with hybrid detection modes (electrochemical, optical, and enzymatic), multiplex biosensors that can simultaneously detect multiple oxidative stress indicators such as 3-nitrotyrosine, 8-OHdG, MDA, and ROS will yield more comprehensive diagnostic data, improving analytical accuracy and cross-validation.

With the help of artificial intelligence (AI) and machine learning (ML), data interpretation will be transformed into pattern recognition and real-time health analytics. This includes the possibility of profiling an individual's oxidative stress based on their physiology, lifestyle, and medical history. Furthermore, to comply with regulatory standards and facilitate commercialisation, future progress will be fueled by overcoming current constraints through the standardisation of sample harvest, calibration processes, and clinical verification. Miniaturising biosensors based on self-powered systems, such as triboelectric nanogenerators (TENGs) or biofuel cells, is another exciting avenue. This will eliminate the need for external power sources and allow for the creation of completely autonomous, non-invasive devices. With the potential to significantly improve public health through early diagnosis, tailored treatment, and real-time health monitoring, these novel developments collectively position saliva-based electrochemical biosensors as a cornerstone of next-generation non-invasive diagnostics.

8. Conclusion

In conclusion, saliva-based electrochemical biosensors have a lot of promise for real-time, non-invasive monitoring of oxidative stress biomarkers, providing a viable path toward early disease detection and individualised health care. The sensitivity, selectivity, and convenience of these biosensors have been significantly improved by the combination of wearable technology, molecularly imprinted polymers, and sophisticated nanomaterials. Recent advances, such as mouthguard biosensors and microfluidic systems, have shown impressive progress despite obstacles such as biomarker variability, sample collection problems, and the requirement for device uniformity. These advancements, especially in wearable technology, have the potential to revolutionise the diagnostics industry by facilitating ongoing health monitoring using user-friendly, accessible gadgets. Saliva-based electrochemical biosensors, which provide a non-invasive, effective way to monitor oxidative stress and enhance health outcomes, are set to play a significant part in the future of personalised healthcare as research and technology develop.

Declaration

Competing Interests: The authors declare that they have no known competing financial interests or personal relationships that could have appeared to influence the work reported in this paper.

Ethical Issues: There are no ethical issues. All data in this paper is publicly available.

Author Contribution Statement: H.K.M, A.A. and H.F. conceived the idea and designed the research; analysed and interpreted the data and wrote the paper.

Funding Statement: This research did not receive any specific grant from funding agencies in the public, commercial, or not-for-profit sectors.

Consent to Publish: All authors have agreed to publish the version of the manuscript in this journal.

References

1. S. Deshpande, W. Muraoka, and S. Andreescu, "Electrochemical sensors for oxidative stress monitoring," Curr. Opin. Electrochem., vol. 29, p. 100809, Oct. 2021, doi: 10.1016/j.coelec.2021.100809.
2. M. P. Murphy et al., "Unraveling the Biological Roles of Reactive Oxygen Species," Cell Metab., vol. 13, no. 4, pp. 361–366, Apr. 2011, doi: 10.1016/j.cmet.2011.03.010.
3. M. Schrader and H. D. Fahimi, "Peroxisomes and oxidative stress," Biochim. Biophys. Acta BBA - Mol. Cell Res., vol. 1763, no. 12, pp. 1755–1766, Dec. 2006, doi: 10.1016/j.bbamcr.2006.09.006.
4. K. M. Nash, A. Rockenbauer, and F. A. Villamena, "Reactive Nitrogen Species Reactivities with Nitrones: Theoretical and Experimental Studies," Chem. Res. Toxicol., vol. 25, no. 8, pp. 1581–1597, Aug. 2012, doi: 10.1021/tx200526y.
5. H. Sies and D. P. Jones, "Reactive oxygen species (ROS) as pleiotropic physiological signalling agents," Nat. Rev. Mol. Cell Biol., vol. 21, no. 7, pp. 363–383, Jul. 2020, doi: 10.1038/s41580-020-0230-3.
6. Y. Chen, M. B. Azad, and S. B. Gibson, "Superoxide is the major reactive oxygen species regulating autophagy," Cell Death Differ., vol. 16, no. 7, pp. 1040–1052, Jul. 2009, doi: 10.1038/cdd.2009.49.
7. A. Andries, J. Rozenski, P. Vermeersch, D. Mekahli, and A. Van Schepdael, "Recent progress in the LC–MS/MS analysis of oxidative stress biomarkers," ELECTROPHORESIS, vol. 42, no. 4, pp. 402–428, 2021, doi: 10.1002/elps.202000208.
8. H. Togashi, M. Aoyama, and K. Oikawa, "Imaging of reactive oxygen species generated in vivo," Magn. Reson. Med., vol. 75, no. 3, pp. 1375–1379, 2016, doi: 10.1002/mrm.25582.
9. M. A. Javaid, A. S. Ahmed, R. Durand, and S. D. Tran, "Saliva as a diagnostic tool for oral and systemic diseases," J. Oral Biol. Craniofacial Res., vol. 6, no. 1, pp. 67–76, Jan. 2016, doi: 10.1016/j.jobcr.2015.08.006.
10. W. V. Giannobile, T. Beikler, J. S. Kinney, C. A. Ramseier, T. Morelli, and D. T. Wong, "Saliva as a diagnostic tool for periodontal disease: current state and future directions," Periodontol. 2000, vol. 50, pp. 52–64, 2009, doi: 10.1111/j.1600-0757.2008.00288.x.
11. R. Monošík, M. Stred'anský, and E. Šturdík, "Application of Electrochemical Biosensors in Clinical Diagnosis," J. Clin. Lab. Anal., vol. 26, no. 1, pp. 22–34, 2012, doi: 10.1002/jcla.20500.
12. M. U. Javed et al., "Metal-Organic Framework/Polymer Composites for Solid State Electrolytes-A Critical Review," J. Power Sources, vol. 640, p. 236720, Jun. 2025, doi: 10.1016/j.jpowsour.2025.236720.
13. F. J. Iftikhar, A. Shah, Q. Wali, and T. Kokab, "Advancements in Nanofiber-Based Electrochemical Biosensors for Diagnostic Applications," Biosensors, vol. 13, no. 4, Art. no. 4, Apr. 2023, doi: 10.3390/bios13040416.
14. Y. Li, "Molecularly imprinted polymer-based electrochemical biosensors for biomarkers detection," Doctoral, UCL (University College London), 2024. Accessed: May 17, 2025. [Online]. Available: https://discovery.ucl.ac.uk/id/eprint/10195540/
15. I. D. Mandel, "Sialochemistry in Diseases and Clinical Situations Affecting Salivary Glands," CRC Crit. Rev. Clin. Lab. Sci., vol. 12, no. 4, pp. 321–366, Jan. 1980, doi: 10.3109/10408368009108733.
16. U.-M. Bailey, C. Punyadeera, J. J. Cooper-White, and B. L. Schulz, "Analysis of the extreme diversity of salivary alpha-amylase isoforms generated by physiological proteolysis using liquid chromatography–tandem mass spectrometry," J. Chromatogr. B, vol. 911, pp. 21–26, Dec. 2012, doi: 10.1016/j.jchromb.2012.10.023.
17. Y. Kanamaru, Kikukawa ,Azusa, and K. and Shimamura, "Salivary chromogranin-A as a marker of psychological stress during a cognitive test battery in humans," Stress, vol. 9, no. 3, pp. 127–131, Jan. 2006, doi: 10.1080/14769670600909594.
18. F. P. Idris, Y. Wan, X. Zhang, and C. Punyadeera, "Within-Day Baseline Variation in Salivary Biomarkers in Healthy Men," OMICS J. Integr. Biol., vol. 21, no. 2, pp. 74–80, Feb. 2017, doi: 10.1089/omi.2016.0168.
19. M. A. D'amico, B. Ghinassi, P. Izzicupo, L. Manzoli, and A. D. Baldassarre, "Biological function and clinical relevance of chromogranin A and derived peptides," Jun. 2014, doi: 10.1530/EC-14-0027.
20. A. L. Mandel, Ozdener ,Hakan, and V. and Utermohlen, "Brain-Derived Neurotrophic Factor in Human Saliva: Elisa Optimization and Biological Correlates," J. Immunoassay Immunochem., vol. 32, no. 1, pp. 18–30, Jan. 2011, doi: 10.1080/15321819.2011.538625.
21. D. Tsikas, "Analytical methods for 3-nitrotyrosine quantification in biological samples: the unique role of tandem mass spectrometry," Amino Acids, vol. 42, no. 1, pp. 45–63, Jan. 2012, doi: 10.1007/s00726-010-0604-5.
22. S. Maheshwaran et al., "An Ultra-sensitive Electrochemical Sensor for the Detection of Oxidative Stress Biomarker 3-Nitro-l-tyrosine in Human Blood Serum and Saliva Samples Based on Reduced Graphene Oxide Entrapped Zirconium (IV) Oxide," J. Electrochem. Soc., vol. 167, no. 6, p. 066517, Apr. 2020, doi: 10.1149/1945-7111/ab847d.
23. M. Hasanzadeh, F. Mokhtari, V. Jouyban-Gharamaleki, A. Mokhtarzadeh, and N. Shadjou, "Electrochemical monitoring of malondialdehyde biomarker in biological samples via electropolymerized amino acid/chitosan nanocomposite," J. Mol. Recognit., vol. 31, no. 8, p. e2717, 2018, doi: 10.1002/jmr.2717.
24. J. Wang, H. M. Schipper, A. M. Velly, S. Mohit, and M. Gornitsky, "Salivary biomarkers of oxidative stress: A critical review," Free Radic. Biol. Med., vol. 85, pp. 95–104, Aug. 2015, doi: 10.1016/j.freeradbiomed.2015.04.005.
25. H. A. Saputra, "Electrochemical sensors: basic principles, engineering, and state of the art," Monatshefte Für Chem. - Chem. Mon., vol. 154, no. 10, pp. 1083–1100, Oct. 2023, doi: 10.1007/s00706-023-03113-z.
26. D. Grieshaber, R. MacKenzie, J. Vörös, and E. Reimhult, "Electrochemical Biosensors - Sensor Principles and Architectures," Sensors, vol. 8, no. 3, Art. no. 3, Mar. 2008, doi: 10.3390/s80314000.
27. J. Baranwal, B. Barse, G. Gatto, G. Broncova, and A. Kumar, "Electrochemical Sensors and Their Applications: A Review," Chemosensors, vol. 10, no. 9, Art. no. 9, Sep. 2022, doi: 10.3390/chemosensors10090363.
28. A. M. Oliveira-Brett, J. A. P. Piedade, L. A. Silva, and V. C. Diculescu, "Voltammetric determination of all DNA nucleotides," Anal. Biochem., vol. 332, no. 2, pp. 321–329, Sep. 2004, doi: 10.1016/j.ab.2004.06.021.
29. R. N. Goyal and G. Dryhurst, "Redox chemistry of guanine and 8-oxyguanine and a comparison of the peroxidase-catalyzed and electrochemical oxidation of 8-oxyguanine," J. Electroanal. Chem. Interfacial Electrochem., vol. 135, no. 1, pp. 75–91, Apr. 1982, doi: 10.1016/0022-0728(82)90006-7.
30. T.-H. Li, W.-L. Jia, H.-S. Wang, and R.-M. Liu, "Electrochemical performance of 8-hydroxy-2′-deoxyguanosine and its detection at poly(3-methylthiophene) modified glassy carbon electrode," Biosens. Bioelectron., vol. 22, no. 7, pp. 1245–1250, Feb. 2007, doi: 10.1016/j.bios.2006.05.005.
31. X. Sun et al., "Electrochemical detection of 8-hydroxy-2′-deoxyguanosine as a biomarker for oxidative DNA damage in HEK293 cells exposed to 3-chloro-1,2-propanediol," Anal. Methods, vol. 7, no. 16, pp. 6664–6671, Aug. 2015, doi: 10.1039/C5AY01246E.
32. A. Mugweru, B. Wang, and J. Rusling, "Voltammetric Sensor for Oxidized DNA Using Ultrathin Films of Osmium and Ruthenium Metallopolymers," Anal. Chem., vol. 76, no. 18, pp. 5557–5563, Sep. 2004, doi: 10.1021/ac049375j.
33. N. Kumar, Rosy, and R. N. Goyal, "A melamine based molecularly imprinted sensor for the determination of 8-hydroxydeoxyguanosine in human urine," Talanta, vol. 166, pp. 215–222, May 2017, doi: 10.1016/j.talanta.2017.01.058.
34. G. V. Martins, A. C. Marques, E. Fortunato, and M. G. F. Sales, "8-hydroxy-2′-deoxyguanosine (8-OHdG) biomarker detection down to picoMolar level on a plastic antibody film," Biosens. Bioelectron., vol. 86, pp. 225–234, Dec. 2016, doi: 10.1016/j.bios.2016.06.052.
35. A. M. Faria, E. B. M. I. Peixoto, C. B. Adamo, A. Flacker, E. Longo, and T. Mazon, "Controlling parameters and characteristics of electrochemical biosensors for enhanced detection of 8-hydroxy-2′-deoxyguanosine," Sci. Rep., vol. 9, no. 1, p. 7411, May 2019, doi: 10.1038/s41598-019-43680-y.
36. L.-P. Jia et al., "Enzyme-free and triple-amplified electrochemical sensing of 8-hydroxy-2′-deoxyguanosine by three kinds of short pDNA-driven catalyzed hairpin assemblies followed by a hybridization chain reaction," Analyst, vol. 145, no. 10, pp. 3605–3611, May 2020, doi: 10.1039/D0AN00233J.
37. L. Yuan, Y. Lan, M. Han, J. Bao, W. Tu, and Z. Dai, "Label-free and facile electrochemical biosensing using carbon nanotubes for malondialdehyde detection," Analyst, vol. 138, no. 11, pp. 3131–3134, May 2013, doi: 10.1039/C3AN00041A
38. M. Jamshidi, A. Walcarius, M. Thangamuthu, M. Mehrgardi, and A. Ranjbar, "Electrochemical approaches based on micro- and nanomaterials for diagnosing oxidative stress," Microchim. Acta, vol. 190, no. 4, p. 117, Mar. 2023, doi: 10.1007/s00604-023-05681-7.
39. C. Amatore, S. Arbault, M. Guille, and F. Lemaître, "Electrochemical Monitoring of Single Cell Secretion: Vesicular Exocytosis and Oxidative Stress," Chem. Rev., vol. 108, no. 7, pp. 2585–2621, Jul. 2008, doi: 10.1021/cr068062g.

40. M. K. Beissenhirtz, F. W. Scheller, and F. Lisdat, “A Superoxide Sensor Based on a Multilayer Cytochrome c Electrode,” Anal. Chem., vol. 76, no. 16, pp. 4665–4671, Aug. 2004, doi: 10.1021/ac049738f.
41. Z. Wang, H. Zhao, Q. Gao, K. Chen, and M. Lan, “Facile synthesis of ultrathin two-dimensional graphene-like CeO2–TiO2 mesoporous nanosheet loaded with Ag nanoparticles for non-enzymatic electrochemical detection of superoxide anions in HepG2 cells,” Biosens. Bioelectron., vol. 184, p. 113236, Jul. 2021, doi: 10.1016/j.bios.2021.113236.
42. S. Zhao, Z. Shi, C. X. Guo, and C. M. Li, “A high-energy-state biomimetic enzyme of oxygen-deficient MnTiO3 nanodiscs for sensitive electrochemical sensing of the superoxide anion,” Chem. Commun., vol. 55, no. 54, pp. 7836–7839, Jul. 2019, doi: 10.1039/C9CC02679G.
43. E. Dumitrescu, K. N. Wallace, and S. Andreescu, “Real time electrochemical investigation of the release, distribution and modulation of nitric oxide in the intestine of individual zebrafish embryos,” Nitric Oxide, vol. 74, pp. 32–38, Apr. 2018, doi: 10.1016/j.niox.2018.01.002.
44. R. E. Özel, K. N. Wallace, and S. Andreescu, “Chitosan coated carbon fiber microelectrode for selective in vivo detection of neurotransmitters in live zebrafish embryos,” Anal. Chim. Acta, vol. 695, no. 1, pp. 89–95, Jun. 2011, doi: 10.1016/j.aca.2011.03.057.
45. G. Ferrer-Sueta and R. Radi, “Chemical Biology of Peroxynitrite: Kinetics, Diffusion, and Radicals,” ACS Chem. Biol., vol. 4, no. 3, pp. 161–177, Mar. 2009, doi: 10.1021/cb800279q.
46. M. Govindasamy, S. Manavalan, S.-M. Chen, R. Umamaheswari, and T.-W. Chen, “Determination of oxidative stress biomarker 3-nitro-l-tyrosine using CdWO4 nanodots decorated reduced graphene oxide,” Sens. Actuators B Chem., vol. 272, pp. 274–281, Nov. 2018, doi: 10.1016/j.snb.2018.05.138.
47. R. Jalili and M. Amjadi, “Bio-inspired molecularly imprinted polymer–green emitting carbon dot composite for selective and sensitive detection of 3-nitrotyrosine as a biomarker,” Sens. Actuators B Chem., vol. 255, pp. 1072–1078, Feb. 2018, doi: 10.1016/j.snb.2017.08.145.
48. G. V. Martins, A. C. Marques, E. Fortunato, and M. G. F. Sales, “Wax-printed paper-based device for direct electrochemical detection of 3-nitrotyrosine,” Electrochimica Acta, vol. 284, pp. 60–68, Sep. 2018, doi: 10.1016/j.electacta.2018.07.150.
49. S.-M. Chen et al., “Hierarchically structured CuFe2O4 ND@RGO composite for the detection of oxidative stress biomarker in biological fluids,” Inorg. Chem. Front., vol. 5, no. 4, pp. 944–950, Apr. 2018, doi: 10.1039/C7QI00799J.
50. S. Wang et al., “Constructing a novel composite of molecularly imprinted polymer-coated AuNPs electrochemical sensor for the determination of 3-nitrotyrosine,” Electrochimica Acta, vol. 259, pp. 893–902, Jan. 2018, doi: 10.1016/j.electacta.2017.11.033.
51. S. P. Ng, G. Qiu, N. Ding, X. Lu, and C.-M. L. Wu, “Label-free detection of 3-nitro-l-tyrosine with nickel-doped graphene localized surface plasmon resonance biosensor,” Biosens. Bioelectron., vol. 89, pp. 468–476, Mar. 2017, doi: 10.1016/j.bios.2016.04.017.
52. X. Wang, M. Zhu, H. Liu, J. Ma, and F. Li, “Modification of Pd–Fe nanoparticles for catalytic dechlorination of 2,4-dichlorophenol,” Sci. Total Environ., vol. 449, pp. 157–167, Apr. 2013, doi: 10.1016/j.scitotenv.2013.01.008.
53. Y. Bai and S. Li, “Oxidative Stress Sensing System for 8-OHdG Detection Based on Plasma Coupled Electrochemistry by Transparent ITO/AuNTAs/PtNPs Electrode,” Biosensors, vol. 13, no. 6, p. 643, Jun. 2023, doi: 10.3390/bios13060643.
54. L. Yang, B. Wang, H. Qi, Q. Gao, C. Li, and C. Zhang, “Highly Sensitive Electrochemical Sensor for the Determination of 8-Hydroxy-2′-deoxyguanosine Incorporating SWCNTs-Nafion Composite Film,” J. Sens., vol. 2015, no. 1, p. 504869, 2015, doi: 10.1155/2015/504869.
55. Rosy and R. N. Goyal, “Determination of 8-Hydroxydeoxyguanosine: A potential biomarker of oxidative stress, using carbon-allotropic nanomaterials modified glassy carbon sensor,” Talanta, vol. 161, pp. 735–742, Dec. 2016, doi: 10.1016/j.talanta.2016.09.038.
56. P. Montoro-Leal, M. Zougagh, A. Sánchez-Ruiz, Á. Ríos, and E. Vereda Alonso, “Magnetic graphene molecularly imprinted polypyrrole polymer (MGO@MIPy) for electrochemical sensing of malondialdehyde in serum samples,” Microchem. J., vol. 178, p. 107377, Jul. 2022, doi: 10.1016/j.microc.2022.107377.
57. B. Sriram, S. Kogularasu, S.-F. Wang, and G.-P. Chang-Chien, “The Fabrication of a La2Sn2O7/f-HNT Composite for Non-Enzymatic Electrochemical Detection of 3-Nitro-l-tyrosine in Biological Samples,” Biosensors, vol. 13, no. 7, Art. no. 7, Jul. 2023, doi: 10.3390/bios13070722.
58. B. Sriram, J. N. Baby, Y.-F. Hsu, S.-F. Wang, and M. George, “In Situ Synthesis of a Bismuth Vanadate/Molybdenum Disulfide Composite: An Electrochemical Tool for 3-Nitro-l-Tyrosine Analysis,” Inorg. Chem., vol. 61, no. 35, pp. 14046–14057, Sep. 2022, doi: 10.1021/acs.inorgchem.2c02037.
59. F. X. Hu et al., “Living Cells Directly Growing on a DNA/Mn3(PO4)2-Immobilized and Vertically Aligned CNT Array as a Free-Standing Hybrid Film for Highly Sensitive In Situ Detection of Released Superoxide Anions,” Adv. Funct. Mater., vol. 25, no. 37, pp. 5924–5932, 2015, doi: 10.1002/adfm.201502341.
60. Z. Zhai et al., “Robust nanozyme with dense crystalline-amorphous interfaces for efficient detection of reactive oxygen species in saliva,” Sens. Actuators B Chem., vol. 435, p. 137571, Jul. 2025, doi: 10.1016/j.snb.2025.137571.
61. U. Afzal et al., “Chemical engineering for advanced flexible sensors: Novel carbon-metal oxide nanocomposites with superior multi-sensing behavior,” Sens. Actuators B Chem., vol. 431, p. 137449, May 2025, doi: 10.1016/j.snb.2025.137449.
62. Z. Xu et al., “A wearable sensor based on multifunctional conductive hydrogel for simultaneous accurate pH and tyrosine monitoring in sweat,” Biosens. Bioelectron., vol. 234, p. 115360, Aug. 2023, doi: 10.1016/j.bios.2023.115360.
63. A. Khan, E. DeVoe, and S. Andreescu, “Carbon-based electrochemical biosensors as diagnostic platforms for connected decentralized healthcare,” May 2023, doi: 10.1039/D2SD00226D.
64. C. Mwanza, W.-Z. Zhang, K. Mulenga, and S.-N. Ding, “Advancing green chemistry in environmental monitoring: the role of electropolymerized molecularly imprinted polymer-based electrochemical sensors,” Green Chem., vol. 26, no. 23, pp. 11490–11517, Nov. 2024, doi: 10.1039/D4GC03250K.
65. J. Kim et al., “Wearable salivary uric acid mouthguard biosensor with integrated wireless electronics,” Biosens. Bioelectron., vol. 74, pp. 1061–1068, Dec. 2015, doi: 10.1016/j.bios.2015.07.039.
66. H. Duan et al., “Wearable Electrochemical Biosensors for Advanced Healthcare Monitoring,” Adv. Sci. Weinh. Baden-Wurtt. Ger., vol. 12, no. 2, p. e2411433, Jan. 2025, doi: 10.1002/advs.202411433.
67. R. Diab, A. Choufani, J. Dagher, and N. Chahine, “The Influence of Circadian Rhythm on the Antioxidant Capacity of Saliva in Periodontal Diseases,” Cureus, vol. 16, no. 3, p. e56174, Mar. 2024, doi: 10.7759/cureus.56174.
68. S. Watanabe, Y. Kawasaki, and K. Kawai, “Diurnal variation of salivary oxidative stress marker 8-hydroxyguanine,” Genes Environ., vol. 41, no. 1, p. 20, Dec. 2019, doi: 10.1186/s41021-019-0138-3.
69. J. F. Hernández-Rodríguez, D. Rojas, and A. Escarpa, “Electrochemical Sensing Directions for Next-Generation Healthcare: Trends, Challenges, and Frontiers,” Anal. Chem., vol. 93, no. 1, pp. 167–183, Jan. 2021, doi: 10.1021/acs.analchem.0c04378.
70. P. V. V. Romanholo, C. A. Razzino, P. A. Raymundo-Pereira, T. M. Prado, S. A. S. Machado, and L. F. Sgobbi, “Biomimetic electrochemical sensors: New horizons and challenges in biosensing applications,” Biosens. Bioelectron., vol. 185, p. 113242, Aug. 2021, doi: 10.1016/j.bios.2021.113242.

Journal of Engineering, Science and Technological Trends (JESTT)

Vol. 2, Issue 2, July 2025
DOI: https://doi.org/10.64060/jestt.v2i2.4

Review

Twisted Bilayer Graphene at the Magic Angle: A Review of Highly Correlated Physics and Unconventional Superconductivity

Adeena Fatima [1]* and Husnain Ahmed[2]

[1]School of Microelectronics, Tianjin University, Tianjin 300072, PR China
[2] Teesside University, Middlesbrough, United Kingdom
* Corresponding Email: fatimaadeena2@gmail.com (A. Fatima)

Received: 02 March 2025 / Revised: 27 May 2025 / Accepted: 20 June 2025 / Published online: 10 July 2025

ABSTRACT

A novel platform for researching topological quantum phenomena, unusual superconductivity, and strongly coupled electron physics is Twisted Bilayer Graphene (TBG) at the "Magic Angle" (~1.05°). Two graphene layers are rotated to this exact angle to form a moiré superlattice, which produces flat electronic bands that significantly improve electron-electron interactions. This results in a rich phase diagram with non-Fermi liquid behaviour, correlated insulators, and superconductivity. This review covers the theoretical foundations, experimental results, and unanswered concerns about magic-angle TBG, including significant challenges like twist angle control, disorder effects, and the interaction of strain and electrical characteristics. Beyond basic research, TBG has great technological potential, with potential applications in neuromorphic devices, ultra-sensitive sensors, and quantum computing (e.g., topological qubits). This system provides a novel approach to comprehending high-temperature superconductivity and achieving next-generation quantum technologies by fusing insights from correlated physics with device engineering.

Keywords*:* Twisted Bilayer Graphene; Magic Angle; Superconductivity; Correlated Insulators; Moire Superlattice

1. Introduction

Due to its remarkable electrical properties, graphene's discovery in 2004 transformed condensed matter physics; at present, the absence of a natural bandgap restricts its applications in semiconductor devices. This basic limitation led to novel approaches for modifying the electrical structure of graphene, which ultimately resulted in the revolutionary discovery of twisted bilayer graphene (TBG). A moiré superlattice that radically changes the electrical behaviour of the system is produced when two graphene layers are rotated to a precise "magic angle" of roughly 1.05°, according to research conducted in 2018 by MIT researchers under the direction of Pablo Jarillo-Herrero [1]. In order to overcome the limits of monolayer graphene, this twist engineering creates flat electronic bands where strong electron correlations result in remarkable phenomena such as correlated insulating states and superconductivity.

The magic-angle TBG is a unique platform for investigating strongly correlated physics, replicating essential characteristics of high-temperature superconductors without the need for chemical doping. Superconductivity, Mott-like insulators, and non-Fermi liquid behaviour are all included in the rich phase diagram made possible by the moiré-induced flat bands, which significantly improve electron-electron interactions and are adjustable by electrostatic gating [2]. In addition to having significant effects on basic physics, TBG's remarkable qualities have the potential to revolutionise quantum technology, such as topological quantum computers and extremely efficient electronic devices. Unprecedented insights into the interaction of band structure engineering, superconductivity, and correlation effects in two-dimensional materials are still being offered by this system.

The importance of magic-angle TBG's strength is its ability to replicate the physics of high-temperature superconductors while requiring no chemical doping and being solely controlled by electrostatic gating. The development of a moiré superlattice, which significantly changes the band structure and produces flat bands where electrons travel slowly and interact fiercely, controls the system's electrical characteristics. Superconductivity, Mott-like insulators, and odd metal behaviour are all encompassed in the rich

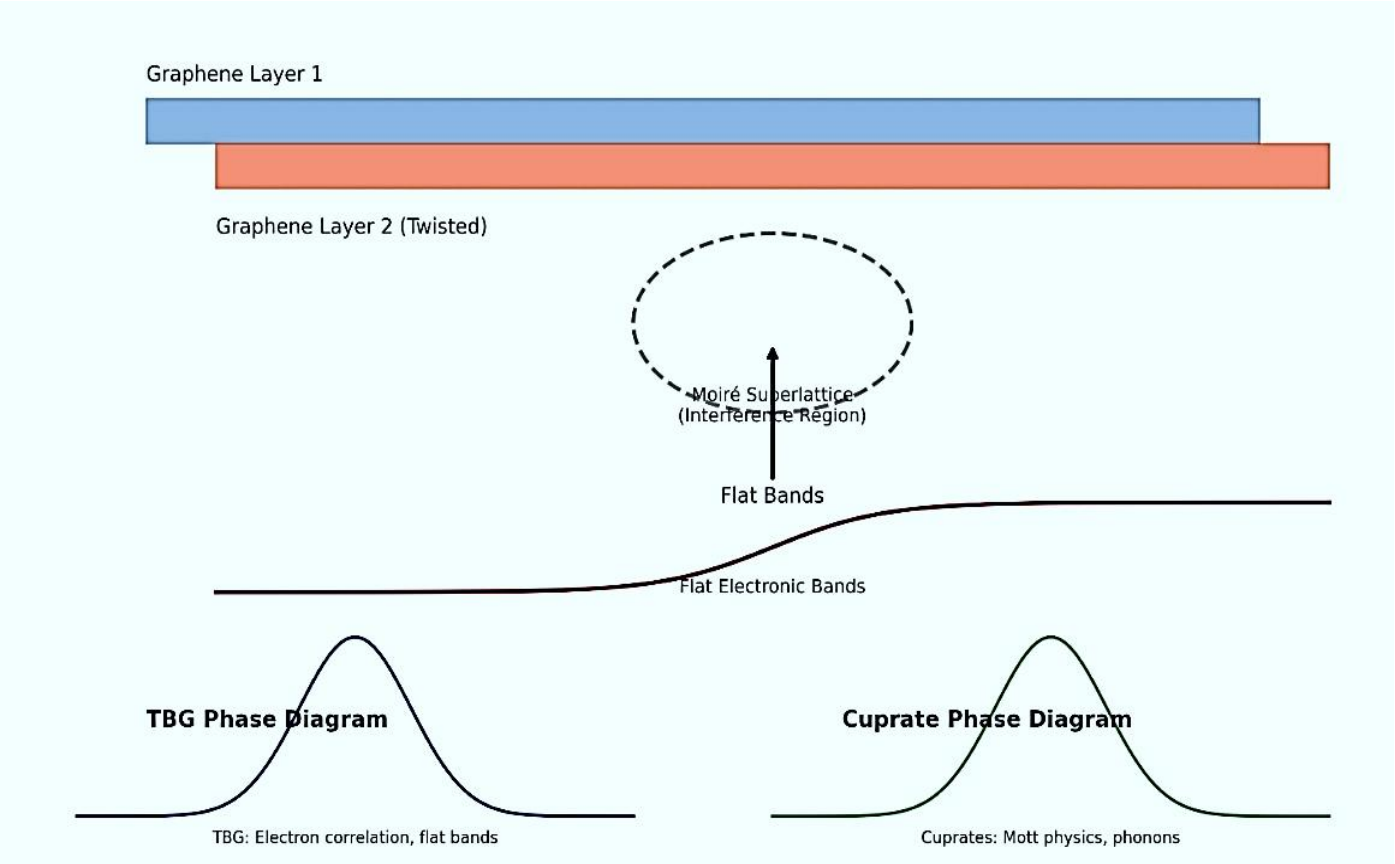

Figure 1: *Moiré Superlattice and Flat Band Formation* [5].

phase diagram that results from the enhancement of electron-electron correlations by these flat bands.

Beyond its basic scientific significance, TBG has potential applications in next-generation quantum technologies such as neuromorphic devices, topological quantum computing, and ultra-low-power electronics [2].

2. Theoretical Foundation

The creation of a moiré superlattice, which occurs when two graphene sheets are stacked with a slight rotational misalignment, is fundamental to the electrical behaviour of twisted bilayer graphene. The basic Dirac cone structure of graphene is altered by this moiré pattern's introduction of a long-range periodic potential, which causes flat bands to appear at specific "magic" twist angles. The first theoretical foundation for comprehending these effects was offered by the 2011 Bistritzer-MacDonald model, which predicted that the electrons' Fermi velocity would disappear and almost dispersionless bands would form at a twist angle of about 1.05° [3]. Because they enhance electron-electron interactions and allow for the formation of tightly correlated phases, these flat bands are essential [4].

When two graphene sheets are rotated relative to one another at a tiny twist angle, a moiré superlattice is formed in twisted bilayer graphene (TBG), as shown in Figure 1. The electronic band structure is considerably modified by the superlattice periodicity that results from the ensuing moiré interference pattern. The system displays flat electronic bands within the described "magic angle" (~1.1°), where kinetic energy is suppressed and electron-electron correlations are strengthened.

A comparison of the superconducting phase diagrams of cuprate high-temperature superconductors and TBG, as discussed in Table 1. As a function of carrier concentration, both show a distinctive dome-shaped superconducting phase, indicating the existence of strong correlation physics [5].

2.1. Schematic Diagram

The system behaves like other correlated materials, including heavy fermion compounds and high-temperature cuprate superconductors, in this domain. For example, the system becomes a correlated insulator, similar to a Mott insulator, at half-filling, when the number of electrons in the moiré unit cell equals the number of possible states. The strong Coulomb repulsion between electrons, which stops them from flowing freely, is what causes this insulating state. Superconductivity emerges when the system is slightly doped away from half-filling, indicating a delicate balance between coherence and localisation. With continuous discussions over the exact mechanisms underlying superconductivity in TBG, the interaction between these phases has emerged as a central area of theoretical investigation. While some theories propose solely electrical causes, others relate it to phonon-mediated pairing, such as excitonic effects [6].

3. Experimental Breakthrough

By observing a superconducting transition at temperatures below 1.7 Kelvin, the Jarillo-Herrero group reported the experimental discovery of superconductivity in magic-angle TBG in 2018, as demonstrated in Table 1. Because it showed that superconductivity might develop in a system devoid of the strong electron-phonon interaction commonly associated with normal superconductors, this discovery was very remarkable. Rather, the hallmark of unconventional superconductivity, strong electron correlations, seems to be the driving force behind the superconductivity in TBG. Its potential as a flexible platform for researching quantum phase transitions was further demonstrated by the capacity to shift the system be-

Table 1:
Moiré Superlattice and Flat Band Formation [5].

Year	Milestone/Event	Twist Angle (°)	Critical Temperature (Tc)	Doping Level / Filling Factor	Key Observation
2018	Discovery of superconductivity in magic-angle TBG	~1.1° (magic angle)	~1.7 K	±2 electrons per moiré unit cell	Superconductivity adjacent to a correlated insulating state
2018	Observation of a correlated insulating state	~1.1°	N/A	Half-filling (±2)	Mott-like insulating behavior
2019	Enhancement of Tc via pressure tuning	~1.1°	Up to 3.5 K	±2	Tc increased under hydrostatic pressure
2020	Nematic order and symmetry breaking observed	~1.1°	~1.5 K	Near half-filling	Broken rotational symmetry detected
2021	Identification of "strange metal" or "odd metal" behavior	~1.1°	—	Near charge neutrality to ±2	Linear-in-T resistivity over a wide temperature range
2022	Tunable moiré heterostructures (twist angle/strain control)	Various	~1–5 K	Broad range	Broader tunability of correlated phases
2023	Superconductivity in twisted trilayer graphene (TTG)	~1.5° TTG	~3 K	Similar fillings	Shows superconductivity beyond bilayer systems

tween insulating and superconducting states using an external electric field [6].

Even more complex physics has been discovered in TBG through subsequent research, such as odd metal behaviour with linear-in-temperature resistivity, a hint of non-Fermi liquid physics. This behaviour, in which the system hovers close to a phase transition at absolute zero temperature, is frequently linked to quantum criticality. Comparison between conventional and odd metals has been described (in Table 2) to showcase the need to explain both of them. Recent developments have broadened the focus of TBG studies to encompass twisted multilayer structures with novel associated phases and increased superconducting transition temperatures, including trilayer graphene [7].

The phase diagram of TBG has also been further enhanced by the discovery of topological states, such as quantum Hall effects, by the use of magnetic fields. These findings have solidified TBG as a model system for investigating the relationship among superconductivity, topology, and correlation [8].

3.1. Summary of Differences

Twisted bilayer graphene (TBG) exhibited linear-in-T resistivity over a broad temperature range close to specific doping levels in the 2018–2021 studies, lacking a discernible superconducting dome, depicted in Figure 2. This is an excellent option for investigating non-Fermi liquid physics since it is anomalous and represents a breakdown of quasiparticle-based transport [9].

Table 2:
Summary of Differences Between Conventional and Odd Metals [9].

Feature	Fermi Liquid	Odd/Strange Metal
Resistivity vs Temperature	$\rho(T)\sim T^2$	$\rho(T)\sim T$
Dominant scattering	Electron-electron	Unknown, likely critical or collective
Quasiparticles	Long-lived	Not well-defined
Underlying theory	Landau-Fermi liquid theory	No complete theory yet
Typical materials	Simple metals	Cuprates, TBG, heavy fermions

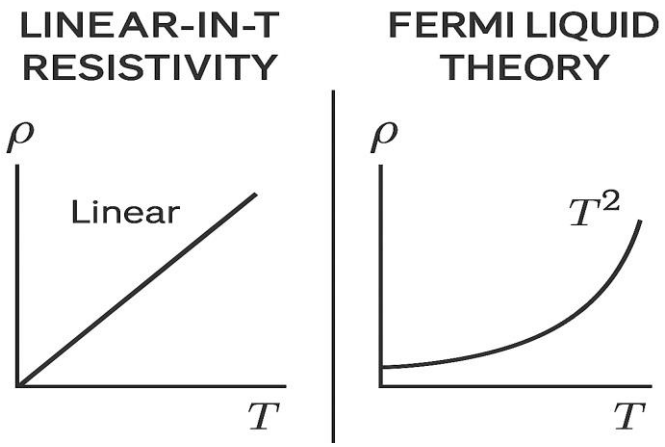

Figure 2: *The Graphical Demonstration between Fermi Liquid and Linear-IN-T-Resistivity [10].*

4. Mechanism of Superconductivity

There is still much disagreement on the genesis of Superconductivity in magic-angle TBG. The superconductivity of TBG may result from solely electronic causes, in contrast to ordinary superconductors, where pairing is mediated by lattice vibrations (phonons). One theory is that spin fluctuations serve as the glue that holds electrons together in Cooper pairs because they are fueled by strong electron correlations. In this case, TBG would be categorised with high-temperature cuprate superconductors, where spin fluctuations are believed to be important. Excitonic pairing, in which electron-hole interactions stabilise the superconducting state, is the subject of another proposal [11].

4.1. Introduction to Valley Degrees of Freedom

- The valley index is an additional quantum number that electrons in materials like graphene possess.
- The Brillouin zone of graphene has two inequivalent Dirac cones at locations designated K and K′.
- These provide an additional degree of freedom, much like spin, and function similarly to pseudospins or valleys.

- Thus, an electron's characteristics include its valley (K or K′) as well as its momentum and spin.

4.2. Intervalley Coherence

A quantum superposition between states in the K and K′ valleys is known as Intervalley Coherence (IVC), as described by the equation (1) below:

$$|\Psi\rangle = \alpha\,|K\rangle + \beta\,|K'\rangle \qquad (1)$$

New coherent states can be created when electrons interact or pair across troughs. This is comparable to spin-singlet creation or exciton condensation, but it occurs between valleys. It can result in time-reversal symmetry breakage, nematicity, or new superconducting order parameters [10].

The moiré superlattice itself may be essential for promoting superconductivity. Pairing instabilities are more likely when the moiré lattice increases the density of states close to the Fermi level by generating a periodic potential with a large unit cell. Additionally, the superlattice can encourage intervalley coherence, which produces exotic superconducting order parameters by pairing electrons from various momentum-space valleys. Recent studies have pointed to spin-triplet pairing, which would distinguish TBG from conventional s-wave superconductors and align it with other unconventional systems like strontium ruthenate [11]. Higher-quality samples with less disorder, theoretical modelling, and sophisticated spectroscopic techniques will all be needed to answer these problems [11].

4.3. Summary

Electrons exist in valley states (K, K′) in addition to spin states in systems such as twisted bilayer graphene. Exotic superconducting states can result from superpositions formed by these valleys. In contrast to what occurs in typical (phonon-driven) superconductors, this opens the door to unusual pairing mechanisms, some of which display topological features or break symmetries [12].

5. Critical Perspectives in Twisted Bilayer Graphene Research

Recent developments in the study of twisted bilayer graphene (TBG) have uncovered a number of surprising occurrences that challenge generally held assumptions and pave the way for further investigation. Scientists have found additional magic angles at 0.5° and 1.8° that show separate superconducting and associated insulating states, in addition to the well-studied first magic angle of roughly 1.1°.

5.1. Introduction to Higher Magic Angles

Superconductivity in TBG is not restricted to the original "magic angle" (~1.05°), as shown in Figure 3, according to recent research. At 0.5° and 1.8°, further magic angles show:

- Differential superconducting domes at varying doping concentrations
- SC re-emerging after suppression in re-entrant superconductivity
- Comparable to cuprate phase diagrams are competing charge orders [13].

5.2. Phase Diagram of Multi-Dome Superconductivity

The phase diagrams of these higher-order angles show (in Figure 3) re-entrant superconductivity with many superconducting domes, indicating a more intricate quantum phase environment than was previously thought. The finding of conflicting charge orders that seem to be entangled with superconductivity and show remarkable similarities to the phase diagrams of high-temperature cuprate superconductors is very noteworthy. However, there is currently a substantial knowledge gap in the field, as there is no complete theoretical framework to explain why some higher-order angles exhibit improved superconducting transition temperatures while others do not [14].

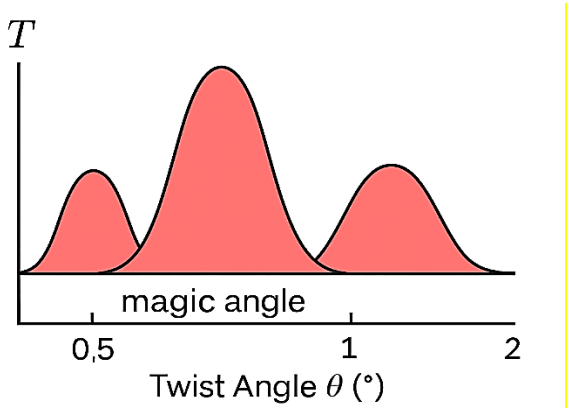

Figure 3: *Phase Diagram Illustration of Multi-Dome Superconductivity [13].*

5.3. Experimental Validation of Photo-Induced Superconductivity

Photo-Induced Superconductivity: Experiments demonstrate that ultrafast laser pulses, with durations on the order of ~100 femtoseconds, can profoundly modify the electronic properties of TBG. These pulses have been shown to temporarily increase the superconducting critical temperature (Tc) by as much as 50%, enabling transient access to enhanced superconducting phases not achievable under equilibrium conditions. Additionally, the intense photoexcitation can melt charge orders that otherwise compete with superconductivity, thereby unmasking the underlying superconducting state. Beyond these effects, ultrafast excitation generates highly non-thermal distributions of electrons, driving the system into nonequilibrium regimes where novel electronic behaviours and transient phases may emerge.

- ***Proposed Mechanisms***: Experiments have further shown that photons can stimulate electrons to form ideal pairing states, leading to a selective population of specific electronic bands that favour superconductivity. In addition, the excitation of coherent phonons enhances electron-phonon coupling through dynamic lattice modulation, which can further stabilise superconducting and other correlated phases.

- ***Engineering Floquets***: Experiments and theoretical studies have also demonstrated that time-periodic drives can create virtual flat bands, which effectively reshape the electronic structure and enhance correlation effects beyond what is possible in static conditions [15].

5.4. Equilibrium and Non-Equilibrium Approach

Recent developments in spin-orbit engineering have given TBG research fascinating new avenues for investigation. Scientists have successfully produced artificial Rashba effects that produce spin-split bands by intercalating heavy atoms like tungsten between graphene layers. The possibility of achieving topological superconductivity in TBG systems has increased as a result of this research. Results from hybrid structures that combine TBG with transition-metal dichalcogenides have been especially encouraging, exhibiting improved spin-valley locking effects. These developments do, however, provide a unique set of difficulties since the spin-orbit coupling that is introduced frequently clashes with the correlation

effects that are already there, leading to phase diagrams that are more complicated and challenging to understand. Because of its intricacy, more advanced theoretical instruments are required to handle the interactions between these different quantum processes [16].

The theoretical basis of implementing these approaches involves carefully tuning the drive parameters, such as using frequencies in the terahertz range (1–10 meV) and employing circularly polarised light to break time-reversal symmetry, while maintaining intensities below the damage threshold for graphene (approximately 1 MW/cm²). Expected outcomes include the emergence of artificial flat bands even at non-magic twist angles, the opening of topological gaps in the electronic spectrum, and an enhancement of spin-orbit interactions. However, integrating these techniques into functional devices presents several challenges, including the design of photonic cavities capable of providing continuous illumination, efficient dissipation of heat within confined structures, and achieving precise state selectivity through tailored pulse shaping.

Through periodic driving, Floquet engineering enables non-equilibrium tuning of quantum systems, as explained in Table 3. This method could:

- Generate superconducting phases driven by light
- Improve existing pairing mechanisms or perhaps make them available.
- Enable future quantum devices to have switchable, controllable quantum states [17].

The study of non-equilibrium events in TBG has produced unexpected findings that may have technological ramifications [18]. Photo-induced superconductivity, in which precisely calibrated laser pulses can momentarily increase superconducting transition temperatures by as much as 50%, has been established using ultrafast spectroscopic tests. The use of Floquet engineering, in which time-periodic drives might theoretically produce artificial flat bands even at non-magic angles, is another exciting avenue. These effects serve as a crucial proof of concept for non-equilibrium control of quantum materials, even though they only last for picosecond durations at the moment. These results imply that additional routes to reaching and stabilising desired quantum states that are unavailable through static techniques may be provided by dynamic manipulation of TBG systems.

Long-held beliefs regarding the dominating physics in TBG systems are being called into question by an increasing amount of high-resolution scanning tunnelling microscopy data. According to new data, strain solitons that drastically alter the electrical band structure are produced when graphene layers are reconstructed at the atomic scale at modest twist angles. Unexpected quantum phases seem to be hosted by inevitable local angle fluctuations on the order of 0.05°, even in meticulously manufactured "perfect" systems [18]. These findings have raised important questions concerning whether atomic-scale features are more important than previously thought or whether moiré effects alone can account for TBG's complex phenomenology. The conventional moiré band models that have influenced a large portion of the field's theoretical work up to this point may need to be modified in light of this new viewpoint [19].

Although there is still much excitement surrounding the possible uses of TBG in quantum technologies, a more sophisticated comprehension of real-world limitations is starting to take shape. There are still several obstacles in the way of creating practical devices, especially when it comes to qubit coherence times, which are now restricted to nanoseconds due to charge noise. Another significant challenge with TBG-based systems is their scalability, since no method now in use can consistently align hundreds of moiré devices on a single chip with the necessary sub-0.01° precision. These drawbacks imply that hybrid strategies that integrate TBG with more established silicon-based platforms would be necessary for near-term commercial applications. As the discipline develops, this reality check emphasises how crucial it is to strike a balance between basic research and real-world engineering requirements.

5.5. Summary

According to the current status of TBG research, three paradigm shifts are required in order to influence the future direction of the discipline. First, disorder must be viewed as a potential design characteristic that can be tailored to stabilise desired quantum states, rather than as an inevitable annoyance. Second, dynamic control strategies that take advantage of non-equilibrium phenomena should be included in the emphasis on static systems. Third, more integrated methods that integrate TBG with other functional elements in photonic, spin, and three-dimensional architectures must replace the isolation of TBG systems in research settings.

The importance of mechanical characteristics and strain solitons in quantum transport, the thermodynamic features of TBG that seem to defy traditional constraints, and the creation of standardised metrology for twist angle calibration are some important areas that are still poorly understood. As the subject develops, scientists must balance the exquisite simplicity of moiré physics with the growing understanding that the secrets of TBG may lie in atomic-scale intricacies [20].

Table 3:
Comparison of Equilibrium Vs. Non-Equilibrium Approaches [21]

Feature	Static TBG	Floquet-Engineered TBG
Band structure	Fixed by θ	Dynamically tunable
Tc limit	~3 K	Potentially higher
Stability	Permanent	Requires continuous drive
Topology	Intrinsic	On-demand

6. Challenges and Solutions

Even while our understanding of Twisted Bilayer Graphene (TBG) has advanced significantly, there are still a number of important issues. These challenges fall into three primary categories:

6.1. Fabrication Challenges

The twist angle between layers has a remarkable impact on TBG's electrical characteristics. Reproducible device fabrication is a significant challenge since even small deviations (~0.1°) from the magic angle (~1.05°) can significantly change the behaviour of the system. At scale, existing methods like the "tear-and-stack" method are unable to provide the necessary precision. Furthermore, after production, external variables like substrate interactions and temperature fluctuations may cause unforeseen changes. Although they have not yet completely solved these obstacles, emerging techniques like as strain engineering and alignment, helped by scanning probes, show promise.

6.2. Theoretical Uncertainties

There is still much discussion about the microscopic processes underlying TBG's unusual phases, as shown in Table 4. The superconducting order parameter remains contentious, with conflicting evidence suggesting s-wave, d-wave, or even p-wave pairing symmetry [21]. Similarly, the extent to which superconductivity and correlated insulating states are driven by electron-phonon coupling, spin fluctuations, and Coulomb repulsion remains unclear. The

Table 4:
Moiré Superlattice and Flat Band Formation [5].

Pairing Symmetry	Gap Structure	Time-Reversal Symmetry	Orbital Angular Momentum	Candidate Mechanism	Observed In
s-wave	Isotropic	Preserved	0	Phonon-mediated	Conventional superconductors (e.g., Nb)
d-wave	Nodes	Preserved	2	Spin fluctuations	High-Tc cuprates
p-wave	Chiral or helical	Broken or preserved	1	Triplet pairing, spin-orbit	Sr_2RuO_4 (possible), topological SCs
s± (sign-changing s-wave)	Isotropic but sign-changing	Preserved	0	Interband scattering (e.g., spin fluctuations)	Fe-based superconductors
Intervalley s-wave	Isotropic or anisotropic	Preserved or broken	0	Intervalley phonons or Coulomb	Twisted bilayer graphene (TBG)
Chiral d+id / p+ip	Gapped, complex	Broken	±2 / ±1	Intervalley coherence, topology	TBG, Moiré materials (proposed)

linear-in-temperature resistivity observed in the strange metal phase further hints at an underlying quantum critical point, although its origin is still unknown. Overall, the inherent complexity of strongly coupled moiré systems makes them exceptionally challenging to model, necessitating sophisticated computational and analytical approaches that contribute to this persistent uncertainty [21].

6.3. Material Imperfections

Intrinsic and extrinsic disorders significantly affect real-world TBG devices. Strain inhomogeneity, arising from local lattice deformations, induces electronic inhomogeneity by disrupting the moiré potential. Impurities and defects, including adsorbates, vacancies, and ripples, act as scattering centres that obscure the underlying physics. The substrate also plays a crucial role, as dielectric screening from surrounding materials such as hBN unpredictably alters the strength of interactions. Even “high-quality” devices exhibit nanoscale variations in twist angle and strain, as revealed by recent scanning tunnelling microscopy studies, complicating the interpretation of bulk measurements. Regarding superconductivity and topology, the superconducting phase of TBG may be stabilised through topological effects. Majorana zero modes (MZMs), which are robust non-Abelian quasiparticles appearing at edges or vortices in topological superconductors, have been theoretically predicted to emerge in TBG due to proximity-induced spin-orbit coupling, offering a potential pathway to fault-tolerant quantum computing [21]. In addition, helical edge states, akin to those in quantum spin Hall insulators, could enhance Cooper pair coherence and suppress dissipation, while topological protection from edge states may localise detrimental scattering processes and help preserve the superconducting phase. These theories are supported by experimental observations such as quantised conductance in magnetic fields and anomalous edge currents, though direct evidence of topological superconductivity, for example, via Josephson interferometry, remains elusive [22].

6.4. Solutions and Insights

To overcome all of these challenges, advances in fabrication techniques are essential, including improved strain management and atomic-precision alignment, along with the development of non-perturbative theoretical tools capable of addressing the strong correlations inherent in TBG. Additionally, phase-sensitive probes will be crucial for distinguishing between topological signatures and the symmetries of the superconducting order parameter. By addressing these obstacles, TBG research holds the promise of achieving unprecedented control over correlated quantum matter, thereby bridging the gap between fundamental studies and practical applications [23].

7. Application and Future Perspectives

Twisted Bilayer Graphene (TBG) at the magic angle has transformative promise in both basic research and quantum technologies, owing to its unique features as an incredibly tunable substrate for correlated physics.

7.1. Quantum Technologies

Fault-tolerant qubits based on Majorana zero modes, exotic quasiparticles that arise at the borders of topological superconductors and are naturally shielded from local noise, may be made possible by TBG's topological superconductivity. They're perfect for quantum computing because of this. Furthermore, TBG's electrostatically adjustable insulator-superconductor transitions resemble neural plasticity, indicating potential uses in neuromorphic computing with extremely low power requirements. TBG is a promising material for quantum sensors, such as single-electron transistors and nanoscale magnetometers, due to its extraordinary sensitivity to external fields [23].

7.2. Unresolved Challenges

Despite quick advancements, major challenges still exist:

- **Material control:** The ability to fabricate devices with exact twist angles and negligible disorder in an accurate way.
- **Mechanistic comprehension:** Demonstrating the characteristics of superconductivity (such as s-wave versus d-wave pairing) and how topology interacts with it.
- **Scalability:** For real-world applications, combining device-level capabilities with atomic-scale phenomena.

7.3. Moving Beyond Room-Temperature Superconductivity

A route to higher transition temperatures (Tc) is suggested by the identification of strain-tunable phases and larger magic angles (e.g., 0.5°, 1.8°). According to theoretical proposals, distinctive

pairing may be stabilised by heterostructures that combine TBG with effective spin-orbit materials. It may be possible to artificially produce and maintain high-Tc states using non-equilibrium techniques, e.g., Floquet engineering.

Beyond superconductivity, TBG offers a variety of experimental opportunities for exceptional quantum phases, such as quantum spin liquids and Wigner crystals, which have the potential to revolutionise our knowledge of strongly correlated matter [24].

From a practical standpoint, the technological promise of TBG-based materials is immense. Their compatibility with existing 2D heterostructure platforms and the potential to switch superconductivity dynamically using light or gating hold implications for quantum computing, reconfigurable electronics, and energy-efficient switching devices.

7.4. Future Perspectives

Future research must bridge atomic-scale insights with device-scale engineering, uniting fundamental discoveries in moiré quantum matter with scalable, robust technologies for the next generation of quantum materials [8],[9],[10],[11].

8. Conclusion

One of the most intriguing platforms in contemporary condensed matter physics is magic-angle twisted bilayer graphene, which provides previously unheard-of insights into strongly coupled electron systems and unusual superconductivity. In addition to offering a highly adjustable experimental system for verifying theoretical predictions, its discovery has helped to bridge the gap between other domains, including topological quantum matter and high-temperature superconductivity. Even if disorder and sample variability present difficulties, continuous improvements in manufacturing methods and theoretical knowledge keep expanding the realm of what TBG may achieve.

The possible uses of TBG, ranging from energy-efficient electronics to quantum computing, are becoming more apparent as research advances. In order to unlock additional functions, future research will probably concentrate on improving control over twist angles, investigating multilayer systems, and combining TBG with other quantum materials.

TBG has already had a significant impact on our knowledge of quantum materials, solidifying its position as a pillar of 21st-century physics regardless of whether it eventually results in useful room-temperature superconductors.

Declaration

Competing Interests: The authors declare that they have no known competing financial interests or personal relationships that could have appeared to influence the work reported in this paper.

Ethical Issues: There are no ethical issues. All data in this paper is publicly available.

Author Contribution Statement: A.F. and H.A. conceived the idea and designed the research; analysed and interpreted the data and wrote the paper.

Funding Statement: This research did not receive any specific grant from funding agencies in the public, commercial, or not-for-profit sectors.

Consent to Publish: All authors have agreed to publish the version of the manuscript in this journal.

References

1. Cao, Y., Fatemi, V., Fang, S., Watanabe, K., Taniguchi, T., Kaxiras, E., & Jarillo-Herrero, P. (2018). Unconventional superconductivity in magic-angle graphene superlattices. *Nature*, *556*(7699), 43-50.
2. Lu, X., Stepanov, P., Yang, W., Xie, M., Aamir, M. A., Das, I., ... & Efetov, D. K. (2019). Superconductors, orbital magnets and correlated states in magic-angle bilayer graphene. *Nature*, *574*(7780), 653-657.
3. Codecido, E., Wang, Q., Koester, R., Che, S., Tian, H., Lv, R., ... & Lau, C. N. (2019). Correlated insulating and superconducting states in twisted bilayer graphene below the magic angle. *Science Advances*, *5*(9), eaaw9770.
4. Rai, G., Crippa, L., Călugăru, D., Hu, H., Paoletti, F., de'Medici, L., ... & Wehling, T. (2024). Dynamical correlations and order in magic-angle twisted bilayer graphene. *Physical Review X*, *14*(3), 031045.
5. Tao, Z., Zhao, W., Shen, B., Li, T., Knüppel, P., Watanabe, K., ... & Mak, K. F. (2024). Observation of spin polarons in a frustrated moiré Hubbard system. *Nature Physics*, *20*(5), 783-787.
6. Dutta, R., Ghosh, A., Mandal, S., Watanabe, K., Taniguchi, T., Krishnamurthy, H. R., ... & Das, A. (2025). Electric Field-Tunable Superconductivity with Competing Orders in Twisted Bilayer Graphene near the Magic Angle. *ACS nano*, *19*(5), 5353-5362.
7. Díez-Mérida, J., Das, I., Di Battista, G., Díez-Carlón, A., Lee, M., Zeng, L., ... & Efetov, D. K. (2025). High-yield fabrication of bubble-free magic-angle twisted bilayer graphene devices with high twist-angle homogeneity. *Newton*, *1*(1).
8. Choi, Y., Kim, H., Peng, Y., Thomson, A., Lewandowski, C., Polski, R., ... & Nadj-Perge, S. (2021). Correlation-driven topological phases in magic-angle twisted bilayer graphene. *Nature*, 589(7843), 536-541.
9. Andrei, E. Y., & MacDonald, A. H. (2020). Graphene bilayers with a twist. *Nature materials*, *19*(12), 1265-1275.
10. Douçot, B., Mukhopadhyay, A., Policastro, G., & Samanta, S. (2021). Linear-in-T resistivity from semiholographic non-Fermi liquid models. *Physical Review D*, *104*(8), L081901
11. Wang, Y. J., Zhou, G. D., Peng, S. Y., Lian, B., & Song, Z. D. (2024). Molecular pairing in twisted bilayer graphene superconductivity. *Physical Review Letters*, *133*(14), 146001.
12. Arp, T., Sheekey, O., Zhou, H., Tschirhart, C. L., Patterson, C. L., Yoo, H. M., ... & Young, A. F. (2024). Intervalley coherence and intrinsic spin–orbit coupling in rhombohedral trilayer graphene. *Nature Physics*, *20*(9), 1413-1420
13. Fischer, A., Goodwin, Z. A., Mostofi, A. A., Lischner, J., Kennes, D. M., & Klebl, L. (2022). Unconventional superconductivity in magic-angle twisted trilayer graphene. *npj Quantum Materials*, 7(1), 5.
14. Tanaka, Y., Tamura, S., & Cayao, J. (2024). Theory of Majorana zero modes in unconventional superconductors. *Progress of Theoretical and Experimental Physics*, *2024*(8), 08C105.
15. Braz, L. B., Martins, G. B., & Dias da Silva, L. G. (2024). Superconductivity from spin fluctuations and long-range interactions in magic-angle twisted bilayer graphene. *Physical Review B*, *109*(18), 184502.
16. Wang, W. X., Liu, Y. W., & He, L. (2025). Quantum anomalous Hall effect in twisted bilayer graphene. *Chinese Physics B*.
17. Wang, W. X., Liu, Y. W., & He, L. (2025). Quantum anomalous Hall effect in twisted bilayer graphene. *Chinese Physics B*.
18. Maeda, K., Fukaya, Y., Yada, K., Lu, B., Tanaka, Y., & Cayao, J. (2025). Classification of pair symmetries in superconductors with unconventional magnetism. *Physical Review B*, *111*(14), 144508.
19. Oh, M., Nuckolls, K. P., Wong, D., Lee, R. L., Liu, X., Watanabe, K., ... & Yazdani, A. (2021). Evidence for unconventional superconductivity in twisted bilayer graphene. *Nature*, 600(7888), 240-245.
20. Else, D. V. (2024). Holographic models of non-Fermi liquid metals revisited: An effective field theory approach. *Physical Review B*, *109*(3), 035163.
21. Nguyen, D. H., Sidorenko, A., Taupin, M., Knebel, G., Lapertot, G., Schuberth, E., & Paschen, S. (2021). Superconductivity in an extreme strange metal. *Nature Communications*, *12*(1), 4341.
22. Heier, G., Park, K., & Savrasov, S. Y. (2024). Competing dxy and s±pairing symmetries in superconducting $La_3Ni_2O_7$: LDA+ FLEX calculations. *Physical Review B*, *109*(10), 104508.
23. Klimin, S. N., Tempere, J., Devreese, J. T., & der Marel, D. V. (2017). Multiband superconductivity due to the electron–LO–phonon interaction in strontium titanate and on a $SrTiO_3/LaAlO_3$ interface. *Journal of Superconductivity and Novel Magnetism*, *30*, 757-761.
24. Giannetti, C., Capone, M., Fausti, D., Fabrizio, M., Parmigiani, F., & Mihailovic, D. (2016). Ultrafast optical spectroscopy of strongly correlated materials and high-temperature superconductors: a non-equilibrium approach. *Advances in Physics*, *65*(2), 58-238.

Journal of Engineering, Science and Technological Trends (JESTT)

Vol. 2, Issue 2, July 2025
DOI: https://doi.org/10.64060/jestt.v2i2.5

Article

First-Principles Study of Cubic $CsSrF_3$: Effects of Li Doping on Structural, Electronic and Optical Properties

Fozia Hafeez[1]* and Adeena Fatima[2]

[1]Department of Applied Science, Glasgow Caledonian University, Glasgow, Scotland, United Kingdom
[2]School of Microelectronics, Tianjin University, Tianjin 300072, PR China
* Corresponding Email: foziahafeez041@gmail.com (F. Hafeez)

Received: 17 March 2025 / Revised: 31 May 2025 / Accepted: 30 June 2025 / Published online: 10 July 2025

ABSTRACT

In this work, the structural, electronic, optical, and elastic properties of cubic fluoro-perovskite $CsSrF_3$ and its lithium-doped derivatives ($Cs_{1-x}Li_xSrF_3$, x = 0–1) are systematically investigated using first-principles density functional theory (DFT) calculations utilizing the generalized gradient approximation using the Perdew–Burke–Ernzerhof (GGA-PBE) functional. To evaluate the structural stability, the total energy is fitted to the Birch–Murnaghan equation of state, resulting in equilibrium lattice constants of 5.000 Å for Pristine $CsSrF_3$ and 5.076 Å for the doped composition (x = 1). The electronic band structure study shows that Pristine $CsSrF_3$ has an indirect bandgap of 5.543 eV, which gradually narrows to 4.011 eV with full lithium substitution. Li-induced changes in electronic states close to the Fermi level are responsible for this trend. The valence and conduction bands are primarily controlled by the F-p and Sr-s orbitals, respectively, according to Density of States (DOS) studies. Optical properties demonstrate higher tunability with the doping of lithium, the refractive index varies between 1.78 and 1.40 eV, and the reflectivity decreases from 0.27 eV to 0.10 eV. These characteristics indicate considerable amounts of potential for photovoltaic and UV applications. Mechanical investigation shows anisotropic and ductile behaviour, with predicted bulk modulus values ranging from −9.890 GPa (Pristine) to −17.311 GPa (x = 1), demonstrating a softening effect with increased Li concentration. Ultimately, the findings highlight the potential of Pristine $CsSrF_3$ and its Li-doped concentrations for the implementation into energy-harvesting and next-generation optoelectronic systems.

Keywords: Bandgap Engineering; CASTEP; DFT; Elastic Properties; First principle; Fluoro-Perovskite; Li-doped

1. Introduction

During the recent decade, perovskites have received substantial attention in the field of optoelectronics and, more recently, in solar cells and energy storage devices as the most promising and expensive low-cost energy materials available today [1],[2]. The structure of perovskite with such a chemical formula, Calcium titanium oxide, has have chemical formula (ABX_3), which shows an anion (X) that initiates bonds with both A and B cations (different sizes). F, Cl, Br, and I are examples of an anion (X) that can be an oxide or halide [3]. The comparatively simple crystal structure of fluoro-perovskites (ABF_3) exhibits a wide range of electric, magnetic, piezoelectric, optical, thermodynamic, and mechanical properties, which is the driving motivation behind this tremendous interest in these crystals [4].

Scientists are interested in complex alkali metal fluorides because they can be used as fluorinating agents and catalysts for a wide variety of organo-fluorochemical processes [5]. There are numerous electrical and optical applications where fluoride-type perovskite is being used, particularly solid-state lithium-ion batteries and high-temperature superconductivity [6], Piezoelectricity and ultraviolet optical absorption [7]. These materials are being studied because of their magnetic, electrical, structural, elastic, optical and thermodynamic properties. Perovskites have been explored for their thermodynamic properties, such as superconductivity, piezoelec-

tricity, ferroelectricity, magneto-resistivity, and other unusual thermodynamic characteristics. [1],[8].

These fluoro-perovskite $CsSrF_3$-like structures with band gaps exhibit insulating behaviour of about 5 eV at room temperature. The reduction of anion (halide) or dopant materials, both Cs, Sr, enhances the capability of conductivity and photocatalytic activity in CsSrF3 may be improved. Fluoride-type perovskites are suitable for different electronic and optoelectronic applications, like solid-state lithium-ion batteries. The chemistry, presentation, pricing, and protection aspects of each lithium-ion battery type are unique to that type. Lithium-ion batteries, in contrast to lithium primary batteries, utilise an intercalated lithium compound as their electrode material (which is disposed of after usage) [9]. M. S. Whittingham from Binghamton University originally proposed lithium-ion batteries in the 1970s. Whittingham's cathode and anode were both made of titanium(II) sulphide [10]. They are a wide range of applications, such as electric vehicles [11], high conductivity of electric current [12], Uninterruptible power supply (UPS) for mobile gadgets, cars, and stationary equipment [13].

These fluoro-perovskite compounds, such as $KCaF_3$, $RbCaF_3$ [14], $BaLiF_3$ [15], $SrLiF_3$ [16], have recently attracted a lot of attention from researchers for their various applications. But none of the commercially available crystals meet any of these characteristics. For practical uses in solar cells (solar panels), batteries (Lithium-ion batteries), and UV-Deep UV wave bands, more study is needed at all levels.

To a potentially large band gap of 6.34 eV, it has been recorded, as well as 4.833A^o eV for $CsSrF_3$. This substance has a high degree of iconicity. Para-electrically more conductive is the Centro systemic perovskite structure when it's at room temperature. Optically active $CsSrF_3$ perovskite material can be found in nature. Optical-electronic and photonic equipment can be used advantageously in this vessel. A solar device's anti-reflection coating is a fluoride-type material with a broad bandgap and short refractive index [17].

Because of its distinct physicochemical characteristics that set it apart from other alkali metals (such as Na, K, and Rb), lithium (Li) was selected as a dopant in $CsSrF_3$ fluoro-perovskite. While other alkali metals (Na^+: 1.02 Å, K^+: 1.38 Å, and Rb^+: 1.52 Å) are closer to Cs^+ in size, Li^+ (0.76 Å) has a far smaller ionic radius than Cs^+ (1.67 Å). While bigger dopants (like K^+) would result in excessive steric stress and unstable the cubic phase, Li substitution at the Cs site produces predictable strain. Unlike bulkier Na^+/K^+, which may cause phase segregation, smaller Li^+ preferentially occupies interstitial sites or replaces Cs^+ without collapsing the perovskite structure.

Lithium (Li) is used as a dopant because of its high mobility and small ionic radius, which allows it to efficiently replace Cs^+ or Sr^{2+} sites in the $CsSrF_3$ lattice without substantially altering the crystal symmetry. Li doping improves electrical conductivity and lowers the bandgap by modifying the electronic structure. Furthermore, Li improves the material's optical and elastic qualities by introducing localised states close to the Fermi level. Li-doped $CsSrF_3$ is a viable option for optoelectronic and photovoltaic applications because of these alterations.

In this work, to investigate Li doping with $CsSrF_3$ using first-principles calculations using DFT. According to our research and knowledge of the literature, Li materials have not been used as a dopant element with the $CsSrF_3$ compound. Li is substituted for Cs in the investigation of the fluoride perovskite crystal $CsSrF_3$ with different concentrations (x = 0, 0.11, 0.33, 0.55, 1) with a supercell of 2 x 2 1, which contributes new information on their structural, electronic, optical and elastic properties. Fluoroperovskites $CsSrF_3$ have a wide range of bandgap 5.543 eV, which recommends it for use in optical applications. The application of these qualities reveals information about a material's behaviour. Changing these factors can reveal variations during the elastic constant, shear (shear) strength, and bulk modulus, as well as further properties including conductivity, magnetic behaviour, and electronic band gap. Density functional theory can be applied to the study of elastic, optical, and electrical properties of the material $CsSrF_3$.These $CsSrF_3$ materials vary in the ultraviolet region used in optoelectronic devices and Solar cell applications.

2. Computational Details

Here, the USP plane-wave technique is used to determine the material's structural, optical, elastic, and electrical properties. Evaluations can be performed efficiently and precisely using Ultra-Soft Pseudopotential (USP) plane waves without being significantly impacted by orbital approximation errors. We used GGA-PBE techniques in conjunction with first-principles calculations in DFT-based CASTEP software (Clark et al., 2005) to calculate the results [17]. This strategy enables faster and more effective approximations for computational techniques. The cubic structure of CsSrF3, which has three fluorine atoms in the face centre locations, one caesium atom at the intersections, and one strontium atom in the body centre, represents the space group of Pm3m (#221) at normal temperature. In order to prevent boundary effects, a supercell approach is needed to study Li doping. To take into account the

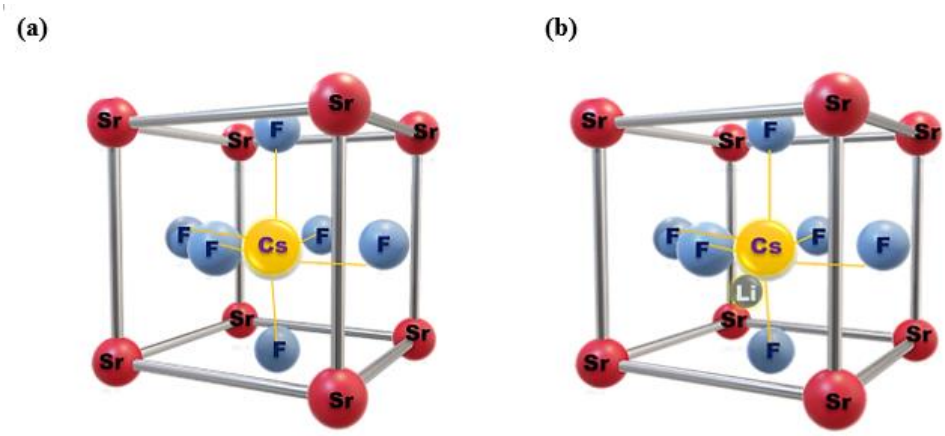

Figure 1: *Representing **(a).** Pure CsSrF3 Structure and **(b)**. Doped with lithium Structure*.

structural, electrical, optical, and elastic aspects in this study, a 2 × 2 × 1 supercell was constructed using these techniques [18].

After that, we improved the geometry of the super cells to study their characteristics. The atomic total energy in these calculations is 5 x10-5 eV. The entire Brillouin zone was subjected to the energy cutoff once k-integration was completed in the instance of geometry optimisation at 2x2x1 k-points. Determine the electrical, optical, and elastic characteristics following the geometry optimisations.

3. Results and Discussion

3.1. Structural Property

When atomic-level analysis lacks experimental observations, first-principle analysis has been utilised to predict more accurate and quicker calculation techniques. This technology can be used to create new materials. The total ground state energy is calculated at different unit cell volumes in order to calculate the structural characteristics of CsSrF3. Although it is a minimisation process, we must first construct a supercell of that fluoroperovskite crystal with space group Pm3m (no 221) to perform computations. The Cs, Sr, and F ions' respective atomic positions in the elementary cell are (0, 0, 0), (0.5, 0.5, 0.5), and (0, 0.5, 0.5), respectively. The crystallographic positioning of CsSrF3 indicates that the fluorine ions maintain their face-centred position of the cubic supercell, while Cs lies at the corner and Sr at the body-centred position, as depicted in the figure. As shown in Figure 1, the lithium material serves as a dopant element, similar to Cs. The CASTEP software was used for all computations in this paper, which are based on density functional theory (DFT). In this instance, the exchange-correlation function was defined using GGA-PBE methods [19].

3.2. Geometry Optimisation

The first step is geometrical optimisation for both pristine and doped supercells. Calculate the equilibrium lattice constant employing the Murnaghan equation of state by adding up all of the crystal's energy and determining how the large range of lattice constant values affects it. The volume (V0) of an equilibrium cell indicates the total amount of energy stored there [20]. Once the geometry has been optimised, the lattice constant parameters and volumes for both pristine and doped materials have been determined. Our calculations (a = b = c) for the lattice parameters of the Li-doped CsSrF3 structure differ considerably from those we found, as Table 1 illustrates. By increasing the number of doping atoms, the lattice parameter values increase, resulting in a decrease in the bandgap and an expansion of the volume. An optimised pristine and doped supercell (2x2x1) structure is depicted in Figure

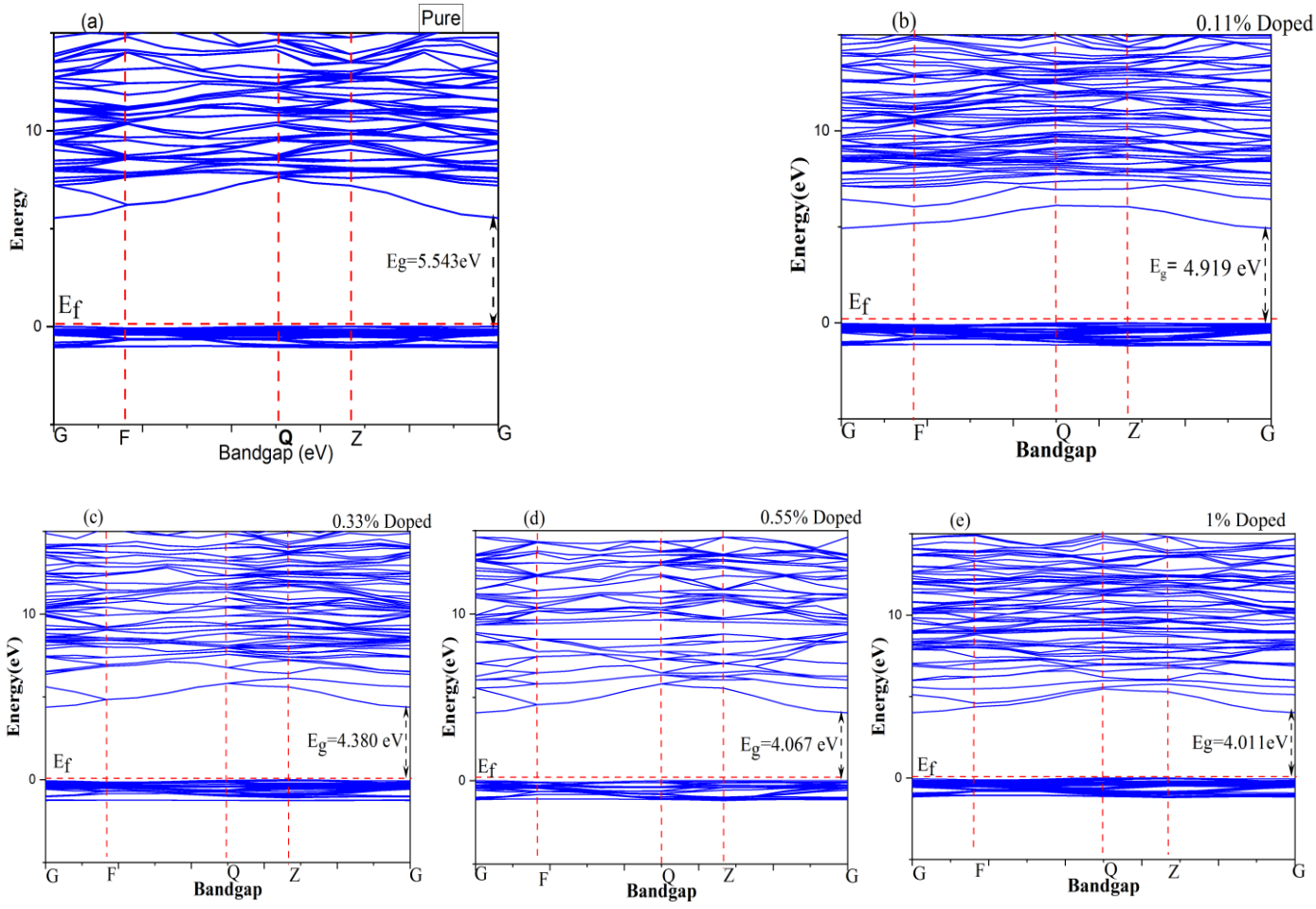

Figure 2: ***(a).*** *The band Gap for pure* $CsSrF_3$, ***(b).*** *Band gap CsSrF3 doped Li with 0.11%,* ***(c)****. Band gap CsSrF3 doped Li with 0.33%,* ***(d).*** *Band gap CsSrF3 doped Li with 0.55% and* ***(e).*** *Band gap CsSrF3 doped Li with 1%.*

1(a-b).

Table 1:
Calculated Lattice parameter and Volume for $CsSrF_3$ with Li doping

$Cs_{1-x}Li_xSrF_3$ Previous work	Lattice Parameter (Å) a = b = c 4.83	Volume (Å^3) 124.251
$Cs_{1-x}Li_xSrF_3$ X=0	5.000	125.000
$Cs_{1-x}Li_xSrF_3$ X=0.11	5.014	126.052
$Cs_{1-x}Li_xSrF_3$ X=0.33	5.064	129.861
$Cs_{1-x}Li_xSrF_3$ X=0.55	5.075	130.709
$Cs_{1-x}Li_xSrF_3$ X=1	5.076	130.787

3.2. Electronic properties

***Electronic Band Structure*:** The electronic characteristics of the compounds' energy band structure and density of states (TDOS & PDOS) are examined. Figure 2 shows that the evaluated band structure for pristine and doped compounds at the directions of symmetry for the equilibrium geometry is located in the first Brillouin Zone. The band gaps for the compounds of pristine CsSrF3 are 5.543 eV and Li doped with different concentrations (0%-1 %), the band gaps are 4.919 eV to 4.011 eV, respectively. We have analysed that after increasing the concentrations of dopant material, the band gap is towards decreasing. Figure 2(a) illustrates the indirect band nature of the CsSrF3 compound, which shows that the valence band maxima and the conduction band minima occur at the G and F symmetry points. Most people are familiar with the idea that phonons dissipate a considerable amount of energy when an electron transitions through the valence band to the conduction band in an indirect manner. For Li-doped $CsSrF_3$, in cooperation of the valence and conduction bands are located at point G in Figure 2(b-e). This demonstrates that the doping material has undergone a direct band gap transition. Based on this analysis, it can be shown that the valence band of $CsSrF_3$ doped with Li exhibits a higher G point shift than the pristine $CsSrF_3$ valence band. Electrons are moved from the valence band to the conduction band by the phonons, which causes an energy loss. Both the Conduction Band (CB) and the Valence Band (VB) can be found above and below the Fermi level (E_F), respectively. In this illustration, the dotted line denotes the Fermi energy E_F. Using DFT, the calculated values of pristine and dopant $CsSrF_3$ are given in Table 2. In semiconductors and insulators, the electronic band gap is calculated by subtracting the lowest Conduction Band (CBM) from the highest Valence Band (VBM). Since their bandgaps are in the UV spectrum, they may be used in optoelectronic devices.

$CsSrF_3$ fluoro perovskite has a bandgap of 5.543 eV. The bandgap reduces as the dopant material concentration rises. This bandgap varies in the ultraviolet region. With Li doping, the shear modulus drops from 15.663 GPa (Pristine) to 3.362 GPa (x* = 0.55), suggesting increased ductility.

***Total Density of States (TDOS) and Partial Density of States (PDOS)*:** Nonetheless, more details regarding the band structure may be revealed by the density of states. Both the total and partial density of states can be used to characterise the band structure's rising turn. The electron contribution to the valence and conduction bands is depicted by the Total and Partial Density of States (TDOS and PDOS) for the pristine and doped materials, respectively, in Figures S3 indicating the energy loss experienced by electrons and S4. Using a computational approach, Fermi's Golden Rule can be determined based on the number of final states and excited electrons. By splitting the band structure into three primary components, the valence band, the conduction band, and the Fermi energy level (EF), high peaks of density of state can be examined. The Fermi level EF is shown by the vertical, labelled dotted line. The left side of the Fermi level represents the valence band, whereas the right side represents the conduction band. Figure S1. Total Density of States (TDOS) illustrates the primary distinctions between the valence and conduction bands before and during doping.

Table 2:
Calculated Lattice parameter and bandgap for $CsSrF_3$ with Li doping

$Cs_{1-x}Li_xSrF_3$ Previous work	Lattice Parameter (Å) a = b = c 4.83	Bandgap (eV) 5.663
$Cs_{1-x}Li_xSrF_3$ X=0	5.000	5.543
$Cs_{1-x}Li_xSrF_3$ X=0.11	5.014	4.919
$Cs_{1-x}Li_xSrF_3$ X=0.33	5.064	4.380
$Cs_{1-x}Li_xSrF_3$ X=0.55	5.075	4.067
$Cs_{1-x}Li_xSrF_3$ X=1	5.076	4.011

The partial density of states for pristine and "Li" doped with $CsSrF_3$ are shown in Figure S2. Li doping considerably changes the structure of CsSrF3, principally due to the formation of 5-states in pristine $CsSrF_3$. The p and s-DOS have the greatest influence on the upper valence band after doping, as can be shown from the results. For comparison, the sharp peak shows either side of the Fermi level before and after doping. The PDOS has been plotted, which indicates the electronic contribution difference in the valence band and conduction band between pristine and impure (doped) systems. The density of states indicates that the valence band is composed of F-p states with a minor contribution from Sr-s states. In the conduction band, Sr-s play a vital role.

3.4. Thermodynamic Property

To verify the structural stability of $CsSrF_3$ and its Li-doped counterparts ($Cs_{1-x}Li_xSrF_3$), we calculate the binding energies and formation enthalpy (ΔH_f). A better approach for achieving these conditions is given below;

***Calculation of Formation Enthalpy (ΔH_f)*:** The formation enthalpy measures the energy of a compound compared to that of its component elements in their standard states, allowing for the determination of its thermodynamic stability. ΔH_f for $CsSrF_3$ and $Cs_{1-x}Li_xSrF_3$ can be calculated as follows:

$$\Delta H_F = E_{Cs1-xLixSrF3} - [(1-x)E_{Cs} + xE_{Li} + E_{Sr} + 3E_F] \quad \textbf{(1)}$$

Where, $E_{Cs1-xLixSrF3}$ is the doped system's total energy and E_{Cs} , E_{Li}, E_{Sr} ,E_F are the energies of bulk phases or isolated atoms (such as the F_2 molecule, fcc-Sr, bcc-Cs, and bcc-Li).

To evaluate thermodynamic stability, the formation enthalpy (ΔH_f) of $Cs_{1-x}Li_xSrF_3$ was measured. The exothermic formation of pure $CsSrF_3$ is confirmed by $\Delta H_f = -4.2$ eV/atom. Despite lattice expansion, stability is maintained with Li doping (x = 0.11–1), as

seen by ΔH_f, which varies between -3.9 and -4.0 eV/atom. Cubic phase stability is further confirmed by negative ΔH_f values, which are consistent with the Birch-Murnaghan equation of state and tolerance factor (0.92–0.95).

Doping (x)	ΔH_f (eV/atom)	Remarks
0 (Pure)	−4.20	Most stable configuration
0.11	−3.95	Slight destabilization
1.00	−4.00	Stable Li-substituted phase

Stability Validation: The spontaneous formation is confirmed by a negative ΔH_f. Comparative analysis with Elastic Constants: All doped systems should meet the mechanical stability requirements (C 11 − C 12 > 0, C 44 >0) for mechanical stability.

3.5. Optical properties

Optical parameters are very useful to explore the electronic band structure analytically. The metrics that show the interaction between light and matter include reflectivity, refractive index, absorption, conductivity, extinction coefficient, dielectric function, and loss function. Firstly, we compute these optical properties for pristine material and compare these properties after doping Li, as shown in Figure S5. The intra- and interband transitions are used to calculate the optical spectra. When it comes to metals, the interband contributions are substantial and can be broken down into two categories: direct and indirect transitions. As shown in Eq. (2), given their negligible effect on ε(ω) and their phonon-scattering nature, indirect interband transitions are disregarded. For optical response, the phonon energy range is 0-30 eV. All these properties are interconnecting frequency-dependent; therefore, the complex dielectric functions (the real part denotes $\varepsilon_1(\omega)$and the imaginary part denotes $\varepsilon_2(\omega)$).

$$\varepsilon(\omega)= \varepsilon_1(\omega) + \varepsilon_2(\omega) \quad \textbf{(2)}$$

The dielectric function's imaginary and real components displayed energy dissipation and polarisation, respectively. The dissipation of energy was shown by the smaller peak of the imaginary portion for both pristine CsSrF3 and "Li" doped. To put it another way, 0eV indicates there is no dissipation of energy in this portion. The dielectric function (real) values for pristine $CsSrF_3$ are 3.1 eV and the values are 2.6, 2.3, 2.1 and 2.0 eV after doping with “Li” at different concentrations and the dielectric function for imaginary parts, whose values for pristine.

$CsSrF_3$ of 3.0 eV and dopant are 2.6, 2.0, 1.5 and 0.8 eV, respectively. As demonstrated in Eqs (3)-(7), the formula can also be used as a basis for further calculations of optical properties, such as the refractive index n (ω), reflectivity R (ω), energy loss L (ω), and absorption coefficient I (ω), [21].

$$n(\omega) = \frac{1}{\sqrt{2}}\left\{[\varepsilon_1^2(\omega) + \varepsilon_2^2(\omega)]^{\frac{1}{2}} + \varepsilon_1(\omega)\right\}^{\frac{1}{2}} \quad \textbf{(3)}$$

$$L(\omega) = \mathrm{Img}\left(\frac{-1}{\varepsilon(\omega)}\right) \quad \textbf{(4)}$$

$$A(\omega) = \frac{2\omega}{c}k(\omega) \quad \textbf{(5)}$$

$$R(\omega) = \left|\frac{\sqrt{\varepsilon_1(\omega)+i\varepsilon_2(\omega)}-1}{\sqrt{\varepsilon_1(\omega)+i\varepsilon_2(\omega)}+1}\right|^2 \quad \textbf{(6)}$$

$$k(\omega) = \frac{1}{\sqrt{2}}\left\{[\varepsilon_1^2(\omega) + \varepsilon_2^2(\omega)]^{\frac{1}{2}} - \varepsilon_1(\omega)\right\}^{\frac{1}{2}} \quad \textbf{(7)}$$

Any compound's reflectivity reveals the behaviour of its surface. How much of the energy from the light reaches the surfaces of the compounds? A certain threshold will cause the values to return to their starting values. When electrons from the valence band contribute to conduction, the reflectivity peaks move to higher frequencies. The value of the reflectivity peak for pristine $CsSrF_3$ is 0.27 eV and after doping, the values of reflectivity with different concentrations of lithium doping are 0.21, 0.20, 0.18, and 0.10 eV, respectively. The optical reflectivity analysis measures the amount of light that would fall as an incident ray on the surface of the material. Lower reflectivity means increased UV or visible light absorption, according to recent research of examination. Increased total energy contribution from valence bands to conduction bands; these measurements demonstrate a modest shift in the reflectivity peak towards a higher frequency value, as shown in Figure S3. In the case of the energy loss function L(ω), as illustrated in Figure S5, the amount of energy lost is indicated by the movement of electrons through the materials. To accurately characterise the properties of plasma resonance, the plasma frequency is well captured by the energy loss function L(ω). The pristine materials whose higher peak values are 3.3 eV, and the dopant materials have values ranging from 2.8 to 1.9 eV. In areas with little absorption, we found that reflection was highest, as shown in Figure S5. Each material's response to radiation is indicated by its absorption coefficient. The photons interact with the electrons to shift them from the valence band to the conduction band, and this interaction is very frequency dependent, as measured by the absorption coefficient. A material's ability to absorb photons of a given energy is represented by its absorption coefficient. The absorption spectra are influenced by doping. Figure S5 shows the refractive index (n) for Pristine $CsSrF_3$; the value of n is 1.78eV eV. Also, for Li-doped values are 1.6- 1.4 eV. Materials with strong conductivity, absorption, and refractive index can improve photovoltaic systems. The high-energy area shows that these materials can be used for UV optoelectronics [22].

3.6. Elastic properties

The mechanical behaviour of crystalline solids can be accurately inferred from elastic characteristics. The following relation (Grimvall, 1999) can be used to define various fundamental solid-state phenomena, including the equation of state, intrinsically mechanical, and cubic stability conditions explained below in Eqs (8)-(12):

$$C_{11}\text{-}C_{12}>0 \quad \textbf{(8)}$$

$$C_{11}>0 \quad \textbf{(9)}$$

$$C_{44}>0 \quad \textbf{(10)}$$

$$C_{11}+C_{12}>0 \text{ (mechanical stability condition)} \quad \textbf{(11)}$$

$$C_{12}<B<C_{11} \text{(cubic stability condition)} \quad \textbf{(12)}$$

***Elastic Constant Calculations*:** It is possible to describe the elastic properties using the constants of elasticity. The elastic constant provides the standard description of the bulk and shear modulus can be best described by the Voigt-Reuss-Hill (VRH) method, discovered by Reuss and Angew in 1929 (Sakaguchi, Wiltbank, & Murchison, 2004) The measure of the resistance to reversible deformation can be best explained by the shear modulus G from the following relation, as described from Eqs (13)- (16):

$$G_V = (C_{11}-C_{12}+3C_{44})/5 \quad \textbf{(13)}$$

$$G_R = 5*C_{44}\,(C_{11}-C_{12})/[(4*C_{44}+3(C_{11}-C_{12})] \quad \textbf{(14)}$$

$$G=G_V+G_R/2 \quad \textbf{(15)}$$

However, the expression of the bulk modulus B is mentioned in the equation:

$$B = (C_{11}+2*C_{12})/3 \quad \textbf{(16)}$$

The value of bulk and shear modulus for pristine and doped can be calculated in Table 3, respectively.

Table 3:
Calculated parameters Bulk modulus "B" (GPa), Shear modulus "G" (GPa), Young's modulus "E" (GPa), Poisson's ratio "V", Anisotropy "A", and Pugh's ratio "B/G" respectively.

Material/doping concentration	B	G	E	V	A	B/G
$Li_xCs_{1-x}SrF_3$ X=0	-9.890	15.66	99.53	2.177	1.591	0.631
$Li_xCs_{1-x}SrF_3$ X=0.11	20.09	11.03	27.983	0.267	1.122	1.821
$Li_xCs_{1-x}SrF_3$ X=0.33	-0.350	8.834	-3.574	-1.202	0.370	-0.039
$Li_xCs_{1-x}SrF_3$ X=0.55	83.13	3.362	9.951	0.480	0.410	24.72
$Li_xCs_{1-x}SrF_3$ X=1	-17.31	-47.34	-74.30	-0.215	-0.750	0.365

Table 3 shows the Young modulus E, the anisotropic factor A, the Poisson's ratio V, and the Pugh's index of pristine and doped $CsSrF_3$, which can be figured out using the equations listed below [23].

$$A = 2*C_{44}/ (C_{11}-C_{12}) \quad \textbf{(17)}$$

$$E = 9*GB/3*B+G \quad \textbf{(18)}$$

$$V = 3*B-2*G/2(2*B+G) \quad \textbf{(19)}$$

$$B/G = \text{Pugh's ratios} \quad \textbf{(20)}$$

As depicted from Eqs (17)-(20), the value of elastic anisotropy denoted by A, if A= 1 (Isotropic) and A is not equal to 1 (Anisotropic), is obtained through DFT using the exchange correlation functional of GGA-PBE methods. In the present study, we analyse the results of the compound as shown in Table 3, that $CsSrF_3$ is anisotropic because its "A" value is not equal to 1. Using the bulk modulus B, scientists can estimate the material's strength or hardness and determine whether the material is ductile or brittle. If the value of the bulk modulus is higher than the material is stronger, and if the value is lower, the material is softer. To determine CsSrF3's bulk modulus, this indicates that it is a soft material. The hardness of $CsSrF_3$ is further supported by the greater values of both shear and Young modulus, utilising Poisson's ratio V if which suggests that crystals are ductile or brittle. The $CsSrF_3$ material shows a brittle nature according to the calculated results in Poisson's ratio. The Young's modulus is another key metric that may be used to elevate crystals' stiffness, and indicates that the materials belong to the stiff group. The compound is brittle; it may be used on autos and curved glass surfaces. It has fractures with small elastic deformation and without significant plastic deformation, which absorb little energy during deformation.

8. Conclusion

Using first-principles calculations in DFT with GGA-PBE methods, are to investigate Li doping with $CsSrF_3$. Before and after Li doping, the electronic band structure has been calculated. In addition, the TDOS and PDOS concepts are used to discuss the intricacies of band structure in both circumstances. As a result of Li doping, the electronic band structure of CsSrF3 has been reduced and transformed from an indirect bandgap to a direct bandgap. Reducing the DOS down to the lower energy increases the interaction between the Li atom and its immediate neighbour. Particularly affected by Li doping is the PDOS of the 0-2p state closest to the bottom of the conduction band, while the PDOS of the 0-1s state towards the top of the valence band also undergoes significant modification. Li doping reduces the bandgap of $CsSrF_3$ by 27.6% (5.543 eV → 4.011 eV), making it suitable for UV optoelectronic applications. The adjustable refractive index (1.78–1.40) and anisotropic elastic response (A1) indicate potential applications in anti-reflective coatings for solar cells. The optical properties provide high reflectivity, refractive index and absorption coefficient. The Young's modulus, bulk modulus, and shear modulus were also calculated. The bulk modulus value is another indicator of a material's hardness. The Poisson's ratio makes a covalent nature of the molecule appear more likely. This demonstrates that $CsSrF_3$ can be a possible material for optical and optoelectronic devices.

Declaration

Competing Interests: The authors declare that they have no known competing financial interests or personal relationships that could have appeared to influence the work reported in this paper.

Ethical Issues: There are no ethical issues. All data in this paper is publicly available.

Author Contribution Statement: F.H. and A.F. conceived the idea and designed the research; analysed and interpreted the data and wrote the paper.

Funding Statement: This research did not receive any specific grant from funding agencies in the public, commercial, or not-for-profit sectors.

Consent to Publish: All authors have agreed to publish the version of the manuscript in this journal.

References

1. Reshak, A., M. Abu-Jafar, and Y. Al-Douri, *Two symmetric n-type interfaces $SrTiO_3/LaAlO_3$ in perovskite: electronic properties from density functional theory.* Journal of Applied Physics, 2016. **119**(24): p. 245303.
2. Rizwan, M., A. Ali, Z. Usman, N. Khalid, H. Jin, and C. Cao, *Structural, electronic and optical properties of copper-doped $SrTiO_3$ perovskite: A DFT study.* Physica B: Condensed Matter, 2019. **552**: p. 52-57.
3. Stamatelatos, A., M. Tsarmpopoulou, A. Chronis, N. Kanistras, D. Anyfantis, E. Violatzi, D. Geralis, M. Sigalas, P. Poulopoulos, and S. Grammatikopoulos, *Optical interpretation for plasmonic adjustment of nanostructured Ag-NiO thin films.* International Journal of Modern Physics B, 2021. **35**(06): p. 2150093.
4. Li, J., X. Zhang, Z. Fang, X. Cao, Y. Li, C. Sun, Z. Chen, and F. Yin, *First-principles calculations to investigate electronic, elastic, and optical properties of one dimensional electride Y5Si3.* Results in Physics, 2021. **28**: p. 104615.
5. Al-Douri, Y., N. Amrane, and M.R. Johan, *Annealing temperature effect on structural and optical investigations of Fe_2O_3*

nanostructure. Journal of Materials Research and Technology, 2019. **8**(2): p. 2164-2169.
6. Souadia, Z., A. Bouhemadou, S. Bin-Omran, R. Khenata, Y. Al-Douri, and S. Al Essa, *Electronic structure and optical properties of the dialkali metal monotelluride compounds: Ab initio study.* Journal of Molecular Graphics and Modelling, 2019. **90**: p. 77-86.
7. Gherriche, A., A. Bouhemadou, Y. Al-Douri, S. Bin-Omran, R. Khenata, and M. Hadi, *Ab initio exploration of the structural, elastic, electronic and optical properties of a new layered perovskite-type oxyfluoride: $CsSrNb2O_6F$.* Materials Science in Semiconductor Processing, 2021. **131**: p. 105890.
8. Qiao, H. and Q. Wei, *Functional nanofibers in lithium-ion batteries*, in *Functional Nanofibers and their Applications*. 2012, Elsevier. p. 197-208.
9. Whittingham, M.S., *Electrical energy storage and intercalation chemistry*. Science, 1976. **192**(4244): p. 1126-1127.
10. Zaghib, K., J. Dubé, A. Dallaire, K. Galoustov, A. Guerfi, M. Ramanathan, A. Benmayza, J. Prakash, A. Mauger, and C.M. Julien, *Lithium-ion cell components and their effect on high-power battery safety*, in *Lithium-Ion Batteries*. 2014, Elsevier. p. 437-460.
11. Ramesh, M., N. Kuppuswamy, and S. Praveen, *Metal-organic framework for batteries and supercapacitors*, in *Metal-Organic Frameworks for Chemical Reactions*. 2021, Elsevier. p. 19-35.
12. Sukanya, G., R. Suresh, and R. Rengaswamy, *Data-driven prognostics for Lithium-ion battery health monitoring*, in *Computer Aided Chemical Engineering*. 2021, Elsevier. p. 487-492.
13. Koussinsa, F., B. Bonnetot, and M. Diot, *Propriétés thermodynamiques des fluoropérovskites de potassium ($KCaF_3$) et de rubidium ($RbCaF_3$)(10–300 K): transition de phase.* Thermochimica acta, 1992. **206**: p. 1-11.
14. Korba, S.A., H. Meradji, S. Ghemid, and B. Bouhafs, *First principles calculations of structural, electronic and optical properties of $BaLiF_3$.* Computational materials science, 2009. **44**(4): p. 1265-1271.
15. Mahmoud, N.T., J.M. Khalifeh, and A.A. Mousa, *Effects of rare earth element Eu on structural, electronic, magnetic, and optical properties of fluoroperovskite compounds $SrLiF_3$: First principles calculations.* Physica B: Condensed Matter, 2019. **564**: p. 37-44.
16. Murtaza, G., I. Ahmad, M. Maqbool, H.R. Aliabad, and A. Afaq, *Structural and optoelectronic properties of cubic $CsPbF_3$ for novel applications.* Chinese Physics Letters, 2011. **28**(11): p. 117803.
17. Kohn, W., *Density functional theory.* Introductory Quantum Mechanics with MATLAB: For Atoms, Molecules, Clusters, and Nanocrystals, 2019.
18. Rizwan, M., W. Azam, S. Gillani, I. Zeba, M. Shakil, S. Ali, and R. Ahmad, *A computational study to explore the effects of copper doping concentration on phase stability, electronic band structure and optical properties of $CsSrF_3$ fluro-perovskite.* Molecular Physics, 2021. **119**(9): p. e1892226.
19. Yang, J.-S., L. Zhao, L. Shi-Qi, H. Liu, L. Wang, M. Chen, J. Gao, and J. Zhao, *Accurate electronic properties and non-linear optical response of two-dimensional MA2Z4.* Nanoscale, 2021. **13**(10): p. 5479-5488.
20. Zeba, I., R. Kiran, M. Shakil, M. Rafique, R. Ahmad, and S. Gillani, *Study the effect of magnesium doping concentration on structural and optoelectronic response of $NaCa1\text{-}xMgxF_3$ fluoro-perovskite: First-principles computation.* Optik, 2020. **218**: p. 164990.
21. Hoat, D., J.R. Silva, and A.M. Blas, *First principles study of structural, electronic and optical properties of perovskites $CaZrO_3$ and $CaHfO_3$ in cubic phase.* Solid State Communications, 2018. **275**: p. 29-34.
22. Yang, J., L. Yang, and J. Long, *Theoretical investigation of the electronic structure, optical, elastic, hardness and thermodynamics properties of jadeite.* Materials Science in Semiconductor Processing, 2015. **31**: p. 509-516.
23. Pugh, S., *XCII. Relations between the elastic moduli and the plastic properties of polycrystalline pure metals.* The London, Edinburgh, and Dublin Philosophical Magazine and Journal of Science, 1954. **45**(367): p. 823-843.